University of South-Eastern Norway
Faculty of Technology, Natural Sciences and Maritime Studies

Doctoral dissertation no. 66
2020

Kenneth Kirkeng Andersen

Therapeutic dual-frequency ultrasound transducers

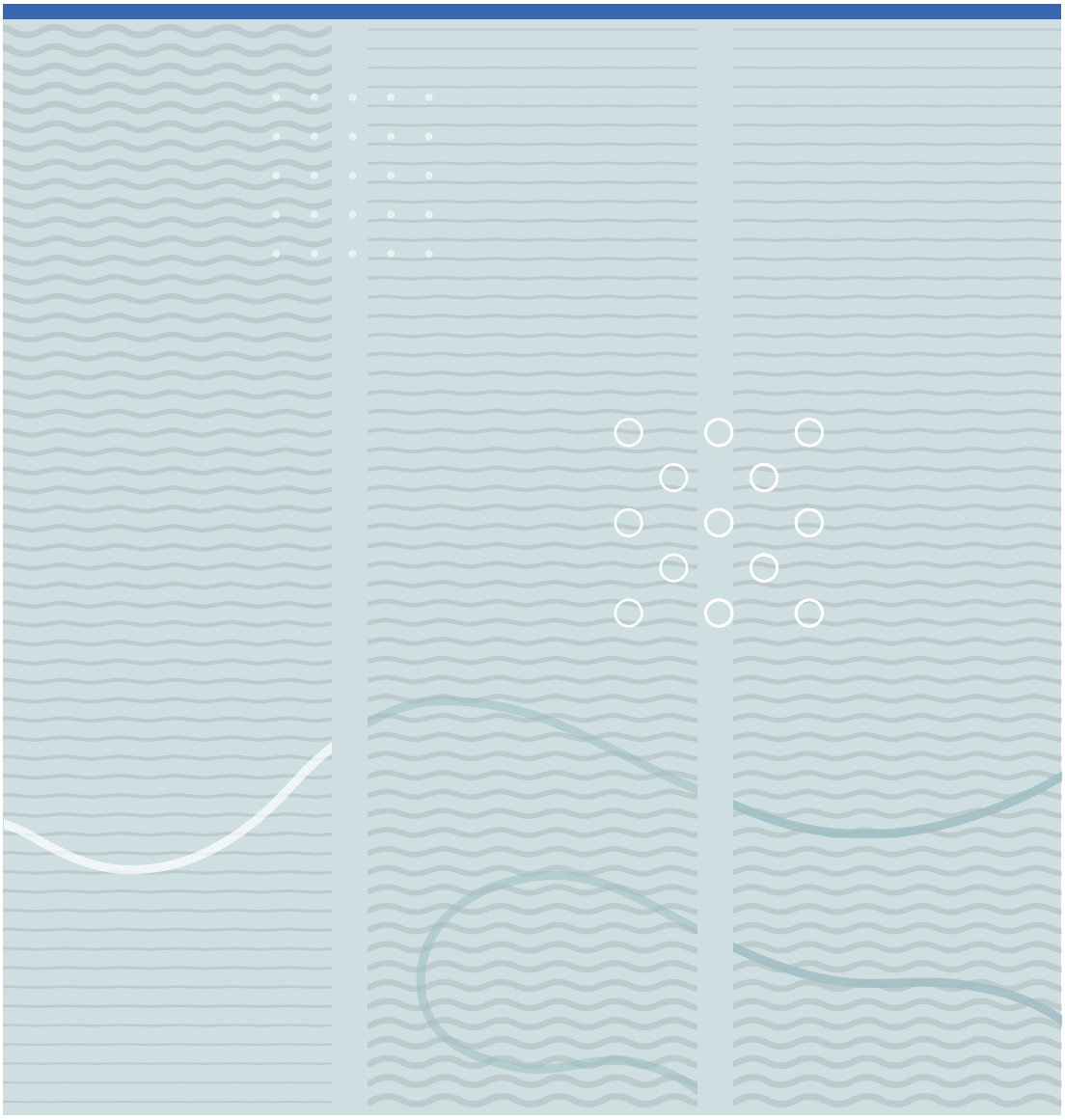

Kenneth Kirkeng Andersen

Therapeutic dual-frequency ultrasound transducers

A PhD dissertation in
Applied Micro- and Nanosystems

Faculty of Technology, Natural Sciences and Maritime Studies
University of South-Eastern Norway
Horten, 2020

Doctoral dissertations at the University of South-Eastern Norway no. 66

ISSN: 2535-5244(print)
ISSN: 2535-5252 (online)

ISBN: 978-82-7860-427-4 (print)
ISBN: 978-82-7860-428-1 (online)

Print: University of South-Eastern Norway

Dedication

First of all I would like to extend my gratitude to my supervisors Professor Lars Hoff, Associate Professor II Martijn E. Frijlink, and Dr Tonni F. Johansen — Their supervision has made this project possible to complete.

I thank Dr Andrew Healey at Phoenix Solutions AS for many discussions and cheerful hours spent in the laboratory — I sincerely hope that Acoustic Cluster Therapy will be successful. The prototype transducer and pre-clinical set-up for testing of Acoustic Cluster Therapy on tumours in mice would never have been realised without the help of Senior Engineer Svein Mindrebøe — Phoenix Solutions AS and I are indebted to you.

I extend my gratitude to Associate Professor Tung Manh for showing me the ropes on transducer manufacturing. I also thank the laboratory staff at the Department of Microsystems Anh Thai Nguyen, Birgitte Kasin Hønsvall, Thomas Martinsen, Zekija Ramic, and, last but not least, the Chief Engineer Ole Henrik Gusland for consistent assistance and guidance.

I am also grateful for the many colleagues I have had during my time as a PhD candidate at the University of South-Eastern Norway (USN). The colloquial chatter in the hallways has made the day-to-day existence a delight.

Lastly, I thank my family and friends for support and love throughout the years as a PhD candidate.

Preface

This doctoral thesis is submitted in partial fulfilment of the requirements for the degree of Philosophiae Doctor at the Faculty of Technology, Natural Sciences, and Maritime Sciences, University of South-Eastern Norway, Campus Vestfold, Norway.

The work was carried out at the Department of Microsystems, Faculty of Technology, Natural Sciences, and Maritime Sciences, University of South-Eastern Norway, Campus Vestfold, Norway, under the supervision of Professor Lars Hoff, associate Professor II Martijn E. Frijlink, and Dr Tonni F. Johansen.

Lars Hoff and Martijn E. Frijlink are with the Department of Microsystems, University of South-Eastern Norway, Campus Vestfold, Norway. Tonni F. Johansen is with the Department Circulation and Medical imaging, Norwegian university of science and technology, Trondheim, Norway and SINTEF Digital, Acoustics, Trondheim, Norway.

This work was supported by the Research Council of Norway (grant number 237887) through the Centre for Innovative Ultrasound Solutions (CIUS).

Abstract

The interaction of ultrasound with organic and non-organic matter has opened up for a vast industry. Arguably, in medicine, the most known application of ultrasound is diagnostic imaging of fetuses. However, ultrasound can be used as a therapeutic agent, too. Examples of treatments utilising ultrasound include treatment and surgically removal of solid malignant tumours; to disintegrate kidney stones; in combination with microbubbles, to increase the efficacy of a wide range of drugs and to help drugs pass the blood-brain barrier — to name but a few.

Typically, the tissue volume to be treated is hidden from the physicians' view and, because of this, both ultrasound or magnetic resonance imaging (MRI) are used to guide the therapeutic ultrasound. Although MRI exhibits excellent image quality, it is expensive and not portable. Ultrasound diagnostic imaging, on the other hand, is inexpensive, portable, and exhibits excellent image quality, which renders it a good imaging candidate for the ultrasound therapeutic applications. One challenge with designing a combined ultrasound imaging and therapeutic system is found in the respective centre frequencies. Due to tissue absorption and image resolution, the therapeutic centre frequencies are often much lower compared to the imaging centre frequencies, respectively. Because of this, a combined ultrasound imaging and therapeutic system may require transducers than can operate beyond the bandwidth limitation ($\sim$100%) of conventional piezoceramic transducers.

The current thesis aims at investigating transducer designs and optimisation methods for so-called *dual-frequency* transducers applicable for ultrasound therapeutic applications. A *dual-frequency* transducer is defined as a transducer that accommodates two usable frequency bands in the same transducer, where the two frequency bands could not have been realised using only the fundamental frequency band. A dual-frequency transducer is typically realised by use of two piezoceramics in different mechanical and electrical configurations. The piezoceramic can be placed next to each another or on top of each other, and the piezoceramics can be of comparable thicknesses or of very differ-

ent thicknesses; however, a dual-frequency transducer may also be realised by exploiting the inherent harmonics in a single piezoceramic.

A challenge when designing a dual-frequency transducer is how to transfer the mechanical energy to the radiation medium. For this purpose, conventional transducers utilise one, or several, quarter-wave impedance transformers of a specific acoustic impedance. For certain dual-frequency transducer designs, the two frequency bands radiate through different apertures; however, this is not always the case. If the two frequency bands radiate through the same aperture, conventional optimisation methods based on quarter-wave impedance transformers may not be used.

Because of this, in Paper A, we designed a new numerical optimisation method for conventional and dual-frequency transducers. The method is based on a mathematical theorem and linearises the phase spectrum of transducer transfer functions. The linearisation is performed in a relevant frequency band, and can be performed on multiple frequency bands simultaneously.

Paper B and C are concerned with the designing, optimisation, and testing of a dual-frequency transducer and accompanying laboratory set-up for pre-clinical testing of Acoustic Cluster Therapy on tumours in mice. A motivation for this project was to simplify the existing laboratory set-up and workflow procedures to help mitigate human errors. The dual-frequency transducer replaced the existing laboratory set-up comprised of two different transducers which had to be carefully aligned to sonicate the tumour adequately. In total, six dual-frequency transducers and laboratory set-ups were manufactured which are currently in use at different research institutions around the world.

Paper D analyses a dual-frequency coupled resonator transducer (CRT). The CRT is comprised of two piezoceramic layers with a polymeric coupling layer sandwiched in between the piezoceramics. Depending on the electrical configuration, the CRT exhibits two usable frequency bands: One for short imaging pulses and another for longer, therapeutic pulses. The dual-frequency CRT has not received much attention in the literature, which motivated an analytical approach. Distributed, lumped, and mass-spring models describ-

ing the low-frequency band were developed, resulting in closed-form expressions for the resonance frequency.

List of abbreviations

ACT	Acoustic Cluster Therapy
ADV	Acoustic droplet vaporisation
CMUT	Capacitive micromachined ultrasonic transducer
CRT	Coupled resonator transducer
FEA	Finite Element Analysis
HF	High-frequency
HF-to-LF ratio	High-frequency to low-frequency ratio
HIFU	High-intensity focused ultrasound
LF	Low-frequency
MI	Mechanical index
POM	Polyoxymethylene
PVDF	Polyvinylidene fluoride
PW	Pulsed-wave
SURF	Second-order ultrasound field Imaging
USN	University of South-Eastern Norway

List of symbols

Symbol	Unit	Explanation
A	m^2	Area
C	Pa	Stiffness constant
c	$\mathrm{m \cdot s}^{-1}$	Sound speed
D	$\mathrm{C \cdot m}^{-2}$	Electric displacement
E	$\mathrm{V \cdot m}^{-1}$	Electric field
e	$\mathrm{C \cdot m}^{-2}$	Piezoelectric constant
f	Hz	frequency
f_c	Hz	Centre frequency
F	N	Force
$H = U/V$	$\mathrm{m \cdot s}^{-1} \cdot \mathrm{V}^{-1}$	Electro-mechanical transfer function
$i = \sqrt{-1}$	1	Imaginary unit
I_{SPTA}	$\mathrm{W \cdot cm}^{-2}$	Intensity (spatial peak temporal average)
$k = \omega/c$	$\mathrm{rad \cdot m}^{-1}$	Wave number
l	m	Thickness
p_r	Pa	Pressure peak rarefaction
S	1	Strain
T	Pa	Stress
U	$\mathrm{m \cdot s}^{-1}$	Normal particle velocity
V	V	Voltage
α	$\mathrm{dB \cdot MHz}^{-1} \cdot \mathrm{cm}^{-1}$	Attenuation coefficient
ϵ	$\mathrm{F \cdot m}^{-1}$	Permittivity
λ	m	Wavelength
ρ	$\mathrm{kg \cdot m}^{-3}$	Density
ω	$\mathrm{rad \cdot s}^{-1}$	Angular frequency

Contents

1. Introduction

1.1 Background and motivation

1.1.1 Ultrasound applications

Arguably, the most commonly known application of ultrasound is diagnostic imaging of fetuses. However, the interaction of ultrasound with organic and non-organic matter has opened up for a vast industry, ranging from medical applications such as diagnostic imaging to high intensity focused ultrasound (HIFU) treatment of benign and malignant solid tumours; beyond medical applications, ultrasound is used in the oil and gas industry to measure the quantity of gas (fiscal metering) and to evaluate the condition of the vast oil and gas pipeline systems (non-destructive testing); in the oceans, ultrasound is used to create maps of the seafloor, detecting submarines, and estimating populations of fish and marine mammals — the list could continue. Throughout the remainder of the thesis, only medical ultrasound will be considered.

1.1.2 Ultrasound diagnostic imaging

The first diagnostic ultrasound image was published by Dr Karl Theodore Dussik in 1942; however, the origin of medical ultrasound imaging can be traced back to P. Langevin who, at the end of the first world war, took advantage of the development in piezoelectricity and vacuum tube amplifiers to be able to perform echo ranging in water [1]. Today, ultrasound diagnostic imaging is well established and several imaging modalities exists, e.g., B-mode [1], harmonic imaging [2], and Doppler [3, 4]. Ultrasound imaging is safe [5, 6] and is generally non-invasive; moreover, it is fast, relatively cheap and portable. Most ultrasound machines are comprised of a computer and a screen fitted on a cart trolley; however, lap-top and hand-held ultrasound machines exist, too, which are a great tool when the patients are restricted from coming to the hospitals.

Ultrasound images are formed by use of a transducer (cf. Sec. 1.1.5) to transmit temporal short mechanical waves to a small region of interest inside the body. Depending on the characteristics of the tissue, an echo is reflected off the tissue and propagates back to the transducer. This process is repeated until a larger area has been covered, and an

image can be formed. Generally, a higher frequency results in better image quality due to an increase in the spatial resolution [1, ch.5.5]. However, the ultrasound wave loses energy due to absorption and scattering as it propagates through the tissue, referred to as attenuation. For soft tissue and biological fluids, the attenuation coefficient α increases non-linearly with frequency [7, ch.4]. Because of this, the frequencies used for imaging are limited by the penetration depth and required signal-to-noise-ratio.

Ultrasound diagnostic imaging is safe [5,6] because the mechanical output power is regulated by the output display standard [8] and the IEC Standard 60601-2-37 [9]. The quantities that are regulated are the spatial-peak temporal-average intensity (I_{SPTA}) and the mechanical index (MI). The I_{SPTA} is related to heating of tissue and the MI is a threshold for the likelihood of cavitation activity. Generally, the maximum allowed I_{SPTA} and MI is $720\,\text{mW}/\text{cm}^2$ and 1.9, respectively; however, lower levels may be used [6, 10].

1.1.3 Ultrasound therapeutic applications

The interaction of ultrasound with tissue is termed ultrasound-induced bio-effects, and the two primary bio-effects are thermal and mechanical [1]. Thermal bio-effects refers to heating and non-thermal bio-effects refer to cavitation. Cavitation is classified as stable or inertial, where stable cavitation refers to sustainable, periodic nonlinear expansion and contraction of a gas body or bubble, and inertial cavitation refers to the rapid growth and violent collapse of a bubble [1, Ch.14,15].

Although severely detrimental to healthy tissue, if properly controlled, heating and cavitation may be used for ultrasound therapeutic applications. A therapeutic treatment with ultrasound consists of focusing the mechanical energy to a small volume to induce different biological effects in the tissue. For example, a small increase in the temperature of tissue, bone, or cartilage may be beneficial to physiotherapy patients [11]. Compared to the average temperature of the human body (36.5 °C to 37.5 °C), only a small increase in the tissue temperature to $\sim$41.8 °C is needed to arrest the growth of cancerous tissue, referred to as hyperthermia [12]; however, a significant increase in the tissue temperature may cause thermal ablation and permanent destruction of the tissue (HIFU [13]). By use of mechanical mechanisms, cavitation cloud histotripsy [14] or boiling histotripsy [15]

Table 1.1: Partial reproduction and expansion of Szabo's "Comparison of water values for medical ultrasound modalities" [1, Tab.15.1], where f_c is centre frequency, p_r is rarefactional pressure, and I_{SPTA} is spatial-peak temporal-average intensity.

Modality	f_c [MHz]	p_r [MPa]	I_{SPTA} [W/cm^2]
Diagnostic imaging	1-15	0.45-5.54	0.0003-0.991
PW Doppler	1-10	0.67-5.3	0.173-9.08
Physiotherapy	0.75-3.4	0.3	<3
Hyperthermia	0.5-5	0.6-6	1-10
HIFU	1-10		1000-10000
Lithotripsy	0.5-10	5-15	Very low
Histotripsy	0.75-3.0	10-25	

can be used to disintegrate tissue, and shock wave lithotripsy can be used to disintegrate kidney stones.

To better understand the differences between diagnostic imaging and ultrasound therapeutic applications, consider Table 1.1 where different medical ultrasound modalities are compared. From Table 1.1, we see that I_{SPTA} can be several orders of magnitude larger for the therapeutic modalities (physiotherapy, hyperthermia, HIFU) compared to diagnostic imaging. For the therapeutic applications, several pulse cycles are typically used which results in high duty-cycles. However, this is in strong contrast to diagnostic imaging where pulses comprised of a few cycles and low-duty cycles are used. The consequence of this is that the imaging pulses do not heat up the tissue, which is the objective of the therapeutic pulses. The second thing to notice in Table 1.1, is that the frequencies used for diagnostic imaging are generally higher than the frequencies used for the therapeutic modalities. Increasing the frequency improves the resolution of the ultrasound image; however, it also increases tissue absorption. For imaging, an increase in tissue absorption reduces the signal-to-noise-ratio. For the therapeutic applications, however, where I_{SPTA} can be many orders of magnitude larger than for the imaging applications, increased tissue absorption may lead to detrimental heating of healthy tissue outside of the focal point.

In general, ultrasound as a therapeutic agent is non-invasive, which is a major advantage compared to conventional surgery. However, the tissue volume to be treated is typically hidden from the physicians view and, because of this, ultrasound or magnetic resonance imaging (MRI) are used to guide the therapeutic ultrasound [13, 16]. Although MRI has high resolution and contrast, it is also expensive and not easily accessible. Ultrasound imaging, on the other hand, is relatively inexpensive and portable, which renders it a suitable imaging modality to accompany the therapeutic applications. However, the differences in the imaging and therapeutic frequencies pose a challenge when designing a combined imaging and therapy transducer. In Secs. 1.1.5 and 1.1.6 we will elaborate more on the implications of the differences in the imaging and therapeutic frequencies; for now, suffice it to say that due to the bandwidth limitation of conventional piezoceramic transducers ($\sim$100%), combined ultrasound imaging and therapeutic transducers can not be accommodated in the same transducer using conventional transducer designs.

1.1.4 Ultrasound mediated drug delivery

Another therapeutic application of ultrasound is mediated drug delivery. Ultrasound-mediated drug delivery refers to the use of ultrasound in combination with acoustically active particles to enhance the uptake of a particular drug to a target volume while simultaneously reducing the overall drug dose administered to the patient. In oncology, this may be a great benefit as many therapeutic regimes must be terminated due to unwanted side effects rather than successful treatment of the condition. In essence, a carrier is used to transport the drug to the target volume where ultrasound is used to both release the drug and activate certain physical mechanisms beneficial for the local drug administration [17]. Different carriers have been used, such as microbubble contrast agents [18], liposomes [17], micelles [17] and polymeric cups [19]. Moreover, acoustic droplet vaporisation (ADV) [20] and combinations of contrast agents and acoustically active droplets, such as Acoustic Cluster Therapy [21] are being pursued.

Acoustic Cluster Therapy (ACT) belongs to the ADV-class and is a new ultrasound mediated drug delivery system currently under development for cancer treatment [21]. The ACT product is comprised of a two-component formulation of commercially available microbubbles (Sonazoid; GE Healthcare, Oslo, Norway) and perfluorated oil microdroplets

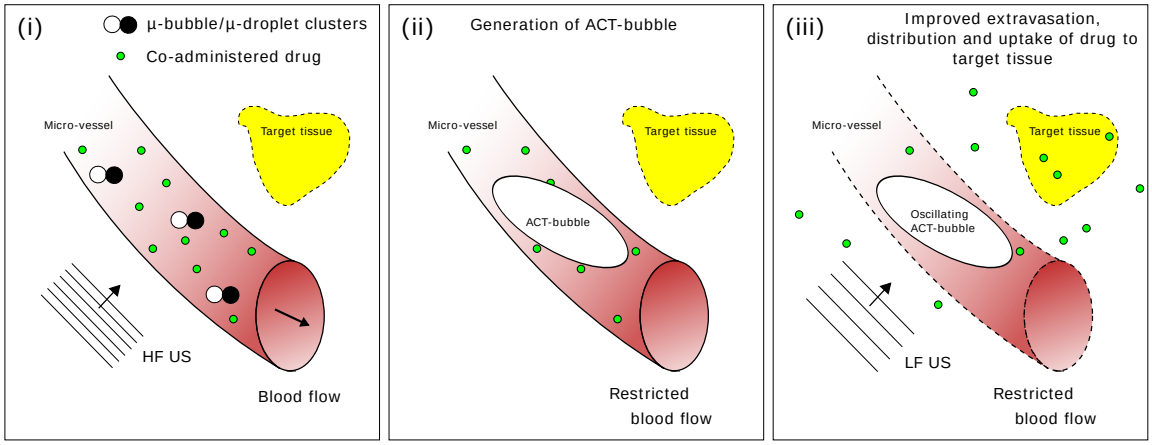

Figure 1.1: Working principle of ACT explained in the main text.

with a low boiling point ($\sim$50 °C). The microbubbles and microdroplets form clusters held together by electrostatic attraction [21].

In figure 1.1, a schematic of a therapeutic treatment with ACT is shown. First, the microbubble/microdroplet clusters are administered to a patient together with a drug. When the clusters reach the tumour, a high-frequency sonication regime is used to sonicate the tumour volume, Fig. 1.1 (i). The centre frequency is 2 MHz to 10 MHz and the MI is $\sim$0.35, significantly lower than the cavitation threshold. The microbubble components act as evaporation seeds and transfer energy to the oil droplets, resulting in vaporisation of the oil and the formation of the larger, gaseous ACT bubbles, Fig. 1.1 (ii). The gas-bubble population has a mean diameter in-vivo of 22 μm with no bubbles larger than 44 μm [22]. The gas-bubble size-range has been engineered so that the ACT bubbles lodge at the microvascular level and remain for 5-10 minutes.

A second low-frequency ultrasound exposure is used to enhance the uptake of the co-administered drug to the tumour [21], Fig. 1.1 (iii). The centre frequency is 0.5 MHz, closer to the resonance frequency of the gaseous bubbles, and the MI is $\sim$0.2. The mechanisms responsible for the enhanced uptake of the drugs include mechanical oscillations of the ACT bubbles which produce stable oscillation, localised microstreaming, radiation and shear forces that increase the local permeability of the vasculature, increasing transport of the co-administered drug across the capillary barrier and through the extracellular matrix [21].

For the high-frequency sonication, depending on the application, a range of centre frequencies can be used. For example, tumours hidden inside the body (e.g., liver metastasis) generally require lower centre frequencies compared to more superficial tumours (e.g., skin cancer). However, for all applications, the low-frequency centre frequency should be $\sim$0.5 MHz. The use of different centre frequencies for the high- and low-frequency sonication regimes require that the transducer's bandwidth exceed 120%. As was pointed out in Sec. 1.1.3, conventional ultrasound transducers have a bandwidth limitation of $\sim$100%, which renders them unsuited for ACT.

1.1.5 Piezoelectric transducers

Ultrasound waves can be transmitted and received with a device called a transducer; an electroacoustic transceiver that converts electrical energy to mechanical energy, and vice versa. Throughout the remainder of the thesis, only bulk piezoelectric transducers will be considered, also referred to as piezoceramic transducers.

The most commonly available piezoelectric material is lead zirconate titanate, abbreviated PZT. Based on the performance, the PZT is classified as Navy Type I, II, III, V, and VI [23]; where, generally, Type I and III are used for high-power applications (e.g., HIFU, lithotripsy, histotripsy), and Type II, V, and VI are used for imaging and low-power applications. New piezoelectric materials such as single-crystal ferroelectrics [24] and lead-free piezoceramics [25] are constantly being researched and certain single-crystal materials are commercially available (e.g., CTS, Bolingbrook, USA) as well as lead-free alternatives (e.g., PI Ceramic GmbH, Lederhose, Germany).

Employing the piezoelectric effect, a plethora of different transducer designs exist and, generally, the application at hand defines the complexity of the transducer. For example, transducers used in non-destructive testing may be comprised of only one solid piezoceramic, while transducers used for generating real-time 3-D images can consist of thousands of individual active piezoceramic elements each connected to their respective electrical ports [26].

However complex the transducer may be, most medical transducers are comprised of mainly the same key components: an active and polarised piezoceramic (solid, compos-

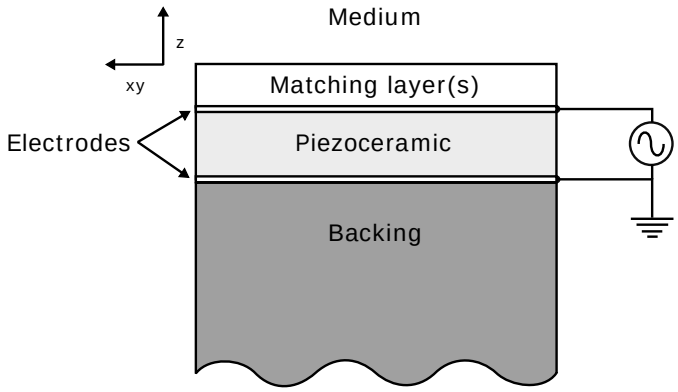

Figure 1.2: Simplified schematic of a bulk piezoceramic transducer showing the key components most transducers are comprised of.

ite or elements in an array) with metal electrodes on each face, one or a few mechanical impedance transformers in between the piezoceramic and the radiation medium, referred to as matching layers, and another passive material on the rear face of the transducer, referred to as backing. In Fig. 1.2, a simplified schematic of the key components in a conventional ultrasound transducer is shown. In addition, the transducer needs to be connected to electrical transmit-receive ports, electrically tuned and shielded, and be accommodated in a housing.

The matching and backing layers are typically made of a passive polymeric material with or without inorganic fillers [27], and the material choice and number of layers has a significant effect on the transducer performance [28]. Depending on the application, the matching and backing layers are used to both shape and shorten the pulse accordingly. For therapeutic application, the shape of the pulse is not necessarily very critical as multiple pulse-cycles are generally used; however, for ultrasound imaging applications the shape and length of the pulse are directly correlated with the image quality. A reduction in the pulse duration (i.e., an increased bandwidth) increases the spatial resolution, and a low time-sidelobe level relative to the main pulse is important to avoid image degradation [ch.5.5] [1]. Significant research attention has been directed at obtaining optimum values for the matching layers' acoustic impedance values, either as analytical expressions [29–31] or using numerical optimisation methods [32–36].

A fundamental property of the piezoceramic is its ability to resonate. When subjected to an external electric field, the piezoceramic resonates at approximately each odd-numbered half-wave interval

$$N \times \frac{\lambda}{2}, \tag{1.1}$$

where $N = 1, 3, \ldots, \infty$. If $N = 1$, the resonance is referred to as the fundamental, and if $N > 1$, the resonances are referred to as harmonics or overtones. Due to the resonating properties, a fundamental limitation of bulk piezoceramic transducers is the range of frequencies with a *usable* amplitude, referred to as bandwidth and is defined as

$$\text{bandwidth} \equiv \frac{f_2 - f_1}{f_c}, \tag{1.2}$$

where f_1 and f_2 are the lower and upper -3 dB frequency points from the maximum of the power spectrum, respectively.

As an example of the bandwidth limitation of bulk piezoceramic transducers, we will use 1-D simulations of the electro-mechanical transfer function $H = U/V$, where U is the complex normal particle velocity at the face of the transducer, and V is the complex input voltage to the transducer's electrical terminals. In Figure 1.3, the magnitude of $|H|$ is shown for two transducers. The PZT transducer is comprised of a Ferroperm™ Pz27 (Meggitt Sensing Systems, Kvistgård, Denmark) solid piezoceramic with two matching layers optimised according to DeSilets' guidelines [29], and the transducer is air-backed. The 1-3 composite single crystal transducer is comprised of a 65% 1-3 piezo-polymer composite [37] where the piezoceramic is a PMN-32% PT Type B single crystal (CTS, Bolingbrook, USA). Two matching layers are used, however, the matching layers are optimised to maximize the bandwidth on the expense of ripple in the passband [34], and an absorbing backing is used to reduce the passband ripple. The respective -3 dB bandwidths are 63% and 109% for the solid PZT and 1-3 composite single crystal transducers, respectively. Although the 1-3 composite single crystal transducer exhibits a bandwidth slightly larger than 100%, use of single crystals as well as 1-3 composites are not always possible. For example, the curie temperature of PMN-32% PT Type B is 130-140°C, which may render it unsuited for high-power therapeutic applications.

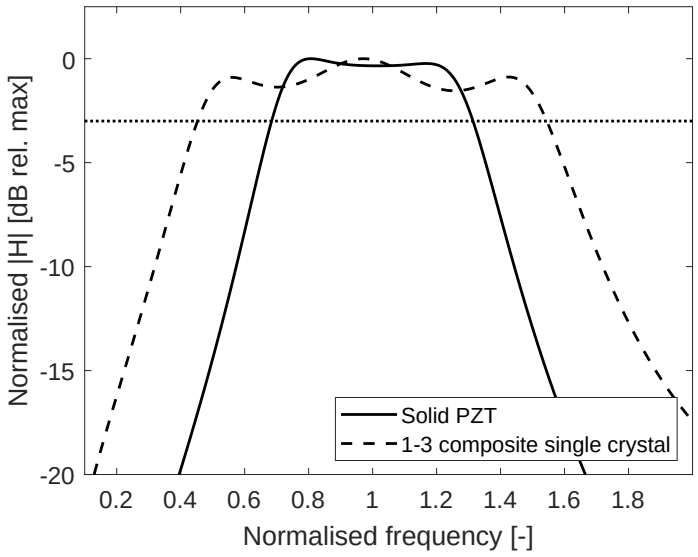

Figure 1.3: 1-D simulation of the magnitude of the electro-mechanical transfer function $|H|$ for a transducer comprised of a solid PZT compared to a transducer comprised of a 1-3 piezo-polymer composite single crystal. The magnitude is normalised to the respective maxima, and the frequency is normalised to the respective centre frequencies. The horizontal dotted line indicates -3 dB from the maximum.

1.1.6 Dual-frequency piezoceramic transducers

To overcome the challenges with the bandwidth limitation of conventional piezoceramic transducers, so-called dual-frequency transducers have been suggested in the literature. Throughout, the term *dual-frequency transducer* will be used for any transducer that accommodates two usable frequency bands in the same device, where the two frequency bands could not have been realised using only the fundamental frequency band. Typically, this means that the high-frequency component is more than 3-4 times that of the low-frequency component.

In Figure 1.4, simplified schematics of different stacked dual-frequency transducer designs available in the literature are shown. The schematics indicate solid piezoceramic layers; however, they are representative for composites and arrays alike. Design and construction layers, such as matching and backing, housing, electrical connections, etc., are omitted for clarity. Each design is discussed individually below.

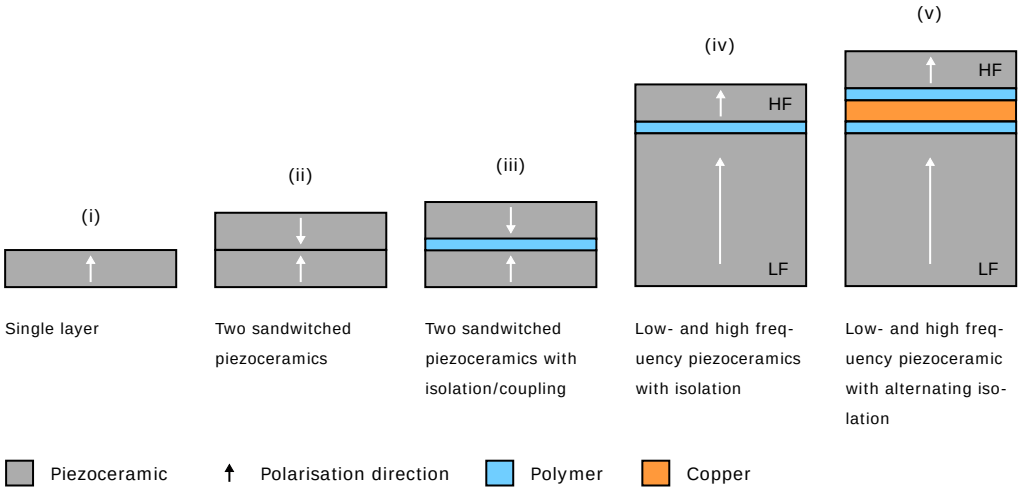

Figure 1.4: Simplified schematics of different stacked dual-frequency transducer designs.

(i) A single active piezoceramic where the inherent harmonics may be utilized for dual-frequency excitation [38]. In magnitude, the harmonics are comparable to the fundamental. The absolute bandwidth of the harmonics are also comparable to the fundamental; however, the relative bandwidth decreases with $\sim N^{-1}$. The reduction in relative bandwidth results in pulses that rings, which, generally, renders the harmonics not suitable for imaging applications.

(ii) Two piezoceramics of comparable thicknesses and with reversed polarisation are stacked on top of each other [39–42]. The potential of this design is that a low-frequency band can be achieved by exciting both piezoceramics together (electrically in parallel and mechanically in series), and a high-frequency band can be achieved by exciting either the front or the back piezoceramic. If both piezoceramics are excited together, a half-wave resonator is realised and the low-frequency resonance frequency is reduced with a factor of two compared to the resonance frequency of the individual layers. By using piezoceramics of different thicknesses, the low-frequency resonance frequency can be reduced with more than two compared to the resonance frequency of the thinnest layer [40]. For the high-frequency excitation, arguments can be made for using either the top or bottom piezoceramic.

Matching this transducer to the medium is, however, challenging. The most conventional approach is to use $\lambda/4$ layer(s) for the high-frequency band, and, effectively, $\lambda/8$ layer(s) for the low-frequency band [41]. With this choice, the low-

frequency band will be narrow resulting in pulses that rings; however, for applications such as Doppler, HIFU, Histotripsy, and ACT, ringing pulses are not necessarily detrimental to performance.

(iii) Two piezoceramics of comparable thicknesses are stacked on top of each other with a soft polymeric coupling layer sandwiched in between the piezoceramics. We will refer to this design as a coupled resonator transducer (CRT). The CRT exhibits immediate resemblance to the design in (ii), where a low-frequency band can be achieved by exciting both piezoceramics together and a high-frequency band can be achieved by exciting either the front or the back piezoceramic. Compared to the design in (ii), the natural choice is to use the front piezoceramic for the high-frequency band. Although the CRT resembles the design in (ii), certain benefits exist:

1) The ratio of the high-frequency to low-frequency (HF-to-LF) resonance frequency can exceed 2:1 by tailoring the thickness and stiffness of the coupling layer relative to the piezoceramics.

2) A good choice for the coupling layer thickness is $\lambda/4$ (relative to the high-frequency) because it allows for mechanical impedance transformation [47]. The mechanical impedance presented to the front piezoceramic at the boundary towards the coupling layer will be lower compared to the impedance of the coupling layer itself; however, close to the centre frequency, where the back piezoceramic is $\lambda/2$, the mechanical impedance presented to the front piezoceramic at the boundary towards the coupling layer will be higher compared to the impedance of the coupling layer. Because of this, the acoustical energy is predominantly reflected off the boundary between the front piezoceramic and the coupling layer, except for in a narrow frequency range ($\sim$5%) around the centre frequency where the acoustical energy propagates into the coupling layer and the back piezoceramic.

3) The piezoceramics can have different thicknesses, which, together with the coupling layer's thickness and stiffness, may be taken advantage of to increase the HF-to-LF ratio.

The CRT has not received significant attention in the literature, although some publications exist. Paco et al. [43] developed a lumped element model of a low-frequency coupled resonator filter. Powell et al. [44] developed a 1-D modelling approach for multi-layered piezoceramic transducer structures, therein investigating a CRT. Wang et al. [45] realised a bi-frequency linear array using two piezoceramic layers with a passive polymeric layer sandwiched in between the active layers. However, upon manufacturing, the polymeric layer was significantly thinner compared to $\lambda/4$, which resulted in a HF-to-LF ratio of $\sim$2.5.

As was discussed with respect to the design in (ii), matching this transducer to the medium is challenging. Also here, the natural choice is to match the high-frequency band to the medium using $\lambda/4$ layer(s). For the low-frequency band, the consequence of this choice is that the matching layers are significantly thinner than $\lambda/4$ resulting in a narrow low-frequency band.

(iv) Two piezoceramics of significantly different thicknesses are stacked on top of each other with a passive polymeric *isolation*[1] layer sandwiched in between the piezoceramics [46, 47]. The HF-to-LF ratio is predominantly defined by the half-wave resonance of the high- and low-frequency layers.

Using this design, Azuma et al. [46,48] realised a 0.5 MHz and 2 MHz dual-frequency transducer with a HF-to-LF ratio of 4:1. Numerical simulations were used to optimise the low-frequency wave propagation through the stack while simultaneously optimising for the high-frequency pulse. Based on the simulations, a $\lambda/10$ isolation layer of acoustic impedance 3 MRayl to 4 MRayl was chosen.

At the North Carolina State University, this design has been taken advantage of in several different applications: Ma et al. [49, 50] (2014, 2015) reported on intravascular dual-frequency transducers for super-harmonic contrast imaging and acoustic angiography. Wang et al. [51] (2015) realised a 6.5 MHz and 26 MHz dual-frequency transducer for acoustic radiation force imaging. Lindsay et al. [52] (2017) realised a 4 MHz and 20 MHz dual-frequency transducer for endoscopic ultrasound imaging

[1]The term isolation layer as compared to coupling layer is adapted here because the objective of the layer is to reduce the high-frequency reverberation inside the transducer.

using microbubble-specific super-harmonic signals. Li et al. [53] (2018) realised a dual-frequency linear array for acoustic angiography for prostate cancer evaluation transmitting at 3 MHz and receiving at 15 MHz.

At the Norwegian University of Science and Technology (NTNU), this design has also been investigated in relation to the SURF technology [47, 54]. Myhre et al. [47] showed that a good choice for the isolation layer thickness is $\lambda/4$. With this choice, the impedance presented to the high-frequency piezoceramic at the boundary to the isolation layer is lower compared to the actual impedance of the isolation layer.

(v) Two piezoceramics of significantly different thicknesses are stacked on top of each other with alternating polymeric and metallic isolation layers sandwiched in between the piezoceramics [47]. The design exhibits immediate resemblance to (iv); however, use of the metallic layer results in a reduction in the high-frequency reverberation within the transducer. Moreover, if the HF-to-LF ratio is larger than 7:1, the low-frequency piezoceramic matches to the medium through a spring-mass interaction [47].

Apart from the stacked dual-frequency designs, several publications and commercially available products exist where the high- and low-frequency piezoceramics, or array elements, are placed next to one another. Sonic Concepts Inc. (Bothell, USA) has specialised in producing therapy transducer for the biomedical market since 1986 and delivers focused bowl transducers with a detachable imaging array placed in the centre of the bowl. Bouakaz et al. [55] (2002), interleaved the high- and low-frequency array elements, realising a 0.9 MHz and 2.8 MHz dual-frequency transducer to enhance the scattered power from contrast agents (gas-filled microbubbles) to the scattered power from the tissue. Instead of interleaving the array elements, Stephens et al. [56] (2006) realised a 1.5 MHz and 5.3 MHz dual-frequency transducer by placing one row of a high-frequency imaging array in the middle surrounded by two rows of therapeutic low-frequency arrays; the low-frequency was used for bubble manipulation to enhance the efficacy of drugs.

Beyond PZT transducers, Akiyama et al. [57] prototyped an ultra-broadband transducer for imaging using the higher-order tissue harmonics. The transducer was comprised of a

conventional circular single-element PZT disk with a PVDF mounted on top. The PZT was used for transmission, and the PVDF was used for reception of up to the 4^{th} harmonic. A similar design where the PVDF is exchanged for a CMUT is currently under development at USN [58].

1.2 Objectives and tasks

The main objective of the current thesis has been to investigate dual-frequency ultrasound transducer designs for therapeutic purposes, therein combined imaging and therapy systems, and new drug delivery systems where conventional transducer designs fall short due to limited bandwidth. Although some dual-frequency HIFU transducers systems exist commercially (e.g., Sonic Concept Inc.), they are generally comprised of a large low-frequency bowl-transducer with an imaging array placed in the centre. Generally, they occupy a large space which may not be feasible for all applications. Because of this, the emphasis has been on the stacked dual-frequency transducer designs (cf. Fig. 1.4). The main benefit of stacked dual-frequency transducers is a reduced footprint compared to the designs where the low- and high-frequency layers are placed next to one another. Even though several dual-frequency transducer designs have been suggested in the literature, the designs are generally not readily available as products, and can thus not be acquired by research groups, for example, investigating new drug delivery systems [21]. As a result of this, a major part of the work has been to manufacture ultrasound transducers.

The transducer manufacturing methods used at the ultrasound laboratory at USN consists predominately of purchasing piezoceramics and filled polymer composites for the matching and backing layers. The composites are diced and ground to obtain the required spatial dimensions before subsequent layers are glued together using an epoxy adhesive. The method is considered accurate; however, time-consuming, and, most importantly, dependent on external suppliers. The latter became an issue during the course of the work when the supplier of filled polymer composites could not deliver new composites. From this, a desire to create new manufacturing methods arose which were less dependent on suppliers of filled epoxy systems. Recipes and methods for producing

matching layers were developed which have been handed down to the ultrasound group at USN, some of which are described in Sec. 1.6.

Conventional transducers have been investigated for a long time, and several publications addressing the optimisation and analysis of such transducers exist [28–31]. However, the design guidelines for conventional transducer are not always applicable to dual-frequency transducers. Because of this, we wanted to explore if numerical optimisation methods could be taken advantage of to optimise dual-frequency transducers.

Based on this, the following major tasks have been identified through the course of the work:

1. Design a numerical optimisation method applicable to complex transducer designs, therein dual frequency transducers.
2. Learn and develop manufacturing methods for ultrasound transducers.
3. Design, build, and test a dual-frequency transducer system for pre-clinical testing of Acoustic Cluster Therapy on tumours in mice.
4. Investigate a coupled resonator transducer intended for Acoustic Cluster Therapy or as a combined imaging and therapy transducer.

1.3 Transducer modelling

Throughout the course of the work, transducer modelling has been a key tool to investigate, evaluate, and optimise different dual-frequency transducer designs. Several modelling approaches have been employed, ranging from 1-D analytical evaluation to 3-D FEA modelling. Generally, a 1-D simulation approach has been used, followed up with 2-D and 3-D FEA to evaluate the feasibility of reducing the 3-D structure to a 1-D equivalent. The 1-D transducer models have been implemented as Matlab (The MathWorks, Inc. Natick, USA) scripts, or run on a Matlab program written by Tonni F. Johansen, referred to as xTrans [59]. Field II [60, 61] was used to analyse the sound field, and a commercial FEA software package (Comsol AB, Stockholm, Sweden) was used for the 2-D and 3-D simulations.

Table 1.2: Transmission line parameters for a bulk piezoceramic operating in the thickness extensional mode. Note that the impedances are also representative for an elastic plate. All variables are defined at the beginning of the thesis in the *List of symbols*.

$C_0 = \epsilon_{33}^S A/l$	Clamped capacitance
$N = h_{33} C_0$	Electro-mechanical turns ratio
$Z_0 = \rho c A$	Mechanical impedance
$Z_a = iZ_0 \tan(kl/2)$	Distributed mechanical impedance
$Z_b = -iZ_0 / \sin(kl)$	Distributed mechanical impedance

1.3.1 1-D distributed equivalent circuit models

For bulk piezoceramic transducers vibrating in the thickness extensional mode, the 3rd dimension corresponds to both the polarisation and displacement direction of the material. If the piezoceramic is much thicker or thinner compared to the remaining two dimensions, physical effects such as fringing fields and edge effects can often be neglected, and the piezoceramic can be satisfactorily modelled by only considering what happens in the 3rd dimension.

The most known 1-D equivalent models for piezoceramic transducers operating in the thickness extensional mode are suggested by Mason [62], Krimholtz, Leedom, and Matthaei [63], referred to as the KLM-model, and Redwood [64]. Common for the models is the use of equivalent circuit representations to visualise the transducer structure. In the current work, only the model suggested by Mason has been used.

In Figure 1.5 (a), a 1-D distributed equivalent circuit model [62] of a piezoceramic slab vibrating in the thickness extensional mode is shown. The parameters in Fig. 1.5 are defined in Table 1.2. The disk is embedded in a vacuum; however, an extension of this model to include matching and backing layers and radiation medium are straight forward. As an example of this, in Fig. 1.5 (b), a 1-D distributed model of an elastic plate terminated in a load of acoustic impedance Z_L is shown. The elastic plate can be attached to the piezoceramic plate, serving as a matching layer radiating in a medium of acoustic impedance Z_L.

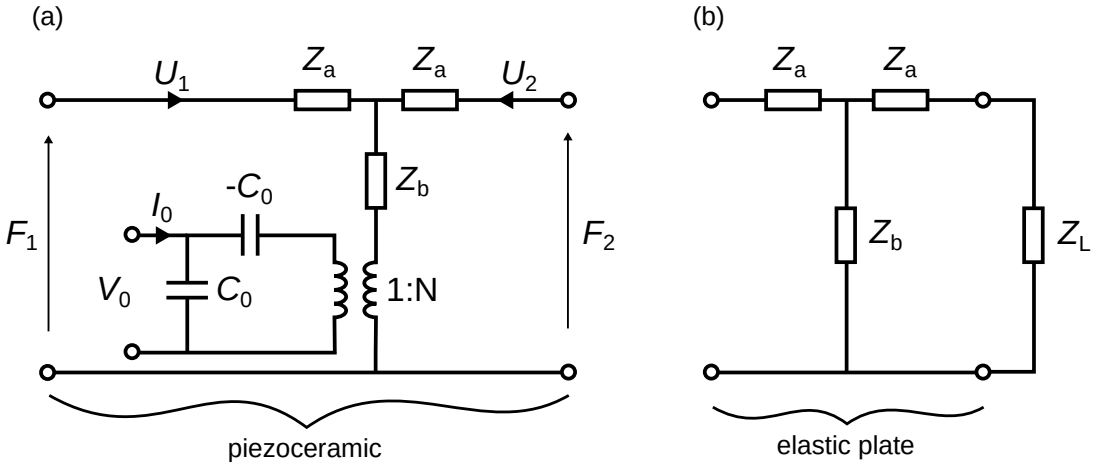

Figure 1.5: (a) 1-D distributed equivalent circuit model of a piezoceramic operating in the thickness extensional mode suggested by Mason [62]. (b) Transmission line representation of an elastic plate terminated in a load of acoustic impedance Z_L.

1.3.2 Finite element analysis

Finite element analysis (FEA) is a powerful simulation tool that can be used to model and analyse more complex structures compared to the 1-D models. Generally, FEA consists of reducing the complexity of partial differential equations and solving the problem numerically using a finite number of elements [65]. In the current work, the commercial FEA package Comsol Multiphysics (Comsol AB, Stockholm, Sweden) was used.

In Comsol, the piezoceramic material is modelled by use of the piezoelectric constitutive equations, which in the stress-strain form, or e-form, is [66]

$$\begin{aligned} T_p &= C_{pq}^E S_q - e_{kp} E_k, \\ D_i &= e_{iq} S_q + \epsilon_{ik}^S E_k, \end{aligned} \tag{1.3}$$

where $p = ij$ and $q = kl$; p, q take the values $1, 2, \ldots, 6$, and i, j, k, l take the values $1, 2, 3$. Generally, the material and tensor symmetry reduces the number of independent material parameters [67]. For a piezoelectric material, such as PZT, five stiffness constants ($C_{11}^E, C_{12}^E, C_{13}^E, C_{33}^E, C_{44}^E$), three piezoelectric constants (e_{31}, e_{33}, e_{51}), and two permittivity constants (ϵ_{11}^S, ϵ_{33}^S), as well as density ρ, have to be defined. An elastic material, such as a polymer, is modelled as an isotropic material, hence only two independent stiffness parameters (C_{11}, C_{44}) have to be defined. All material parameters are associated with losses, which are includes using a complex notation [68].

However powerful FEA may be, the results are strongly dependent on the accuracy of the material parameters used in the simulations. Because of this, important material properties were estimated using numerical inversion techniques [69] or by use of acoustical measurements [70, 71].

1.3.3 Elasticity

Hooke's law of elasticity relate the stress T to the strain S for some stiffness tensor C that characterises the material, which in Voigt notation reads [67]

$$T_p = C_{pq} S_q \qquad (p, q = 1, 2, \ldots, 6). \tag{1.4}$$

For a material experiencing a strain in the 3rd direction due to a stress in the 3rd direction, Eq.(1.4) reduces to

$$T_3 = C_{33} S_3, \tag{1.5}$$

where $C_{33} = c_{33}^2 \rho$ is the stiffness constant in the 3rd direction, and c_{33} is referred to as the longitudinal speed of sound. Another common representation of Hooke's law is

$$F_r = -Kx, \tag{1.6}$$

where F_r is a restoring force working on a mass displaced x from equilibrium, and $K = C_{33} A/l$ is the spring constant. Reducing a physical resonator to a lumped model consisting of a simple spring and a mass can generally be performed if the physical dimensions are smaller than about one-quarter of a wavelength [72, ch.7.1.1]. If several masses are connected through different springs, the system is considered coupled and can be solved using simultaneous equations [73]. In the current work, both of this was taken advantage of when we analysed a coupled resonator transducer (cf. Paper D).

1.4 Numerical optimisation method

Numerical optimisation methods can be important tools when dealing with complex problems because the complexity can be reduced to tangible quantities. In the current work, the transducer was reduced to a two-port network where the input to the system was the complex electrical excitation voltage V and the output of the system was the complex particle velocity at the face of the transducer U. The ratio U/V is the electro-mechanical

transfer function $H = |H|\exp(i\theta)$, where $|H|$ is magnitude and θ is the phase angle between the voltage and the particle velocity.

To optimise a transducer numerically, an optimisation criterion has to be defined. The optimisation criterion will cultivate certain qualities of the transducer beneficial for a specific application. Since most dual-frequency transducer systems require an imaging modality, we crafted an optimisation criterion based on linearising the phase θ. The motivation for optimising a transducer for a linear phase was to obtain short pulses with low time-sidelobe levels [74], ideal for imaging purposes.

The optimisation was performed by simulations of the electro-mechanical transfer function H. In Fig. 1.6, an example of $|H|$ and θ for a conventional single-layer transducer with two matching layers radiating in water is shown. The phase $\theta = \theta(\bar{x})$ is a function of all the physical parameters that describes the transducer, where $\bar{x} = x_1, x_2, x_3, \ldots, x_j$ is a vector containing all the transducer parameters. To linearise θ, we first quantify how much θ deviates from an ideal linear phase. The ideal linear phase

$$\theta_l = \beta_0 + \bar{f}\beta_1, \tag{1.7}$$

is a regression line fitted to θ over a -3 dB fitting range, where β_0 and β_1 are the coefficients of the regression line, and $\bar{f}$ is a frequency vector in the fitting range. The optimisation is performed by searching the parameter space $\bar{x}$ that minimizes the difference between the ideal linear phase θ_l and the transducer phase θ, mathematically expressed as

$$\arg\min_{\bar{x}} E(\bar{x}), \tag{1.8}$$

where $E(\bar{x})$ is referred to as the cost function to be minimized, and is defined as

$$E(\bar{x}) = \frac{1}{m}\sum_{i=1}^{m} |\theta(\bar{f}_i, \bar{x}) - \theta_l(\bar{f}_i, \bar{x})|, \tag{1.9}$$

where E is the average absolute difference between the ideal linear phase $\theta_l(f_i, \bar{x})$ and the simulated transducer's spectral phase $\theta(f_i, \bar{x})$ summed over m discrete frequency points in the -3 dB fitting range.

The optimisation method is implemented in Matlab and the optimisation is performed by a global optimisation algorithm implemented in Matlab's Optimisation Toolbox. A global

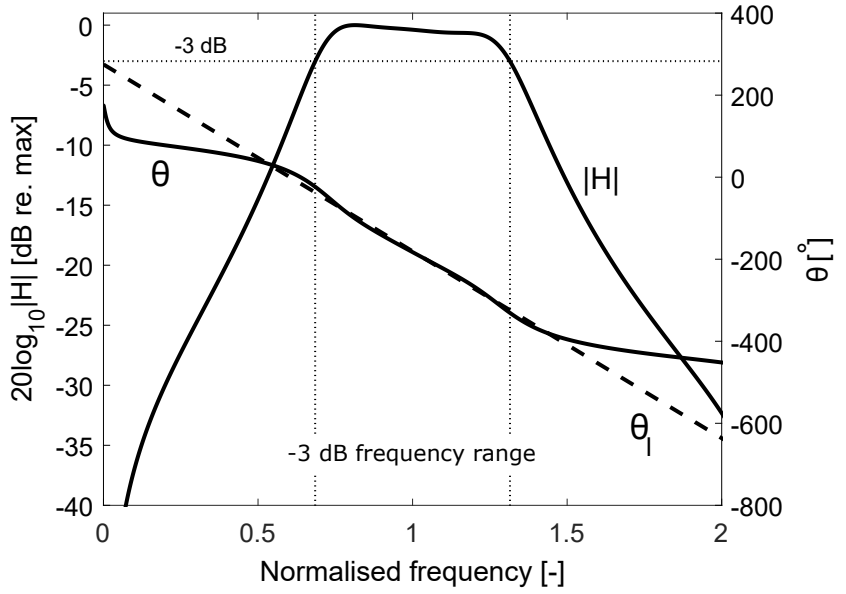

Figure 1.6: An example of the electro-mechanical transfer function H showing the ideal linear phase θ_l obtained by linear regression of the transfer function phase θ in the -3 dB frequency range.

optimisation algorithm is essential to avoid converging in a local minimum, as compared to the global minimum. A flowchart of the optimisation method is shown in Fig. 1.7.

The above description is representative for optimising a conventional transducer with one frequency band. An extension of the linear phase method to encompass two frequency bands is described in Paper C [75]. The essential extension of the optimisation method is reproduced below. The cost function E to be minimised according to Eq.(1.8) is

$$E(\bar{x}) = \sum_{n=1}^{2} \alpha_n E_n(\bar{x}), \tag{1.10}$$

where $E(\bar{x})$ is the sum of the cost functions in the first $E_1(\bar{x})$ and second $E_2(\bar{x})$ frequency bands, respectively, and α_1 and α_2 represents weights that can be applied to each of the cost functions. Both E_1 and E_2 are calculated using Eq.(1.9) after both the transducer phase θ and the ideal linear phase θ_l has been obtained in each of the frequency ranges.

In the current work, the optimisation was predominantly performed using 1-D simulations [62]; however, if the transducer can not adequately be modelled as a 1-D model,

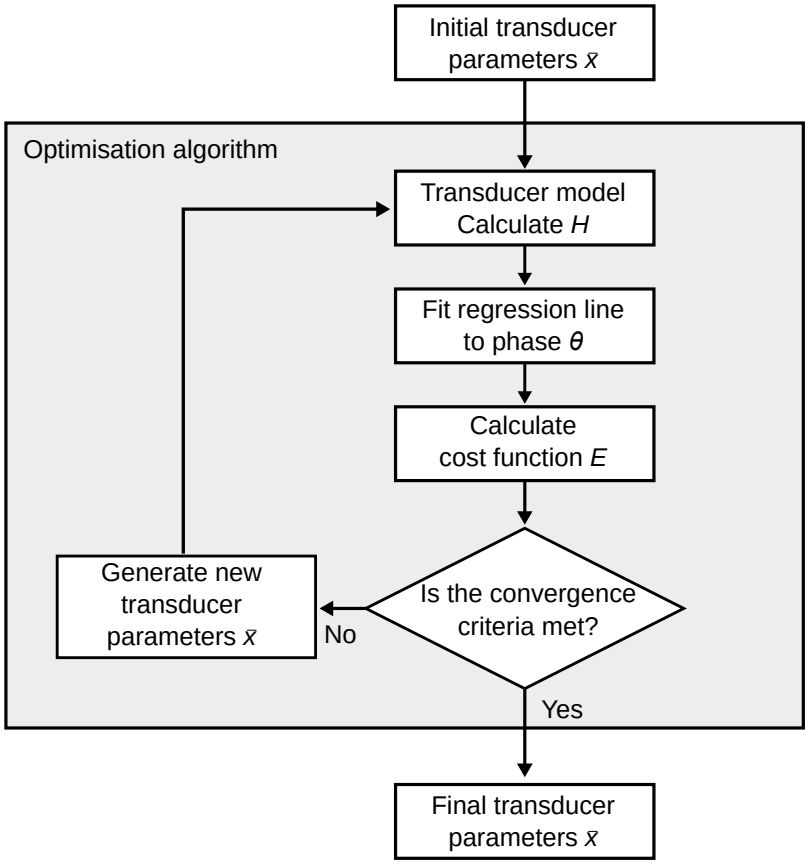

Figure 1.7: Flowchart of the numerical optimisation method.

2-D or 3-D FEA simulations can be used at the expense of an increase in the computation time.

1.5 Acoustical measurements

Acoustical measurements were used throughout the course of the work to compare the manufactured transducers with the design simulations. Predominantly, hydrophone measurements were used.

1.5.1 Hydrophone measurements

The hydrophone measurements were conducted in an AIMS III measurement system from Onda (Onda Corporation, Sunnyvale, USA) controlled through a Matlab interface. A schematic of the measurement set-up is shown in Fig. 1.8, where a signal generator connects to an E&I 2100L power amplifier (Electronics & Innovation, Ltd., Rochester, USA) with 50 dB gain which connects to the transducer under test. The transducer transmits

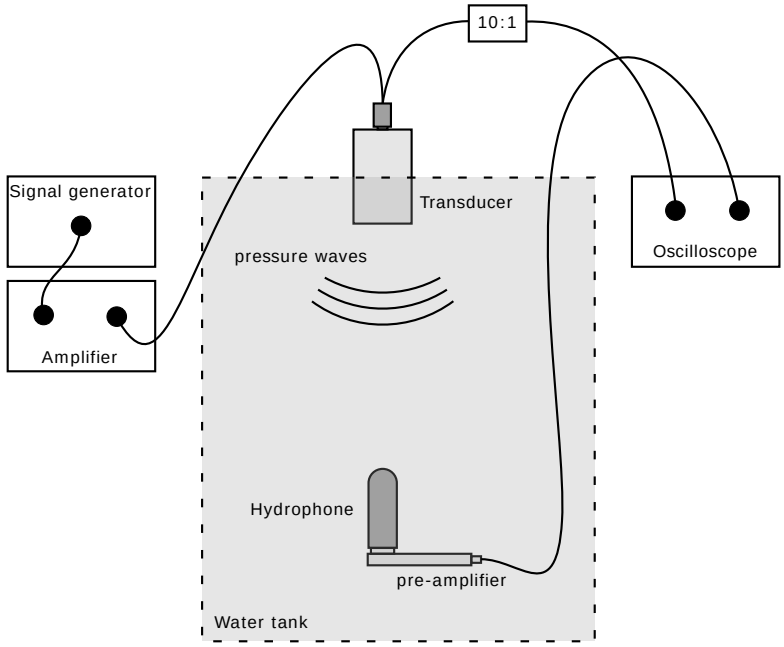

Figure 1.8: Schematic of the hydrophone measurement set-up.

pressure waves received by an Onda HGL0200 *Golden Lipstick* hydrophone connected to an Onda AG-2010 pre-amplifier connected to a PicoScope oscilloscope (Pico Technology, Cambridgeshire, UK). The electrical input signal to the transducer, $v_0(t)$, was recorded using a 10:1 RT-ZP03 probe (Rhode & Schwarts USA, Inc., Columbia, USA). The on-axis spectral pressure at the face of the hydrophone, $P(f, z)$, was obtained by deconvolving the spectrum of the recorded voltage traces with the hydrophone and preamplifier calibration data. Measurements of the magnitude of the electro-mechanical transfer function H was obtained by

$$|H(f)| = \Big|\frac{P(f,z)}{V_0(f)D(f,z)Z_L}\Big|, \tag{1.11}$$

where $V_0(f)$ is the spectrum of the measured voltage at the transducer terminals, $D(f, z)$ is diffraction correction, and Z_L is the characteristic impedance of water.

1.5.2 Diffraction correction

The sound field produced from a finite aperture is characterised by peaks and troughs, generally referred to as interference. Moreover, when a receiver of a finite aperture is used to measure the sound field, the measurement may differ from the sound field associated with an infinitesimal point. For accurate measurements, the pressure variations of using finite apertures should be accounted for and is referred to as diffraction correction.

The diffraction correction is defined as [76–78]

$$D(f,z) \equiv \frac{\langle P(f,x,y,z)\rangle}{\rho c U}, \tag{1.12}$$

where $\langle\rangle$ denotes the average of the sound pressure over a spatial region equal to the receiver aperture from a coaxial transmitter mounted in a rigid and infinite baffle, and $\rho c U$ is the pressure amplitude of a plane wave. Exact solutions to D for a circular transmitter and receiver pair of identical [77] or different [78] sizes exist. In the current work, for circular apertures, D was evaluated using both the approximate [76] and exact [77, 78] approaches; for square apertures, numeric integration of the Rayleigh integral [79, ch.7.4] was performed.

1.6 Matching layer production

The following sections contains some of the key methods used for producing matching layers. The methods were developed during the course of the PhD and were motivated by a desire to be less dependent on suppliers of filled epoxy systems. Initially, we were not able to reproduce the recipes given by Wang et al. [27] because the fillers sedimented in the epoxy. To resolve this, we had to pre-treat the epoxy resin prior to adding the fillers — a technique not transparent in the acoustical literature.

The intention of this section is to help expedite future endeavours in working with filled epoxy systems suitable for acoustic matching layers; however, complete recipes are not offered.

1.6.1 Epoxy

Epoxy resins are a highly versatile class of polymers found in many applications; colloquially, it's a two-component glue. A solid epoxy is obtained by mixing the resin with a hardener (reactant) which induce a chemical thermosetting curing process resulting in cross-linking of the polymer chains [80, ch.1]. Generally, curing is performed in elevated temperatures to advance cross-linking. A thorough description of the different polymers and epoxy classes are beyond the scope of this text, and the reader is referred to the book *Rheology of Filled Polymer Systems* by Aroon V. Shenoy [80].

Table 1.3: Acoustic properties of a few commercially available epoxies.

		Longitudinal			Shear	
	ρ	c	$Z = \rho c$	α	c	α
	[kg/m^3]	[m/s]	[MRayl]	[dB/cm/MHz]	[m/s]	[dB/cm/MHz]
EPO-TEK 301-2[1]	1143	2600	3.0	3.8	1221	13.5
EPO-TEK 301-2[2]	1150	2650	3.1	3.2	1230	12
Spurr's epoxy[1]	1084	2260	2.5	6.0	-	-
Eccobond 45/15 rigid[3]	1090	2420	2.6	4.1	-	-
Eccobond 45/15 semi-rigid[3]	1050	2180	2.3	7.0	-	-
Eccobond 45/15 flexible[3]	1030	2030	2.1	12.2	-	-

[1]Measured at USN by Kenneth K. Andersen.

[2]Wang et al. [27].

[3]Measured at USN by Ebne A. Ashad [81].

A plethora of different epoxies and hardeners exists, as well as different vendors with their own name brands. Because of this, it can be challenging to choose and later obtain a suitable epoxy for a specific application. A good place to start is the *Tables of Acoustic Properties of Materials* offered by Onda, where acoustic properties of a wide range of materials, including commercially available epoxies, are offered. In Table 1.3 of the current thesis, acoustic properties of some selected epoxies are shown. The measurements conducted at USN follow the work by Wu et al. [71] and He et al. [71]. EPO-TEK 301-2 (Epoxy Technology Inc., Billerica, USA) is a low-loss rigid epoxy type with low viscosity, suitable for matching layer production; however, it has a relatively high acoustic impedance. By use of Eccobond 45/15 in a 100:150 mix ratio of resin to hardener, referred to as *flexible*, an acoustic impedance of $2.1\,\mathrm{MRayl}$ was obtained [81]. In the flexible formulation, the cured epoxy has a Shore hardness lower than 60, i.e., similar to hard rubber. A relatively soft material is often associated with a high loss; however, for prototype applications, when a low impedance is required, Eccobond 45/15 is a fair candidate.

1.6.2 Fillers

From an acoustical point of view, the purpose of adding fillers to the epoxy matrix is to tailor the characteristic acoustic impedance $Z = \rho c$ to a specific property. Generally, a

material suited for matching layers should have a low acoustic loss while a material suited for backing should have a high acoustic loss. Aluminium oxide (Al_2O_3) and tungsten (W) are commonly used as fillers for the matching and backing layers, respectively [27]. Use of either Al_2O_3 or W will increase Z, however, if the desire is to lower Z, hollow glass spheres can be used [82, 83].

1.6.3 Sedimentation of fillers

If the viscosity of the epoxy is too low, the added filler may sediment in the epoxy matrix; moreover, if the epoxy is cast directly to a substrate, it may also be desirable to increase the viscosity of the epoxy to limit unwanted flow. Aerosil 200 fumed silica (Evonik Resource Efficiency GmbH, Essen, Germany) was used as a thixotropic agent to increase the viscosity of EPO-TEK 301-2 and to prevent sedimentation of Al_2O_3. Only a small amount of fumed silica ($\sim$1-2% relative to weight) is needed to significantly increase the viscosity of the epoxy and to avoid sedimentation. Interestingly, the addition of fumed silica to the epoxy matrix exerts only a small effect on the acoustic properties of the composite, see Table 1.4.

Measuring the viscosity of liquids can be challenging, and was not performed. However, what can be said is that EPO-TEK 301-2 exhibits a viscosity (225-425 cPs) slightly higher than water, i.e., a pourable free-flowing liquid. If 5% of fumed silica is added to EPO-TEK 301-2, the composite exhibit a viscosity similar to mustard, i.e., a liquid that does not flow, generally impractical with respect to matching layer production.

In conclusion, adding 1-2% percent of fumed silica to EPO-TEK 301-2 resolved the issue with the sedimentation of Al_2O_3; moreover, the composite was possible to degas and transfer to casting moulds.

1.6.4 Mixing

To achieve a homogenous composite, proper mixing is crucial. Planetary mixers take advantage of the centrifugal force to mix different substances together. A SpeedMixer DAC 150.1 FVZ-K was purchased to USN, mainly funded by the Norwegian PhD Network on Nanotechnology for Microsystems founded by the Research Council grant nr.: 221860/F60.

Table 1.4: Measured acoustic properties of EPO-TEK 301-2 filled with fumed silica shown in percent relative to weight. Measurements performed at 5 MHz.

Percent of fumed silica	c [m/s]	ρ [kg/m^3]	$Z = \rho c$ [MRayl]	α [dB/cm]
0%	2600	1143	2.97	19.0
1%	2598	1149	2.99	18.5
2%	2600	1157	3.01	18.2
3%	2610	1159	3.02	18.4
4%	2619	1165	3.05	18.5

Generally, a mixer with a degassing property is preferable for matching layer production; however, this comes at an additional cost, which was outsides of the budget. The Speed-Mixer DAC 150.1 FVZ-K does not degas the mixtures.

1.6.5 Degassing

After mixing, the composite may be filled with air bubbles which should be removed for consistent results and to avoid unnecessary losses in the composite. To degas the mixed composites, a vacuum chamber was built. In essence, the vacuum chamber is comprised of a metal pipe connected to a vacuum pump. A door on the end of the pipe allows samples to be inserted into the vacuum chamber which seals off with an O-ring and clamps. A pressure of 10-100 mTorr is achieved after about 2-4 min if no sample is present. For comparison, the atmospheric pressure is 760 Torr.

If a high-viscosity epoxy is used, or if a high volume percent of fillers are added to the epoxy, degassing can be difficult to perform since the mixture does not release the air bubbles; rather, it rises like foam when subjected to decreasing pressure. To aid in releasing the air bubbles, a BYK-A 501 (BYK-Chemie GmbH, Wesel, Germany) de-foaming agent was used. Generally, one drop ($\sim$1% of the total volume) of BYK-A 501 is sufficient.

When epoxy is subjected to decreasing pressure, the chemical compounds will evaporate when the vapour pressure is equal to the surrounding pressure. The vapour pressure varies for the epoxy resin and hardener, and for different epoxy systems. If one substance

is evaporated, it may negatively affect the cured epoxy. It is advisable to consult the vendors regarding what pressures the epoxy system may be subjected to.

1.6.6 Agglomeration of fillers

Agglomeration refers to the formation of groups of fillers, often visible to the naked eye. A thorough discussion with possible solutions are given by Shenoy [80, ch1.4.5]. Significant agglomeration was experienced when using Araldite 105-1 with Hardener HY 991 from Huntsman (Huntsman International LLC, Salt Lake City, USA). The composite mixed well; however, during degassing agglomeration occurred. No solution was obtained; however, it is believed that a planetary mixer with an inbuilt vacuum chamber may resolve this issue.

1.6.7 Crystallisation of epoxy resin

The crystallisation of epoxy resin refers to the phase change of the material from a liquid to a solid crystalline state [84]. If an epoxy resin has crystallised, the container with the epoxy can be placed in a $\sim$60 °C water bath until all of the crystals have melted. The crystallisation of the epoxy resin is a reversible process, hence crystallisation does not damage the resin.

1.6.8 Casting mould

It can be desirable to cast the epoxy in a mould to obtain the required physical dimensions. However, since the epoxy shrinks due to cross-linking, the thickness of the mould has to be thicker than the desired thickness. After curing, the sample has to be lapped down to the correct thickness. In Fig. 1.9, a schematic of a casting mould and production procedures are shown. The individual steps are explained in the figure caption.

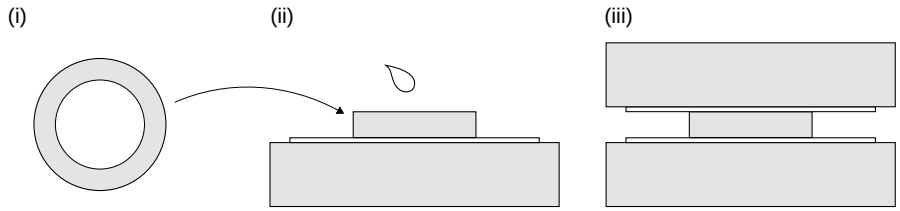

Figure 1.9: Schematic of the casting mould used for producing circular matching layers. (i) A circular mould is machined out of polyoxymethylene (POM). (ii) The mould is placed on a Mylar sheet placed on top of a flat POM block. The epoxy is carefully poured inside the mould. (iii) A second Mylar sheet is placed carefully over the mould and epoxy to avoid trapping air bubbles underneath the Mylar sheet. A second flat POM block is placed on top of the Mylar sheet. Pressure is applied on both top and bottom POM using clamps and the epoxy cures in an oven according to vendor instructions.

1.7 Summary of the thesis

This section contains a summary of the contributions included in the present thesis. The actual papers are enclosed at the end of the thesis.

Paper A: A Numerical Optimization Method for Transducer Transfer Functions by the Linearity of the Phase Spectrum

In paper A, we describe a new numerical optimisation method for conventional and more complex transducers, therein dual-frequency transducers. The method is based on linearising the phase spectrum of simulated transducer transfer functions. The linearisation is performed in a relevant frequency band and can be performed on multiple frequency bands simultaneously. The method was described in Sec. 1.4, and will not be repeated here.

One of the key characteristics of a linear phase optimised transducer is that the transfer function exhibits similarities to a Bessel filter. However, conventional analytical optimisation methods (e.g., DeSilets et al. [29]) results in a spectrum resembling a Butterworth filter. Because of this, we compared the results obtained with the linear phase method to that of a conventional analytical optimisation method [29]. From the comparison, it was shown that the linear phase optimised transducer exhibited a reduced time-sidelobe

level and pulse length compared to the conventional transducer; both of which are essential for imaging applications.

Paper A was published in IEEE Transactions on ultrasonics, ferroelectrics, and frequency control, vol. 66, no. 1, January 2019. In August 2019, the paper was selected as one of the IEEE TUFFC "Editor's Selection Of Articles." Before publication, we presented the main results at the 2017 IEEE International Ultrasonics Symposium (IUS) followed up by a conference proceeding, titled: "Numerical optimization of ultrasound transducers by the linearity of the phase spectrum."

Paper B: A Harmonic Dual-Frequency Transducer for Acoustic Cluster Therapy

In paper B, the design and testing of a harmonic dual-frequency transducer, as well as a laboratory setup, for pre-clinical in vivo studies of ACT on murine tumour models is described. The transducer utilises the inherent harmonics in a piezoceramic disk for the dual-frequency excitation. Specifically, the 5^{th} harmonic is used to evaporate the oil component and the fundamental is used to enhance the uptake of the co-administered drugs to the tumour (cf. Sec 1.1.4). Utilising the harmonics is unconventional; however, it resulted in a transducer with reduced complexity compared to the existing dual-frequency transducer solutions (cf. Fig. 1.4). The drawback of utilising the harmonics is that the harmonic pulses use several pulse cycles to reach steady-state conditions, i.e., they ring. To reduce the ringing of 5^{th} harmonic, the linear phase optimisation method was used to optimise both the fundamental and 5^{th} harmonic for transmission of sound. The optimisation of the transducer is described in Paper C.

A critical design feature was to sonicate the $\sim$6 mm tumours without having to move the transducer during testing. Since the distance to the geometrical focus and the beam-width scales with frequency and aperture size, two different aperture sizes were used. The high- and low-frequency beam-widths were 6 mm and 16 mm, respectively. Another challenge was how to couple the transducer to the tumours and to be sure that the beam centres were aligned with the tumours. The transducer couples to the tumours by use of a water path, realised by a water-proof 3-D printed ABS plastic tube filled with water, referred to as a water stand-off, and a water bag. The water bag rests on the animals and

the front of the water stand-off is placed in the water bag. Prior to testing, the transducer beam centres are marked on the water bag, and the tumours are aligned with the marks.

The laboratory set-up is comprised of a standard signal generator and power amplifier as well as an in-house built electrical switch-box that is used to tune out the electrical reactance of either sonication regime. In addition, in-house made and commercially available (Thorlabs Inc., Newton, USA) mounting accessories are used to hold and guide the water stand-off. In Fig. 1.10, two pictures and a schematic of the laboratory set-up used for the pre-clinical testing of ACT on tumours in mice are shown.

To verify the feasibility of using the 5^{th} harmonic to evaporate the oil droplet, several tests were made. First, the transducer's efficiency and output pressure were measured at the USN using the hydrophone set-up described in Sec. 1.5. After that, the transducer was taken to the Institute of Cancer Research, London, UK, where both *in vitro* and *in vivo* measurements on the resulting bubble population were performed. Both tests indicated that the dual-frequency transducer generated comparable bubble-size populations as commercial imaging systems. Based on these results, the dual-frequency transducer was considered suited for pre-clinical testing of ACT on tumours in mice.

In total, six transducers and laboratory set-ups were manufactured, which are currently in use at different research institutions around the world, and the result of one study has already been published [85]. The research institutions where the system is, or have been used, are

- Joint Department of Physics, Division of Radiotherapy and Imaging, Institute of Cancer Research, London, UK.
- Translational Genomics Research Institute, Phoenix, USA.
- Rikshospitalet, Oslo, Norway.
- Norwegian University of Science and Technology, Trondheim, Norway.
- INSERM, University of Tours, Tours, France.
- Faculty of Medicine and Health, University of Leeds, Leeds, UK.
- Institute of Translational Medicine, University of Liverpool, Liverpool, UK.

Paper B was published in Ultrasound in Medicine and Biology, Vol. 45, No. 9, pp. 2381-2390, 2019.

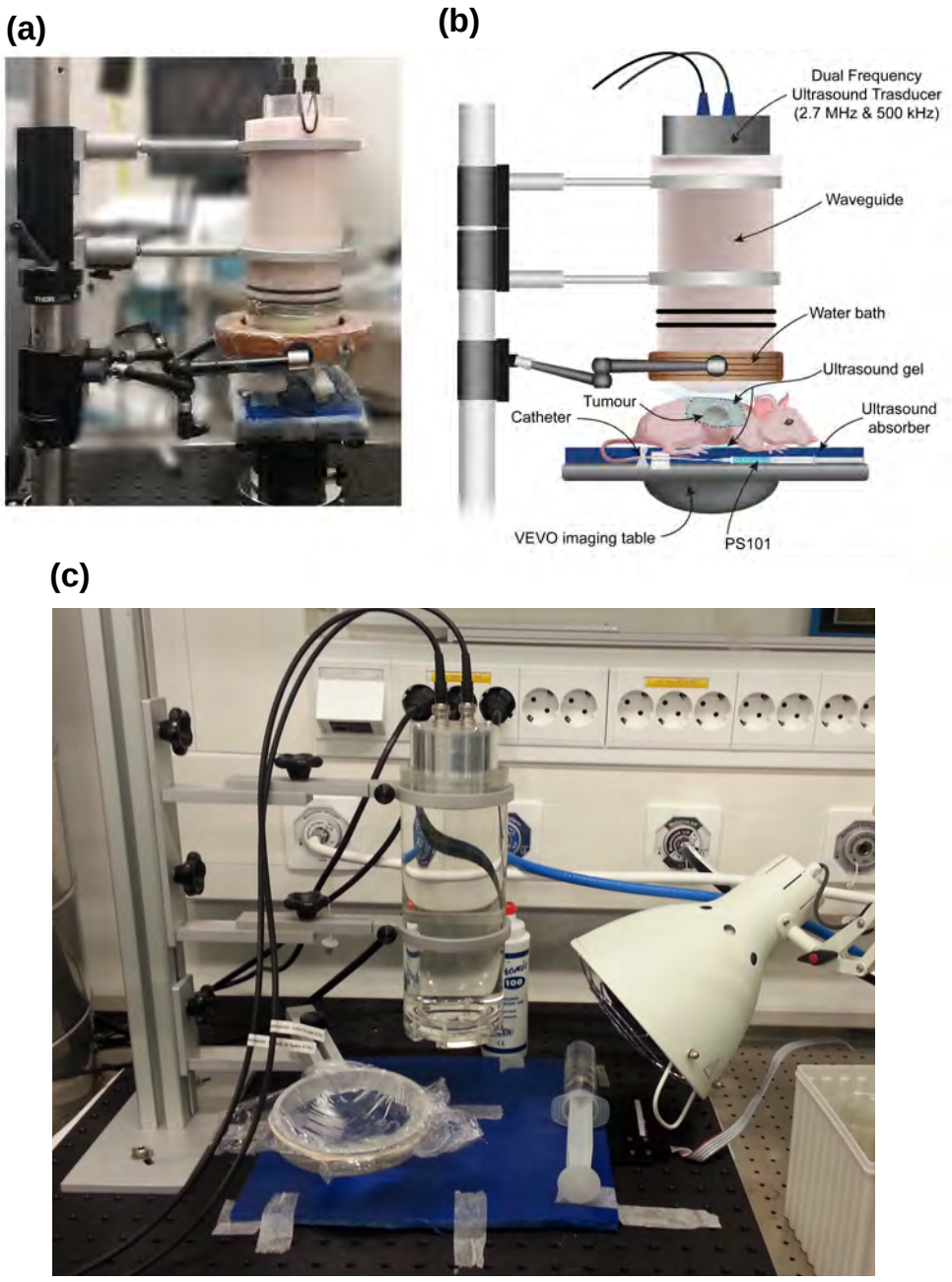

Figure 1.10: Two pictures (a,c) and a schematic (b) of the harmonic dual-frequency transducer and the laboratory set-up used for the pre-clinical testing of ACT on tumours in mice. Figure (a) and (b) are reproduced with permission from Phoenix Solutions AS [85]. Picture (a) is from the Translational Genomics Research Institute, Phoenix, USA. Picture (c) is taken by Melina Muhlenpfordt at the Norwegian University of Science and Technology, Trondheim, Norway.

Paper C: Design, Fabrication, and Testing of a Dual-Frequency Transducer for Acoustic Cluster Therapy Activation

In Paper C, the focus is on the optimisation method and acoustical characterisation of the transducer described in Paper B. Note that the transducer is identical to the one used in Paper B, hence the description of the transducer is omitted for brevity.

To optimise the transmission of sound at both the fundamental and the 5^{th} harmonic, an extension of the linear phase method, described in Paper A, was used (see also Sec. 1.4). In essence, the fundamental and 5^{th} harmonic phase spectra were simultaneously linearised by obtaining appropriate impedance and thickness values in the matching layers. Optimising both frequency bands for a linear phase results in comparable absolute bandwidths, however, significantly different relative bandwidths. Because of this, the 5^{th} harmonic pulse uses several pulse cycles to reach steady-state conditions. However, compared to a conventional analytical optimisation method [29], the impulse response of the 5^{th} harmonic was reduced with 50%.

Examples of the pulses are given in Paper B, and in Paper C the measured and simulated spectra are shown. The measurements and simulations exhibit good comparison, although some deviations are observed.

Paper C was published in the proceedings of the 2018 IEEE International Ultrasonics Symposium (IUS).

Paper D: A Dual-frequency Coupled Resonator Transducer

In Paper D, a dual-frequency coupled resonator transducer (CRT) is investigated. The CRT is comprised of two piezoceramic layers with a polymeric *coupling* layer sandwiched in between the piezoceramics. Depending on the electrical configuration, the CRT exhibits two usable frequency bands. A high-frequency band is achieved by using the front piezoceramic alone and a low-frequency band is achieved by exciting both piezoceramics together. Matching this transducer acoustically to the medium is, however, challenging. A conventional choice is to use $\lambda/4$ matching layers for the high-frequency band, and, effectively, much thinner layers for the low-frequency band. With this choice, because

of the low-impedance coupling layer, the high-frequency band performs comparably to conventional imaging transducers while the low-frequency band will exhibit a narrow bandwidth.

Because the CRT has not received much attention in the literature, an analytical approach was undertaken to shed light on the physical mechanisms responsible for the low-frequency band. Distributed, lumped, and mass-spring models describing the low-frequency band were developed, from which analytical expressions for the low-frequency resonance frequency were obtained. One analysis showed that the resonance frequency of the high-frequency band can be tailored to be 3-5 times higher than the resonance frequency of the low-frequency band by varying the stiffness of the polymeric layer.

A prototype dual-frequency CRT was designed, manufactured, and characterised acoustically. The prototype was intended for ACT, however, the design should also be applicable to certain combined imaging and therapy systems. The prototype was realised as a single-element transducer to best demonstrated the performance of the dual-frequency CRT. The high-frequency band exhibited a centre frequency of $2.5\,\mathrm{MHz}$, with a $-3\,\mathrm{dB}$ bandwidth of 70%. The low-frequency band exhibited a centre frequency of $0.5\,\mathrm{MHz}$, with a $-3\,\mathrm{dB}$ bandwidth of 13%. The high-frequency band is therefore suited for diagnostic imaging applications, or for manipulation of bubbles, and the low-frequency band is suited for transmission of longer pulses which can be used to induce biological effects in tissue, therein manipulation of microbubbles.

Paper D was submitted for publication to *IEEE Transactions on Ultrasonics, Ferroelectrics, and Frequency Control*, October 2019.

1.8 Thesis outline

The introductory chapter cements the motivation for the PhD project and it contains the key tools used throughout the course of the work to fulfil the research task at hand.

In addition to the introductory chapter, the thesis includes the full-length articles summarised in Sec. 1.7. The full-length articles may deviate slightly from the published articles

in that some are the accepted or submitted manuscripts; hence, publisher activities such as editing and proofreading are not included.

1.9 General discussion and future work

In Paper A, we described a new numerical optimisation method for conventional and more complex transducers, therein dual-frequency transducers. The optimisation method is based on linearising the phase spectrum of the electro-mechanical transfer function H. A linear optimised transducer exhibits an impulse response with very low time-sidelobe levels, ideal for imaging applications. Although the linear phase method results in ideal imaging pulses, modern imaging systems typically utilise 2nd harmonic imaging. Transducers suited for 2nd harmonic imaging should be optimised by other means than the linear phase methods.

In Paper B and C, a harmonic dual-frequency transducer for pre-clinical testing of ACT on tumours in mice was described. The 5th harmonic was used to evaporate the oil component and the fundamental was used to enhance the uptake of drugs to the target tissue. The harmonic dual-frequency transducer exhibited comparable evaporation levels compared to commercial imaging systems and was, therefore, a good choice for the pre-clinical studies. However, one of the drawbacks of utilising the harmonics was a narrow high-frequency band not suited for imaging applications. For both the pre-clinical and clinical studies, it could have been beneficial to perform imaging as well as to evaporate the oil component.

Because of this, in Paper D, we investigated a CRT with the potential for being used for both pre-clinical and clinical testing of ACT. The CRT's high-frequency band can be used to both evaporate the oil component, and for imaging. The prototype dual-frequency CRT, described in Paper D, was realised as a single-element transducer, and is readily available to be used for pre-clinical testing of ACT; however, clinical testing requires an array transducer for imaging. Moreover, an array transducer could also be beneficial for the pre-clinical studies, for example, to aid in aligning the tumours with the ultrasound beam centres.

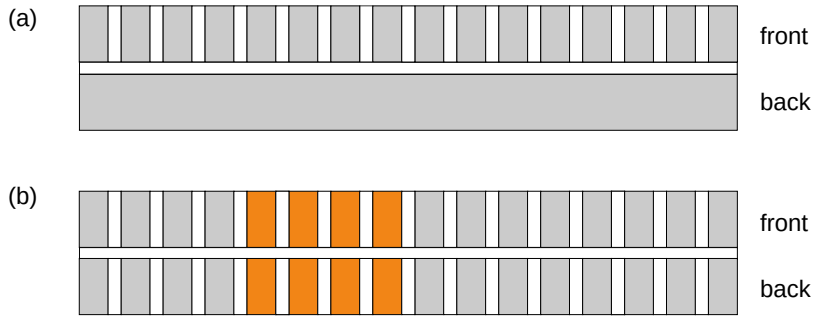

Figure 1.11: Schematics of possible designs for the dual-frequency CRT array. (a) Only the high-frequency band is used as an array. (b) Both the high- and low-frequency bands are used as arrays. The front and back array elements are obtained by dicing through the stack, mitigating possible alignment challenges. One low-frequency array element is indicated with a change in colour.

The CRT can be realised as a linear array, and different designs possibilities exist, for example

1. If the low-frequency sonication regime does not require beamforming, only the front high-frequency piezoceramic has to be an array. The front high-frequency array will perform similarly to a conventional array transducer with a low-impedance backing. Because of this, conventional design guidelines and beamforming techniques apply, cf. Fig. 1.11 (a).

2. If the low-frequency sonication regime requires beamforming, the two piezoceramics and coupling layer could be glued together prior to dicing. If the dicing blade can handle the thickness and alternating materials, this will mitigate any possibility of alignment challenges of the front and back array elements, cf. Fig. 1.11 (b).

In addition, transmit/receive electronics have to be incorporated as well as specific beamforming algorithms. For the pre-clinical testing, the MANUS ultrasound engine (Aurotech Ultrasound AS, Tydal, Norway) should be a good choice for the transmit/receive electronics because it is relatively cheap and portable.

In Paper D, we investigated the CRT as a dual-frequency transducer where the natural choice was to acoustically match the high-frequency band to the medium with $\lambda/4$

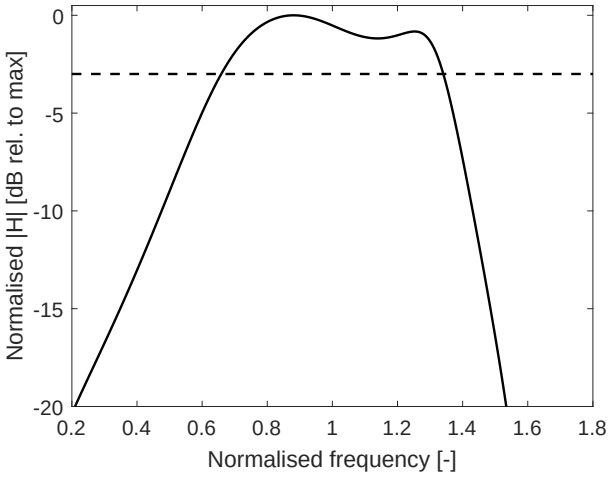

Figure 1.12: 1-D simulation of the magnitude of the electro-mechanical transfer function $|H|$ for a low-frequency CRT where the low-frequency band is matched to water using $\lambda/4$ impedance transformers. The magnitude is normalised to the maximum, and the frequency is normalised to the centre frequency. The horizontal dotted line indicates -3 dB from the maximum.

impedance transformers. However, the CRT's low-frequency band can also be matched to the medium with $\lambda/4$ impedance transformers. If low-frequency CRT is matched to the medium like this, the low-frequency band exhibit comparable performance as a single-layer piezoceramic. As an example of this, in Fig. 1.12, a 1-D simulation of $|H|$ for the CRT's low-frequency band is shown. The CRT was simulated using two Ferroperm™ Pz27's (identical piezoceramic as the transducer in Fig. 1.3) and a coupling layer of acoustic impedance 3.0 MRayl. Two matching layers were used, where the thickness of the layers were $\lambda/4$ calculated at the low-frequency. The bandwidth of the transducer in Fig. 1.12 is 70%, slightly higher compared to the transducer in Fig. 1.3 which exhibited a bandwidth of 63%.

Because of this, the low-frequency matched CRT could possibly be used in low-frequency underwater applications where it may be too expensive to use single-crystal materials. To the author's knowledge, no investigation of the low-frequency matched CRT has ever been performed.

1.10 Contributions

A list of contributions made during the time as a PhD. candidate is presented here.

Peer reviewed papers - Published

1. **Kenneth K. Andersen**, Martijn E. Frijlink, and Lars Hoff. A Numerical Optimization Method for Transducer Transfer Functions by the Linearity of the Phase Spectrum. *IEEE Transactions on Ultrasonics, Ferroelectrics, and Frequency Control*, 66(1):71–78, January 2019.

2. **Kenneth K. Andersen**, Andrew J. Healey, Nigel L. Bush, Martijn E. Frijlink, and Lars Hoff. A Harmonic Dual-Frequency Transducer for Acoustic Cluster Therapy. *Ultrasound in Medicine & Biology*, 45(9):2381–2390, 2019.

Peer reviewed papers - Submitted

1. **Kenneth K. Andersen**, Martijn E. Frijlink, Tonni F. Johannsen, and Lars Hoff. A Dual-frequency Coupled Resonator Transducer. Submitted for publication to *IEEE Transactions on Ultrasonics, Ferroelectrics, and Frequency Control*, October 2019.

Conference proceedings - Published

1. **Kenneth K. Andersen**, Martijn. E. Frijlink, and Lars Hoff. Numerical optimization of ultrasound transducers by the linearity of the phase spectrum. *In 2017 IEEE International Ultrasonics Symposium (IUS)*, pages 1–4, Washington, DC, September 2017.

2. Assel Ryspayeva, **Kenneth K. Andersen**, Lars Hoff, and Kristin Imenes. Design of an ultrasound transducer for continuous fetal heartbeat monitoring. *In 2017 IEEE International Ultrasonics Symposium (IUS)*, pages 1–4, Washington, DC, September 2017.

3. **Kenneth K. Andersen**, Andrew J. Healey, Nigel L. Bush, Martijn E. Frijlink, and Lars Hoff. Design, Fabrication, and Testing of a Dual-Frequency Transducer for Acoustic

Cluster Therapy Activation. *In 2018 IEEE International Ultrasonics Symposium (IUS)*, pages 1–4, Kobe, October 2018.

4. Ellen S. Røed, **Kenneth K. Andersen**, Martin Bring, Frank Tichy, Else-Marie Åsjord, and Lars Hoff. Acoustic Impedance Matching of PMN-PT/epoxy 1-3 Composites for Underwater Transducers with Usable Bandwidth Restricted by Electrical Power Factor. *In 2019 IEEE International Ultrasonics Symposium (IUS)*, pages 1–4, Glasgow, October 2019.

Conference presentations

1. 39th Scandinavian Symposium on Physical Acoustics. January 31 to February 3, 2016, Geilo, Norway. Oral presentation.
2. Ultrasound Transducer Workshop. September 16, 2016, Horten, Norway. Oral presentation.
3. 40th Scandinavian Symposium on Physical Acoustics. 29 January – 1 February, 2017, Geilo, Norway. Oral presentation.
4. CIUS Spring Conference. April 25-26, 2017, Trondheim, Norway. Oral presentation.
5. 2017 IEEE International Ultrasonics Symposium. September 6-9, 2017, Washington, D.C., USA. Poster presentation.
6. CIUS Spring Conference. April 24-25, 2018, Trondheim, Norway. Oral presentation.
7. 2017 IEEE International Ultrasonics Symposium. October 22-25, 2018, Kobe, Japan. Oral presentation.

Popular scientific presentations

1. USNTEK - Utforsk 2018. September 26, 2018, Horten, Norway. Oral presentation.
2. The collaboration with Phoenix Solutions was written about in *forskning.no*, an online newspaper with Norwegian and international research news.

https://forskning.no/kreft-medisin-og-helse-partner/ultralyd-kan-gi-mer-treffsikker-kreftbehandlng/1561383

Bibliography

[1] T. L. Szabo, *Diagnostic ultrasound imaging: Inside out*, 2nd ed. Elsevier Academic Press, 2014.

[2] T. S. Desser and R. Jeffrey, "Tissue harmonic imaging techniques: Physical principles and clinical applications," *Seminars in Ultrasound, CT and MRI*, vol. 22, no. 1, pp. 1–10, Feb. 2001.

[3] D. H. Evans, J. A. Jensen, and M. B. Nielsen, "Ultrasonic colour Doppler imaging," *Interface Focus*, vol. 1, no. 4, pp. 490–502, Aug. 2011.

[4] G. S. Reeder, P. J. Currie, D. J. Hagler, A. J. Tajik, and J. B. Seward, "Use of Doppler Techniques (Continuous-Wave, Pulsed-Wave, and Color Flow Imaging) in the Noninvasive Hemodynamic Assessment of Congenital Heart Disease," *Mayo Clinic Proceedings*, vol. 61, no. 9, pp. 725–744, Sep. 1986.

[5] W. D. O'Brien, "Assessing the Risks for Modern Diagnostic Ultrasound Imaging," *Japanese Journal of Applied Physics*, vol. 37, no. Part 1, No. 5B, pp. 2781–2788, May 1998.

[6] G. ter Haar, "Ultrasonic imaging: safety considerations," *Interface Focus*, vol. 1, no. 4, pp. 686–697, Aug. 2011.

[7] F. A. Duck, *Physical properties of tissue. A comprehensive reference book*, 1st ed. New York: Academic Press, 1990.

[8] NEMA UD 2-2004 (R2009), "Acoustic output measurement standard for diagnostic ultrasound equipment revision 3," National Electrical Manufacturers Association, Arlington, USA, 2004.

[9] IEC 60601-2-37:2007+AMD1:2015 CSV Consolidated version, "Medical electrical equipment - part 2-37: Particular requirements for the basic safety and essential performance of ultrasonic medicaldiagnostic and monitoring equipment," International Electrotechnical Commission, Geneva, Switzerland., Jul. 2015.

[10] T. R. Nelson, J. B. Fowlkes, J. S. Abramowicz, and C. C. Church, "Ultrasound Biosafety Considerations for the Practicing Sonographer and Sonologist," *Journal of Ultrasound in Medicine*, vol. 28, no. 2, pp. 139–150, 2009.

[11] V. J. Robertson and K. G. Baker, "A review of therapeutic ultrasound: effectiveness studies," *Physical Therapy*, vol. 81, no. 7, pp. 1339–1350, 2001.

[12] C. J. Diederich and K. Hynynen, "Ultrasound technology for hyperthermia," *Ultrasound in Medicine & Biology*, vol. 25, no. 6, pp. 871 – 887, 1999.

[13] H. J. Jang, J.-Y. Lee, D.-H. Lee, W.-H. Kim, and J. H. Hwang, "Current and Future Clinical Applications of High-Intensity Focused Ultrasound (HIFU) for Pancreatic Cancer," *Gut and Liver*, vol. 4, no. Suppl 1, pp. S57–S61, Sep. 2010.

[14] A. Maxwell, O. Sapozhnikov, M. Bailey, L. Crum, Z. Xu, B. Fowlkes, C. Cain, and V. Khokhlova, "Disintegration of Tissue Using High Intensity Focused Ultrasound: Two Approaches That Utilize Shock Waves," *Acoustics Today*, vol. 8, no. 4, p. 24, 2012.

[15] J. C. Simon, O. A. Sapozhnikov, V. A. Khokhlova, Y.-N. Wang, L. A. Crum, and M. R. Bailey, "Ultrasonic atomization of tissue and its role in tissue fractionation by high intensity focused ultrasound," *Physics in Medicine and Biology*, vol. 57, no. 23, pp. 8061–8078, Dec. 2012.

[16] F. A. Jolesz, "MRI-Guided Focused Ultrasound Surgery," *Annual Review of Medicine*, vol. 60, no. 1, pp. 417–430, Feb. 2009.

[17] O. Couture, J. Foley, N. F. Kassell, B. Larrat, and J.-F. Aubry, "Review of ultrasound mediated drug delivery for cancer treatment: updates from pre-clinical studies," *Translational Cancer Research*, vol. 3, no. 5, pp. 494–511–511, Oct. 2014.

[18] V. Paefgen, D. Doleschel, and F. Kiessling, "Evolution of contrast agents for ultrasound imaging and ultrasound-mediated drug delivery," *Frontiers in Pharmacology*, vol. 6, Sep. 2015.

[19] R. Myers, C. Coviello, P. Erbs, J. Foloppe, C. Rowe, J. Kwan, C. Crake, S. Finn, E. Jackson, J.-M. Balloul, C. Story, C. Coussios, and R. Carlisle, "Polymeric Cups

for Cavitation-mediated Delivery of Oncolytic Vaccinia Virus," *Molecular Therapy*, vol. 24, no. 9, pp. 1627–1633, Sep. 2016.

[20] C.-Y. Lin and W. G. Pitt, "Acoustic Droplet Vaporization in Biology and Medicine," *BioMed Research International*, vol. 2013, 2013.

[21] P. Sontum, S. Kvåle, A. J. Healey, R. Skurtveit, R. Watanabe, M. Matsumura, and J. Østensen, "Acoustic Cluster Therapy (ACT) – A novel concept for ultrasound mediated, targeted drug delivery," *International Journal of Pharmaceutics*, vol. 495, no. 2, pp. 1019–1027, Nov. 2015.

[22] A. J. Healey, P. C. Sontum, S. Kvåle, M. Eriksen, R. Bendiksen, A. Tornes, and J. Østensen, "Acoustic Cluster Therapy: In Vitro and Ex Vivo Measurement of Activated Bubble Size Distribution and Temporal Dynamics," *Ultrasound in Medicine & Biology*, vol. 42, no. 5, pp. 1145–1166, May 2016.

[23] Military Standard: MIL-STD-1376B, "Piezoelectric ceramic material and measurements guidelines for sonar transducers," Department of defence, USA, Feb. 1995.

[24] Z.-W. Yin, H.-S. Luo, P.-C. Wang, and G.-S. Xu, "Growth, characterization and properties of relaxor ferroelectric PMN-PT single crystals," *Ferroelectrics*, vol. 229, no. 1, pp. 207–216, May 1999.

[25] C.-H. Hong, H.-P. Kim, B.-Y. Choi, H.-S. Han, J. S. Son, C. W. Ahn, and W. Jo, "Lead-free piezoceramics – Where to move on?" *Journal of Materiomics*, vol. 2, no. 1, pp. 1–24, Mar. 2016.

[26] D. Wildes, W. Lee, B. Haider, S. Cogan, K. Sundaresan, D. M. Mills, C. Yetter, P. H. Hart, C. R. Haun, M. Concepcion, J. Kirkhorn, and M. Bitoun, "4-D ICE: A 2-D array transducer with integrated ASIC in a 10-fr catheter for real-time 3-D intracardiac echocardiography," *IEEE Transactions on Ultrasonics, Ferroelectrics, and Frequency Control*, vol. 63, no. 12, pp. 2159–2173, Dec 2016.

[27] H. Wang, T. Ritter, W. Cao, and K. K. Shung, "High frequency properties of passive materials for ultrasonic transducers," *IEEE Transactions on Ultrasonics, Ferroelectrics, and Frequency Control*, vol. 48, no. 1, pp. 78–84, Jan. 2001.

[28] G. Kossoff, "The Effects of Backing and Matching on the Performance of Piezoelectric Ceramic Transducers," *IEEE Transactions on Sonics and Ultrasonics*, vol. 13, no. 1, pp. 20–30, Mar. 1966.

[29] C. S. DeSilets, J. D. Fraser, and G. S. Kino, "The design of efficient broad-band piezoelectric transducers," *IEEE Transactions on Sonics and Ultrasonics*, vol. 25, no. 3, pp. 115–125, May 1978.

[30] J. Souquet, P. Defranould, and J. Desbois, "Design of Low-Loss Wide-Band Ultrasonic Transducers for Noninvasive Medical Application," *IEEE Transactions on Sonics and Ultrasonics*, vol. 26, no. 2, pp. 75–80, Mar. 1979.

[31] J. H. Goll, "The Design of Broad-Band Fluid-Loaded Ultrasonic Transducers," *IEEE Transactions on Sonics and Ultrasonics*, vol. 26, no. 6, pp. 385–393, Nov. 1979.

[32] A. R. Selfridge, R. Baer, B. T. Khuri-Yakub, and G. S. Kino, "Computer-Optimized Design of Quarter-Wave Acoustic Matching and Electrical Matching Networks for Acoustic Transducers," in *1981 Ultrasonics Symposium*, Oct. 1981, pp. 644–648.

[33] J. M. Thijssen, W. A. Verhoef, and M. J. Cloostermans, "Optimization of ultrasonic transducers," *Ultrasonics*, vol. 23, no. 1, pp. 41–46, 1985.

[34] T. L. Rhyne, "Computer optimization of transducer transfer functions using constraints on bandwidth, ripple, and loss," *IEEE Transactions on Ultrasonics, Ferroelectrics, and Frequency Control*, vol. 43, no. 6, pp. 1136–1149, Nov. 1996.

[35] G. Lockwood and F. Foster, "Modeling and optimization of high-frequency ultrasound transducers," *IEEE Transactions on Ultrasonics, Ferroelectrics, and Frequency Control*, vol. 41, no. 2, pp. 225–230, Mar. 1994.

[36] R. Desmare, L. P. Tran-Huu-Hue, F. Levassort, W. Wolny, and M. Lethiecq, "Modeling of multilayer piezoelectric structures," *Ferroelectrics*, vol. 224, no. 1, pp. 195–202, Mar. 1999.

[37] W. A. Smith, A. Shaulov, and B. A. Auld, "Tailoring the Properties of Composite Piezoelectric Materials for Medical Ultrasonic Transducers," in *IEEE 1985 Ultrasonics Symposium*, Oct. 1985, pp. 642–647.

[38] M. E. Frijlink, L. Løvstakken, and H. Torp, "Investigation of transmit and receive performance at the fundamental and third harmonic resonance frequency of a medical ultrasound transducer," *Ultrasonics*, vol. 49, no. 8, pp. 601–604, Dec. 2009.

[39] J. A. Hossack and B. A. Auld, "Improving the characteristics of a transducer using multiple piezoelectric layers," *IEEE Transactions on Ultrasonics, Ferroelectrics, and Frequency Control*, vol. 40, no. 2, pp. 131–139, Mar. 1993.

[40] S. Saitoh, M. Izumi, and Y. Mine, "A dual frequency ultrasonic probe for medical applications," *IEEE transactions on ultrasonics, ferroelectrics, and frequency control*, vol. 42, no. 2, pp. 294–300, 1995.

[41] S. de Fraguier, J. F. Gelly, L. Wolnerman, and O. Lannuzel, "A novel acoustic design for dual frequency transducers resulting in separate bandpass for color flow mapping (CFM)," in *Ultrasonics Symposium, 1990. Proceedings., IEEE 1990*, Dec. 1990, pp. 799–803 vol.2.

[42] T. Manh, L. Hoff, and T. F. Johansen, "Design and prototyping of dual layer linear arrays," in *2014 IEEE International Ultrasonics Symposium (IUS)*, 2014.

[43] D. J. Powell, G. Hayward, and R. Y. Ting, "Unidimensional modeling of multilayered piezoelectric transducer structures," *IEEE Transactions on Ultrasonics, Ferroelectrics, and Frequency Control*, vol. 45, no. 3, pp. 667–677, May 1998.

[44] P. D. Paco, O. Menendez, and E. Corrales, "Equivalent circuit modeling of coupled resonator filters," *IEEE Transactions on Ultrasonics, Ferroelectrics, and Frequency Control*, vol. 55, no. 9, pp. 2030–2037, Sep. 2008.

[45] Z. Wang, S. Li, T. J. Czernuszewicz, C. M. Gallippi, R. Liu, X. Geng, and X. Jiang, "Design, Fabrication, and Characterization of a Bifrequency Colinear Array," *IEEE Transactions on Ultrasonics, Ferroelectrics, and Frequency Control*, vol. 63, no. 2, pp. 266–274, Feb. 2016.

[46] T. Azuma, M. Ogihara, J. Kubota, A. Sasaki, S.-i. Umemura, and H. Furuhata, "Dual-frequency ultrasound imaging and therapeutic bilaminar array using frequency se-

lective isolation layer," *IEEE Transactions on Ultrasonics, Ferroelectrics and Frequency Control*, vol. 57, no. 5, pp. 1211–1224, May 2010.

[47] O. F. Myhre, T. F. Johansen, and B. A. Johan Angelsen, "Analysis of acoustic impedance matching in dual-band ultrasound transducers," *The Journal of the Acoustical Society of America*, vol. 141, no. 2, pp. 1170–1179, Feb. 2017.

[48] T. Azuma, S. Umemura, T. Kobayashi, M. Izumi, J. Kubota, A. Sasaki, and H. Furuhata, "Dual frequency array transducer for ultrasonic-enhanced transcranial thrombolysis," in *2003 IEEE Symposium on Ultrasonics*, vol. 1, Oct. 2003, pp. 680–683 Vol.1.

[49] J. Ma, K. H. Martin, P. A. Dayton, and X. Jiang, "A preliminary engineering design of intravascular dual-frequency transducers for contrast-enhanced acoustic angiography and molecular imaging," *IEEE Transactions on Ultrasonics, Ferroelectrics, and Frequency Control*, vol. 61, no. 5, pp. 870–880, May 2014.

[50] J. Ma, K. H. Martin, Y. Li, P. A. Dayton, K. K. Shung, Q. Zhou, and X. Jiang, "Design factors of intravascular dual frequency transducers for super-harmonic contrast imaging and acoustic angiography," *Physics in Medicine and Biology*, vol. 60, no. 9, pp. 3441–3457, Apr. 2015.

[51] Z. Wang, X. Jiang, T. J. Czernuszewicz, and C. M. Gallippi, "Dual-frequency IVUS transducer for acoustic radiation force impulse (ARFI) imaging," in *Ultrasonics Symposium (IUS), 2015 IEEE International*, Oct. 2015, pp. 1–4.

[52] B. D. Lindsey, J. Kim, P. A. Dayton, and X. Jiang, "Dual-Frequency Piezoelectric Endoscopic Transducer for Imaging Vascular Invasion in Pancreatic Cancer," *IEEE Transactions on Ultrasonics, Ferroelectrics, and Frequency Control*, vol. 64, no. 7, pp. 1078–1086, Jul. 2017.

[53] S. Li, J. Kim, Z. Wang, S. Kasoji, B. D. Lindsey, P. A. Dayton, and X. Jiang, "A Dual-Frequency Colinear Array for Acoustic Angiography in Prostate Cancer Evaluation," *IEEE Transactions on Ultrasonics, Ferroelectrics, and Frequency Control*, vol. 65, no. 12, pp. 2418–2428, Dec. 2018.

[54] S.-E. Måsøy, O. Standal, J. M. Deibele, S. P. Näsholm, B. Angelsen, T. F. Johansen, T. A. Tangen, and R. Hansen, "Nonlinear propagation acoustics of dual-frequency wideband excitation pulses in a focused ultrasound system," *The Journal of the Acoustical Society of America*, vol. 128, no. 5, pp. 2695–2703, Nov. 2010.

[55] A. Bouakaz, S. Frigstad, F. J. Ten Cate, and N. de Jong, "Super harmonic imaging: a new imaging technique for improved contrast detection," *Ultrasound in medicine & biology*, vol. 28, no. 1, pp. 59–68, 2002.

[56] D. N. Stephens, X. M. Lu, T. Proulx, W. Walters, P. Dayton, M. Tartis, D. E. Kruse, A. F. H. Lum, T. Kitano, S. M. Stieger, and K. Ferrara, "5a-1 Multi-frequency Array Development for Drug Delivery Therapies: Characterization and First Use of a Triple Row Ultrasound Probe," in *2006 IEEE Ultrasonics Symposium*, Oct. 2006, pp. 66–69.

[57] I. Akiyama, S. Saito, and A. Ohya, "Development of an ultra-broadband ultrasonic imaging system: prototype mechanical sector device," *Journal of Medical Ultrasonics*, vol. 33, no. 2, pp. 71–76, Jun. 2006.

[58] A. S. Savoia, B. Mauti, T. Manh, L. Hoff, F. Lanteri, J. Gelly, and T. Eggen, "Design, Fabrication and Characterization of a Hybrid Piezoelectric-CMUT Dual-Frequency Ultrasonic Transducer," in *2018 IEEE International Ultrasonics Symposium (IUS)*, Oct. 2018, pp. 1–4.

[59] T. Johansen and B. Angelsen, "Versatile analysis of multilayer piezoelectric transducers using an admittance matrix approach," in *Proceedings of the 28th Scandinavian Symposium on Physical Acoustics*, Jan. 2005.

[60] J. A. Jensen, "Field: A program for simulating ultrasound systems," in *10th Nord-Balt Conf on Biomed Imag, Vol. 4, Sup 1, Part 1*, 1996, pp. 351–353.

[61] J. A. Jensen and N. B. Svendsen, "Calculation of pressure fields from arbitrarily shaped, apodized, and excited ultrasound transducers," *IEEE Trans Ultrason Ferroelectr Freq Control*, vol. 39, no. 2, pp. 262–267, March 1992.

[62] W. P. Mason, *Electromechanical transducers and wave filters*. Princeton, NJ, Van Nostrand, 1948.

[63] R. Krimholtz, D. A. Leedom, and G. L. Matthaei, "New equivalent circuits for elementary piezoelectric transducers," *Electronics Letters*, vol. 6, no. 13, pp. 398–399, Jun. 1970.

[64] M. Redwood, "Transient Performance of a Piezoelectric Transducer," *The Journal of the Acoustical Society of America*, vol. 33, no. 4, p. 527, Jul. 2005.

[65] J. Kocbach, "Finite element modeling of ultrasonic piezoelectric transducers," Ph.D. dissertation, university of Bergen, PB 7800, 5020 Bergen, Norway, 2000.

[66] ANSI/IEEE Std 176-1987, "IEEE Standard on Piezoelectricity," The Institute of Electrical and Electronics Engineers, Inc., New York, USA, 1988.

[67] J. F. Nye, *Physical properties of crystals*, 2nd ed. Oxford University Press Inc., New York, 1985.

[68] S. Sherrit and K. B. Mukherjee, "Characterization of Piezoelectric Materials for Transducers."

[69] M. Wild, M. Bring, L. Hoff, and K. Hjelmervik, "Characterization of Piezoelectric Material Parameters Through a Global Optimization Algorithm," *IEEE Journal of Oceanic Engineering*, pp. 1–9, 2019.

[70] J. Wu, "Determination of velocity and attenuation of shear waves using ultrasonic spectroscopy," *The Journal of the Acoustical Society of America*, vol. 99, no. 5, pp. 2871–2875, May 1996.

[71] P. He, "Measurement of acoustic dispersion using both transmitted and reflected pulses," *The Journal of the Acoustical Society of America*, vol. 107, no. 2, pp. 801–807, 2000.

[72] C. H. Sherman and J. L. Butler, *Transducers and arrays for underwater sound*, 1st ed. Springer-Verlag New York, 2007.

[73] G. C. King, *Vibrations and waves*, 1st ed. John Wiley and Sons Ltd., 2009.

[74] S. C. Pohlig, "Signal duration and the Fourier transform," *Proceedings of the IEEE*, vol. 68, no. 5, pp. 629–630, May 1980.

[75] K. K. Andersen, A. J. Healey, N. L. Bush, M. E. Frijlink, and L. Hoff, "Design, Fabrication, and Testing of a Dual-Frequency Transducer for Acoustic Cluster Therapy Activation," in *2018 IEEE International Ultrasonics Symposium (IUS)*. Kobe: IEEE, Oct. 2018, pp. 1–4.

[76] A. S. Khimunin, "Numerical calculation of the diffraction corrections for the precise measurement of ultrasound absorption," *Acustica*, vol. 27, no. 4, pp. 173–181, 1972.

[77] P. H. Rogers and A. L. Van Buren, "An exact expression for the Lommel-diffraction correction integral," *the Journal of the Acoustical Society of America*, vol. 55, no. 4, pp. 724–728, 1974.

[78] K. Beissner, "Exact integral expression for the diffraction loss of a circular piston source," *Acustica*, vol. 49, pp. 212–217, 1981.

[79] L. E. Kinsler, A. R. Frey, A. B. Coppens, and J. V. Sanders, *Fundamentals of acoustics*, 4th ed. Wiley, 2000.

[80] A. V. Shenoy, *Rheology of Filled Polymer Systems*, 1st ed. Springer-Science+Business Media, B.V., 1991.

[81] E. A. Ashad, "Manufacturing and Characterization of acoustic matching layers for ultrasound transducers," Master's thesis, University of South-Easter Norway, Faculty of Technology, Natural Sciences and Maritime Sciences, Raveien 215, 3184 Borre, Norway, 2019.

[82] Q. Wu, Q.-Y. Chen, G.-X. Lian, and X.-M. Wang, "Air-coupled transducer with a hollow glass microspheres filled epoxy resin matching layer," in *2016 Symposium on Piezoelectricity, Acoustic Waves, and Device Applications (SPAWDA)*. Xi'an, China: IEEE, Oct. 2016, pp. 305–308.

[83] H. Zhao, Y. Liu, J. Wen, D. Yu, and X. Wen, "Dynamics and sound attenuation in viscoelastic polymer containing hollow glass microspheres," *Journal of Applied Physics*, vol. 101, no. 12, Jun. 2007.

[84] Epoxy Technology Inc., "Tech Tip 7: Epoxy crystallization," www.epotek.com, 2015.

[85] S. Ng, A. Healey, S. Kvåle, S. Kotopoulis, D. Hoff, P. Sontum, and H. Han, "Acoustic Cluster Therapy enhances the efficacy of chemotherapeutic regimens in patient-derived xenograft mouse models for pancreatic ductal adenocarcinoma," in *AACR-NCI-EORTC International Conference on Molecular Targets and Cancer Therapeutics*, Boston, Massachusetts, USA, Oct. 2019.

[86] D. M. Mills and S. W. Smith, "Multi-layered PZT/polymer composites to increase signal-to-noise ratio and resolution for medical ultrasound transducers," *IEEE Transactions on Ultrasonics, Ferroelectrics, and Frequency Control*, vol. 46, no. 4, pp. 961–971, Jul. 1999.

[87] K. K. Andersen, M. E. Frijlink, and L. Hoff, "A Numerical Optimization Method for Transducer Transfer Functions by the Linearity of the Phase Spectrum," *IEEE Transactions on Ultrasonics, Ferroelectrics, and Frequency Control*, vol. 66, no. 1, pp. 71–78, Jan. 2019.

A. Paper A

A Numerical Optimization Method for Transducer Transfer Functions by the Linearity of the Phase Spectrum

Kenneth K. Andersen[a], Martijn E. Frijlink [a], and Lars Hoff [a].

[a] Department of Microsystems, University of South-Eastern Norway, Horten, Norway.

A Numerical Optimization Method for Transducer Transfer Functions by the Linearity of the Phase Spectrum

Kenneth K. Andersen, *Student Member, IEEE,* Martijn E. Frijlink, *Member, IEEE,* and Lars Hoff, *Member, IEEE*

***Abstract*—New ultrasound imaging and therapeutic modalities may require transducer designs that are not readily facilitated by conventional design guidelines and analytical expressions. This motivates the investigation of numerical methods for complex transducer structures. Based on a mathematical theorem, we propose a new numerical design and optimization method for ultrasound transducers by linearizing the phase spectrum of transducer transfer functions. A gradient-based algorithm obtains the optimal transducer by varying a selected set of transducer parameters. To demonstrate the linear phase method, a simulated air-backed 4 MHz single element imaging transducer with two matching layers, bondlines, and electrodes is optimized by varying the impedances and thicknesses of the matching layers. The magnitude spectrum resembles that of a Gaussian and, compared to a conventional transducer, the time-sidelobe level is reduced by more than 15 dB. Moreover, we apply the linear phase method to analyze and compensate for bondlines that resonate within the passband. Lastly, we address the challenge of obtaining materials for the matching layers with the optimized impedance values by calculating alternative material pairs.**

***Index Terms*—Complex transducer design, numerical optimization method, transducer transfer functions, linear phase, short pulse duration.**

I. Introduction

ULTRASOUND imaging transducers typically consist of one active piezoceramic layer operating near its fundamental half- or quarter-wave resonance frequency. The piezoceramic has a relatively high characteristic impedance (∼30-35 MRayl) compared to the water-like medium of human tissue (∼1.5 MRayl). To effectively transfer the acoustic energy from the resonating piezoceramic layer to the tissue, one or several near quarter-wave impedance transformers are used. The impedance transformers are referred to as matching layers and are typically made of a passive polymeric material with or without inorganic fillers. The number of matching layers and choice of impedance in each layer has a significant effect on the transducer performance [1]. Another passive material can be attached to the back face of the transducer, referred to as backing, and has an impedance of ∼2-6 MRayl. The backing is used to increase the bandwidth and reduce both the pulse duration and time-sidelobe level of conventional broadband imaging transducers. A reduction in the pulse duration increases the spatial resolution, and a low time-sidelobe level relative to the main pulse is important to avoid image degradation [2, p. 122]. However, the inclusion of backing also reduces the sensitivity of the transducer unfavorably, and air-backed transducers are therefore an important class of transducers.

A realistic imaging transducer consists in addition of so-called construction layers (e.g., metal electrodes, flex-circuits, and bondlines) and electrical tuning networks, all of which may influence the performance of the transducer and affect the matching layers' impedance and thickness values. Moreover, the advance of new ultrasound imaging and therapeutic modalities can require more than one active piezoceramic layers to increase the signal-to-noise ratio [3], obtain dual-frequency excitation for nonlinear imaging [4], or facilitate the co-existence of imaging and therapy pulses in the same transducer [5].

The challenge of calculating appropriate values for the matching layers' impedances has received significant attention in the literature. Several analytical models have been suggested by, e.g., DeSilets *et al.* [6] (1978), Goll [7] (1979), and Souquet *et al.* [8] (1979). Common for the analytical models are the use of ideal quarter-wave matching layers, and the effect of the construction layers are typically not included in the models. To manage the complexity of new or realistic transducer designs, several numerical methods have been proposed. Selfridge *et al.* [9] (1981) defined a "badness" function that attempted to shorten the length while increasing the sensitivity of the impulse response; this was achieved by summing the energy after the fifth zero crossing and dividing by the square of the peak amplitude of the impulse response. The choice of the fifth zero crossing was empirical and subject to change depending on the actual transducer. A gradient method was used as the optimisation algorithm. Thijssen *et al.* [10] (1985) defined three performance characteristics to optimize imaging transducers, based on shortening the impulse response and maximizing the round-trip energy factor. The three performance characteristics were summed with weights, and the transducer parameters were changed systematically. Rhyne [11] (1996) presented a methodology for the computer-aided design of transducer transfer functions by characterizing the transducer as an all-pole filter. The optimization was achieved with a steepest decent algorithm over a -3 dB range, and only the magnitude spectrum was used. Furthermore, Lockwood and Foster [12] (1994) used the "badness" function of Selfridge *et al.* to optimize a transducer using network theory, and Desmare *et al.* [13] (2002) elaborated on the

This work was supported by the Research Council of Norway (grant number 237887).

K. K. Andersen, M. E. Frijlink and L. Hoff are with the Department of Microsystems, University of South-Eastern Norway, Horten, Norway (e-mail: kan@usn.no).

performance index by Thijssen *et al.* to optimize multilayer piezoelectric transducers.

The main objective of this paper is to propose a new numerical optimization method for ultrasound transducers based on a mathematical theorem: Pohlig [14] has shown that for a given spectral magnitude, the signal with the shortest duration must have a linear phase. Applied to ultrasound imaging transducers, this means that the shortest pulses are obtained if the transducer transfer functions are designed to have a linear phase in the relevant frequency band. We have published a preliminary study on the linear phase method [15] which, to our knowledge, is the first use of the phase spectra to optimize ultrasound transducers numerically.

In the current paper, we use the linear phase method to optimize a simulated air-backed 4 MHz single element imaging transducer with two matching layers, bondlines and electrodes. We compare the linear phase optimized transducer with a similar transducer where the matching layers' impedance values are optimized according to the established analytical equations derived by DeSilets *et al.*, referred to as a broadband transducer. The differences between these two transducers are discussed. In contrast to the broadband transducer, we show that the time-sidelobe level is at a minimum when the linear phase optimized transducer is air-backed. Moreover, we show an example of how the linear phase method may be used to analyze and compensate for bondlines that resonate within the passband. Finally, we show a linear relationship between the two matching layers' impedance values, allowing a transducer designer to choose from alternative materials.

II. Optimization method

A. Linearization of the phase spectrum

A typical spectrum of a simulated transducer transfer function $H(\omega) = U(\omega)/V(\omega)$ is shown in Fig. 1, where U is the complex normal particle velocity at the face of the transducer, V is the complex input voltage at the terminals of the transducer, $\omega = 2\pi f$ is the angular frequency, f is frequency, and $H = |H| \exp(i\theta)$, where $|H|$ denotes magnitude and θ is the spectral phase. The transducer's spectral phase, $\theta = \theta(\bar{x})$, is a function of all physical parameters that describes the transducer, where $\bar{x} = x_1, x_2, \ldots, x_j$ is a vector containing all the transducer parameters.

To quantify the linearity of the phase spectrum, a regression line is fitted to the spectral phase over a -3 dB frequency range about the center frequency, f_0,

$$\theta_l = \beta_0 + f\beta_1, \quad f \in [f_{min}, f_{max}], \tag{1}$$

where θ_l is referred to as an ideal linear phase, β_0 and β_1 are the coefficients of the regression line, and f_{min} and f_{max} are the lower and higher limits of the -3 dB frequency range, respectively. The -3 dB frequency range is referred to as *fitting range*, and the coefficients β_0 and β_1 are obtained from linear regression using Matlab (The MathWorks, Inc., Natick, Mass., USA).

The approach is to search the parameter space $\bar{x}$ that minimizes the difference between the ideal linear phase, θ_l, and the transducer phase, θ, mathematically expressed as

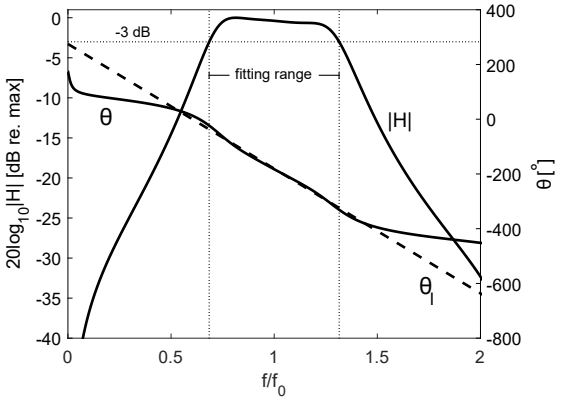

Fig. 1. A typical spectrum of a simulated transducer transfer function, H, where $|H|$ denotes magnitude (solid), θ is phase (solid), and θ_l is the ideal linear phase (dashed). The -3 dB fitting range is also indicated.

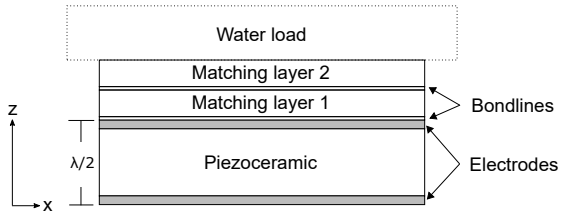

Fig. 2. Cross-sectional view of the transducer structure. The transducer consists of a $\lambda/2$ piezoceramic layer with 12 μm silver electrodes, two matching layers and 3 μm bondlines mechanically connecting the layers. The transducer is air-backed and radiates in water.

$$\arg\min_{\bar{x}} E(\bar{x}), \tag{2}$$

where $E(\bar{x})$ is referred to as the cost function to be minimized, and is defined as

$$E(\bar{x}) = \frac{1}{m}\sum_{i=1}^{m} |\theta(f_i, \bar{x}) - \theta_l(f_i, \bar{x})|, \quad f_i \in [f_{min}, f_{max}], \tag{3}$$

where $E = E(\bar{x})$ is the average absolute difference between the ideal linear phase $\theta_l(f_i, \bar{x})$ and the simulated transducer's spectral phase $\theta(f_i, \bar{x})$ summed over m discrete frequency points in the -3 dB fitting range. [1]

B. Simulation and optimization set-up

A schematic of the transducer is shown in Fig. 2. The transducer consists of a $\lambda/2$, 4 MHz piezoceramic layer with 12 μm silver electrodes, two matching layers and 3 μm bondlines mechanically connecting the layers. The transducer is air-backed and radiates in water. The material parameters for the Ferroperm^{TM} Pz27 (Meggitt Sensing Systems, Denmark)

[1] Note that a different cost function was used in [15]. Although we describe the two cost functions in a similar manner, the description in the current paper is correct.

TABLE I
SIMULATION PARAMETERS FOR THE ACTIVE AND PASSIVE MATERIALS.

Layer	h_{33} [GV/m]	$\epsilon_{33}^S/\epsilon_0$ [-]	Z [MRayl]	c [m/s]	Q [-]	l [μm]
Pz27 [a]	1.98	914	33.4	4330	74	470
ML 1	–	–	n/a	2250	50	n/a
ML 2	–	–	n/a	2250	30	n/a
Bondline	–	–	2.8	2450	13	3
Electrode	–	–	38.3	3650	30	12

[a] Provided by Meggitt Sensing Systems, Denmark.
ML = matching layer.
n/a = to be determined.

piezoceramic are provided by the manufacturer, and the remaining material parameters are realistic. The parameters are listed in Table I where h_{33} is the piezoelectric coefficient, $\epsilon_{33}^S/\epsilon_0$ is the relative dielectric constant, Z is the characteristic impedance, c is the speed of sound, Q is the quality-factor, and l is the thickness.

The transducer is simulated using a 1D equivalent circuit model proposed by Mason [16], implemented as an admittance matrix [17]. The transducer parameters being optimized are the characteristic impedance, Z_n, and the thickness, l_n, for each matching layer n, represented as two dimensionless ratios Z_n/Z_p and l_n/λ_n, where Z_p denotes the characteristic impedance in the piezoceramic, and λ_n denotes the wavelength in the n'th matching layer. In our case, this leads to four optimization parameters,

$$\left\{\frac{Z_1}{Z_p}, \frac{l_1}{\lambda_1}, \frac{Z_2}{Z_p}, \frac{l_2}{\lambda_2}\right\} \subset \bar{x}. \tag{4}$$

The optimization is achieved by varying the ratios Z_n/Z_p and l_n/λ_n and updating the transducer parameter vector, $\bar{x}$, with the new parameter values. The optimal transducer is obtained using a gradient-based algorithm implementation in MATLAB's *Global Optimization Toolbox*, and a schematic of the optimization process is shown in Fig. 3. The optimization process is initiated using a set of transducer parameter values, $\bar{x}$, either generated randomly or based on an established model, e.g., DeSilets *et al.*. Bounds on $\bar{x}$ may be applied to restrict the search. In the current work, the bounds on the impedance is $\pm 50\%$ of the impedance values obtained with the model of DeSilets *et al.*, and the thicknesses are allowed to vary from $\lambda/100$ to λ.

III. RESULTS

The results section is divided in two parts. The main optimization results are given in Sec. III-A, where the transducer in Fig. 2, including the bondlines and electrodes, has been optimized accordingly. In Sections III-B through III-D, we investigate the effect backing, bondlines, and alternative matching layer materials has on the transducer performance. To isolate these effects, the examples in Secs. III-B through III-D are presented with the bondlines and electrodes left out of the simulations, and the transducer is air-backed, unless otherwise stated.

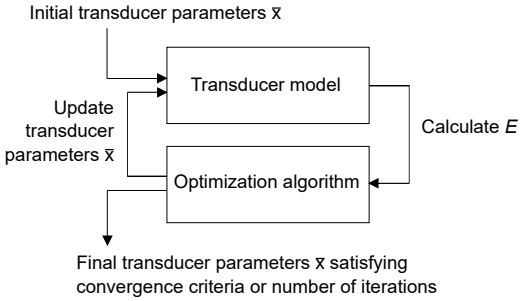

Fig. 3. Schematic of the optimization procedure. $\bar{x} = x_1, x_2, ...x_j$ are the physical transducer parameters and E is the cost function to be minimized. A 1D model is used to simulate the transducer, and a gradient-based algorithm implementation in MATLAB's *Global Optimization Toolbox*, is used to optimize the transducer.

A. Optimized air-backed transducer

The linear phase method was used to optimize the acoustic matching layers' impedances and thicknesses of the transducer in Fig. 2. The results are compared to a similar transducer, where the matching layers' impedances were optimized using the established analytical equations derived by DeSilets *et al.*, referred to as a broadband transducer.

The optimized impedance and thickness values are given in Table II, top section. The significant differences are in the characteristic impedance, where the linear phase optimized transducer, compared to the broadband transducer, exhibit 30% and 13% lower impedance values in matching layer one and two, respectively. In Table III, figures of merit are compared for the two transducers.

TABLE II
OPTIMIZATION RESULTS FOR THE LINEAR PHASE AND BROADBAND TRANSDUCERS.

		Linear phase		Broadband	
	Matching layer	Z [MRayl]	l/λ	Z [MRayl]	l/λ
With bondlines	1	6.21	0.25	8.83	0.242 [a]
and electrodes	2	2.04	0.256	2.34	0.25
Without bondlines	1	6.09	0.256	–	–
and electrodes	2	2.03	0.254	–	–

[a] Adjusted thickness to preserve a flat magnitude spectrum.

In Figure 4 (a–d), the spectrum, impulse response, group delay and envelope of the linear phase optimized transducer are compared to the broadband transducer. In Figure 4 (a), the magnitude spectra reveals the fundamental difference between the two approaches. The spectrum optimized with the linear phase method is rounded and resembles a Gaussian function whereas the broadband transducer's spectrum is nearly flat; the one-way -3 dB bandwidths are 43.1% and 63.2%, respectively. The phase spectra in Fig. 4 (a), show a close to linear variation with frequency over the fitting range; however, this may be deceiving. To distinguish the variations in the phase spectra, the group delays, $-\partial\theta/\partial\omega$, are shown in Fig. 4 (b), and are compared to the group delay of an ideal linear phase. The linear phase optimized transducer exhibits a close to constant group delay within the fitting range. To quantify this, we define

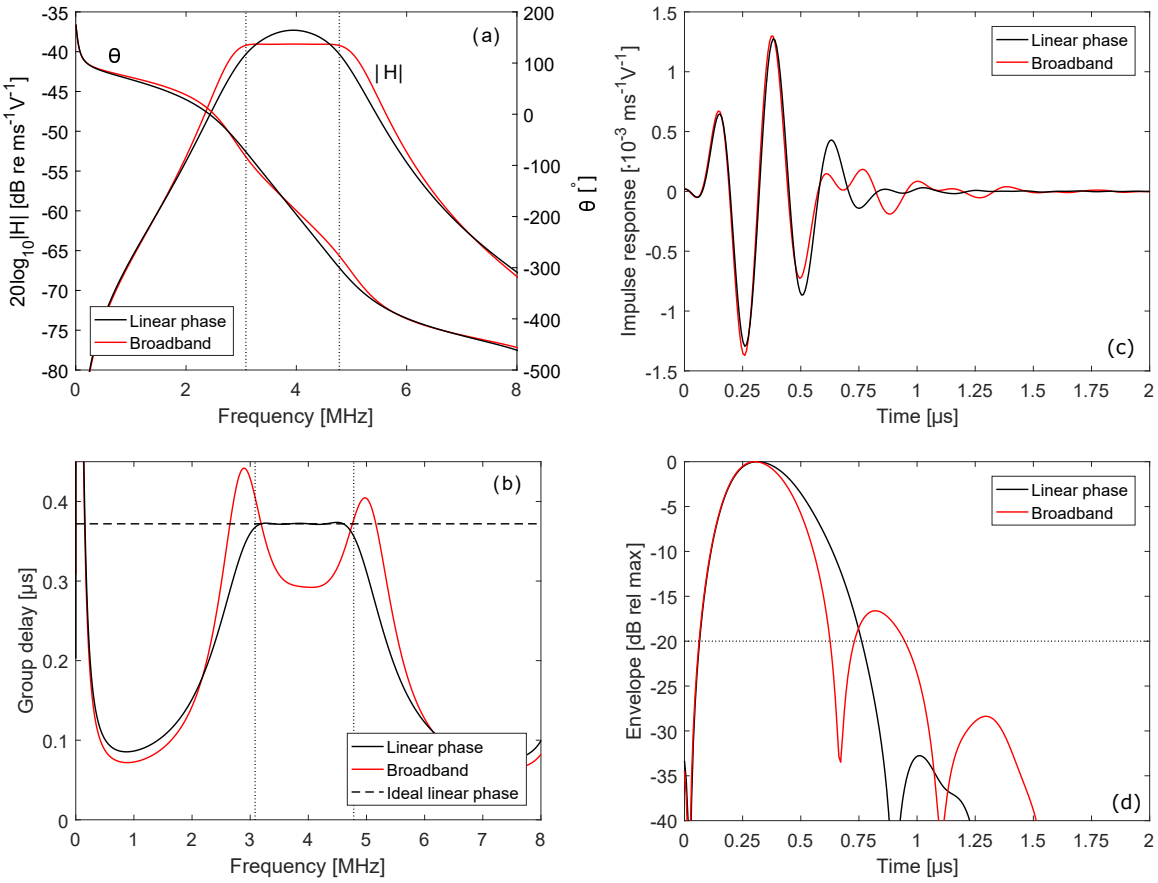

Fig. 4. Optimization results for the linear phase method (black) compared to the analytical equations derived by DeSilets *et al.* (red), referred to as a broadband transducer. (a) Magnitude, $|H|$, and phase, θ, of the transducer transfer function, H. (b) Group delay, $-\partial\theta/\partial\omega$, of the phases in (a) compared to the constant group delay of an ideal linear phase. (c) Impulse response. (d) Normalized magnitude of the analytic signal, denoted envelope, of the impulse responses in (c). The horizontal line marks the -20 dB level. Where applicable, the vertical lines indicate the -3 dB fitting range.

TABLE III
FIGURES OF MERIT FOR THE LINEAR PHASE AND BROADBAND TRANSDUCERS

Quantity	Linear phase	Broadband
-3 dB Bandwidth [%]	43.1	63.2
Group delay ripple [ns]	2.7	150
E [°]	0.022	3.8
Time-sidelobe maxima [dB]	-32.8	-16.6
One-way impulse response length [μs]		
-3 dB	0.30	0.26
-10 dB	0.52	0.44
-20 dB	0.70	0.88

the group delay ripple as the difference between the extrema within the -3 dB passband. For the linear phase optimized transducer and the broadband transducer, the group delay ripple is 2.7 ns and 150 ns, respectively. The large difference in the group delay ripple further highlights the fundamental difference between the two approaches. In Figure 4 (c), the impulse responses are shown, and up to approx. 0.5 μs, no significant differences between the two methods are observed. Beyond 0.5 μs, the impulse response corresponding to the linear phase optimized transducer exhibits less ringing at the expense of a wider main lobe. To illustrate and quantify this difference, the envelope of the two impulse responses is shown in Fig. 4 (d). The envelope is defined as the magnitude of the analytic signal, calculated from the Hilbert transform. The highest time-sidelobe level for the linear phase optimized transducer is -32.8 dB, while the broadband transducer has a time-sidelobe level at -16.6 dB.

B. Backing impedance

The current section investigates the effect of the backing impedance on the time-domain pulse. Specifically, we show that the time-sidelobe level for the linear phase optimized transducer of Fig. 2 is at a minimum when the transducer is air-backed.

In Figure 5 (a), the envelope of the impulse response for an air backed transducer is compared to a transducer with 10 MRayl backing. Both transducers are optimized for a linear phase. The transducer with 10 MRayl backing shows a reduction in the impulse length and, concurrently, an increased bandwidth (54%) compared to the air-backed transducer. However, no significant change in the time-sidelobe level is observed. In Figure 5 (b), we show the time-sidelobe

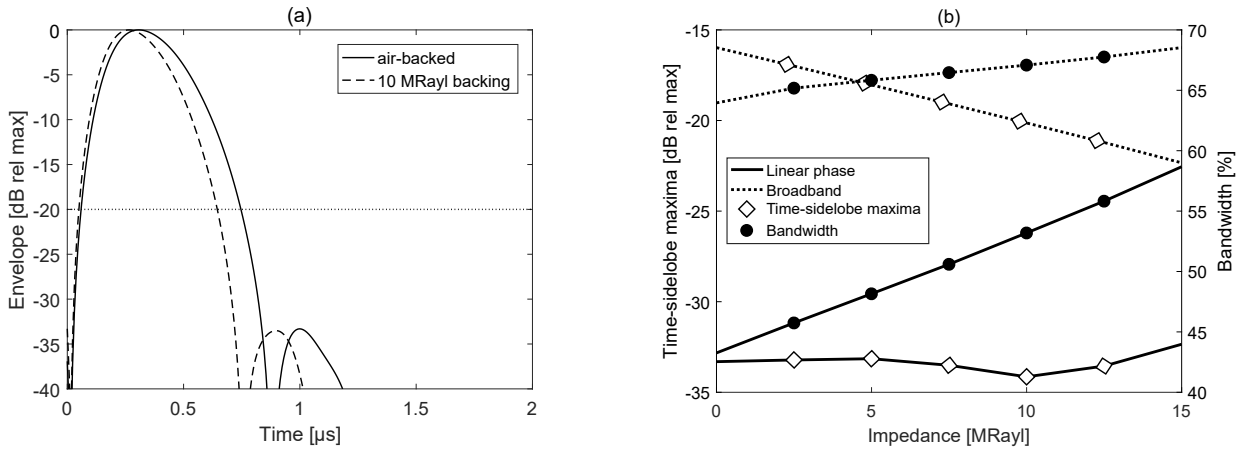

Fig. 5. (a) Envelope of the impulse response for an air-backed transducer (solid) compared to a transducer with 10 MRayl backing impedance (dashed), both optimized for a linear phase. (b) Time-sidelobe maxima and bandwidth as functions of increasing the backing impedance from 0 to 15 Mrayl for the linear phase optimized transducer compared to the broadband transducer.

maxima and bandwidth as functions of increasing the backing impedance from 0 to 15 MRayl, and we compare the results with those of the broadband transducer. For both transducers, a close to linear increase in the bandwidth for increasing backing impedance is observed. For the broadband transducer, a reduction in the time-sidelobe maxima is observed for increasing backing impedance. This is, however, not the case for the linear phase optimized transducer where a close to constant time-sidelobe maxima of -33 dB is observed. For the transducer in Fig. 2, a backing material may be used to obtain a wider bandwidth and a shorter pulse; however, no improvements in the time-sidelobe level is observed.

C. Compensation for epoxy bondlines

Epoxy glue is typically used for bonding together the various layers in a transducer. Unfortunately, even relatively thin bondlines may have a significant effect on the transducer performance [18]. In the current section, we show how the linear phase method can be applied to analyze and compensate for the effect of bondlines. The results in this section are specific for the transducer in Fig. 2, which is simulated using the material parameters listed in Table I. To isolate the effect of the bondlines, the transducer is simulated without electrodes.

In Figure 6, the magnitude of the transfer function, H, is shown for three transducers: (i) is optimized for a linear phase simulated without bondlines (cf. Table II, bottom section); (ii) is simulated with thicker, 10 μm ($\sim\lambda/50$), bondlines without changing the impedance and thickness values compared to (i); and (iii) is optimized for a linear phase with 10 μm bondlines included in the simulations. Transducer (ii) exhibits a large overall difference compared to (i) and (iii): the center frequency is 4.4 MHz, and a reduction in the bandwidth is also observed. The significance of the differences between transducer (i) and (iii) is, however, difficult to determine.

To elaborate on this, in Fig. 6 (b), we show the thickness relative to the wavelength and percentage change in impedance in both matching layers as functions of increasing the bondline thicknesses from 0 to 20 μm. Throughout, the thickness decreases and the impedance increases in both matching layers for increasing bondline thicknesses, and the most significant change is in matching layer one. Most importantly, for all bondline thicknesses, the cost function exhibits a close to constant value of 0.022°. This signifies that appropriate values for the matching layers' impedances and thicknesses has been obtained that preserves the linearity of the phase and, correspondingly, the magnitude of the transfer function.

D. Alternative materials

Purchasing or producing [19] passive materials for the matching layers with the exact optimized impedance values in Table II may be challenging. It is therefore of interest to investigate if other material pairs may be used and determine their trade-off.

To explore this, the impedance in matching layer two was fixed to a constant value and the remaining three design variables were optimized accordingly. The results are shown in Fig. 7 (a). A linear relationship between the impedance in matching layer one and two are observed, given a 2% variation in the thickness of matching layer two (not shown here). For impedance values different than the optimized minimum, the cost function, E, increases in value.

To determine the trade-off of using alternative material pairs, we choose to use Spurr's epoxy for the second matching layer. The impedance of Spurr's epoxy is 2.4 MRayl, 18% higher than the optimized minimum (2.03 MRayl). The impedance in the first matching layer is found from Fig. 7 (a) and is 7.8 MRayl, 28% higher than the optimized minimum (6.09 MRayl).

In Figure 7 (b), we show the magnitude of the transfer function, H, and the impulse response for the alternative materials, compared to the results in Fig. 4 (a,c). The bandwidth and time-sidelobe level for a transducer simulated with the alternative materials are 55% and -24.4, respectively. The bandwidth and time-sidelobe level are therefore higher than the ideal linear phase optimized transducer, but lower than the broadband transducer (cf. Table III). From this we

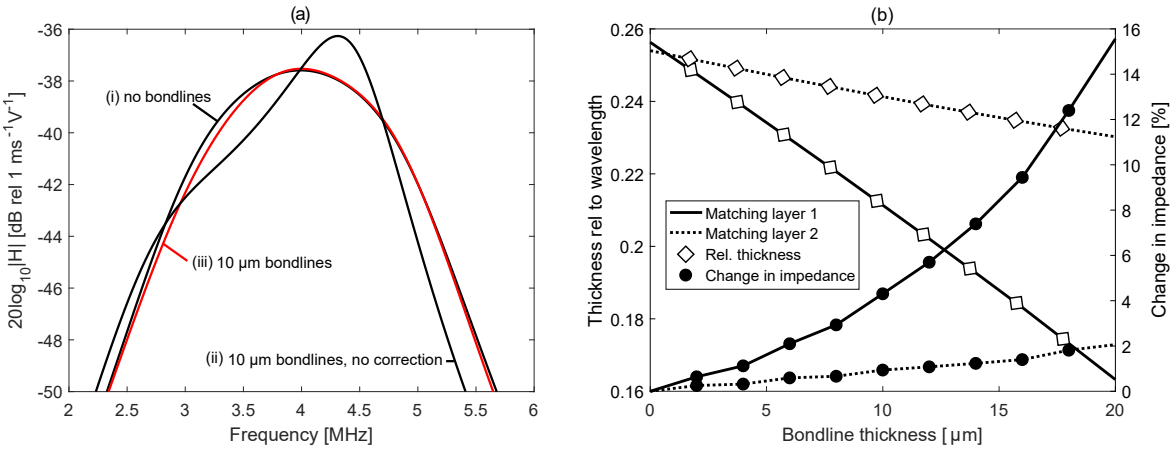

Fig. 6. (a) Three examples of the magnitude of the transfer function, H: (i) is optimized for a linear phase simulated without bondlines (cf. Table II, bottom section); (ii) 10 μm bondlines are included in the simulations without changing the impedance and thickness values compared to (i); (iii) is optimized for a linear phase with 10 μm bondlines included in the simulations. (b) Optimized matching layer thickness relative to wavelength and change in impedance as functions of increasing the bondline thickness from 0 to 20 μm.

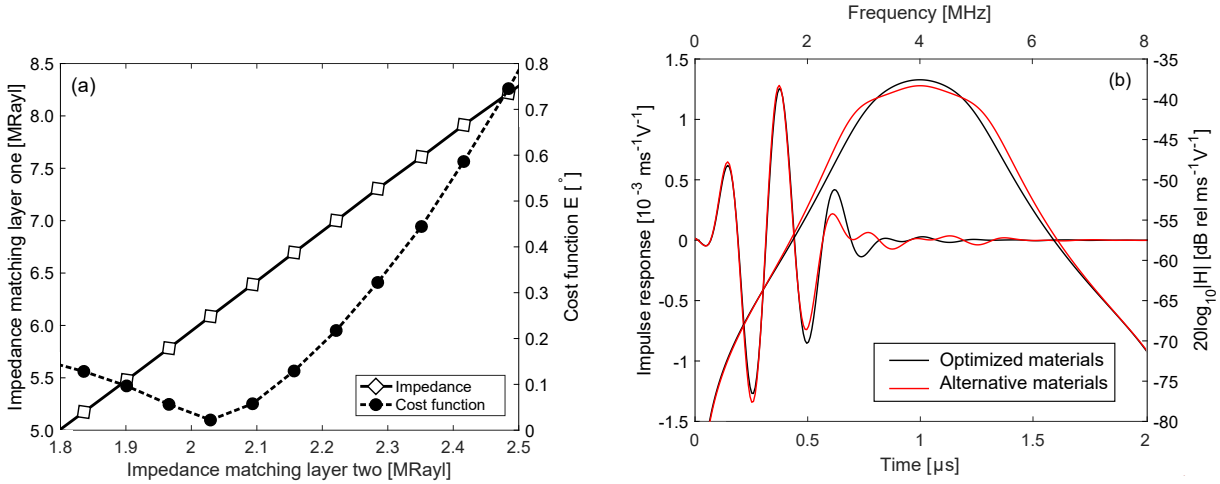

Fig. 7. (a) Optimized impedance in matching layer two and the cost function, E, as functions of increasing the impedance in matching layer one from 1.8 MRayl to 2.5 MRayl. (b) The magnitude of the transfer function, H, and the impulse response using alternative materials (red), compared to the optimized results in Fig. 4 (a,c) (black).

infer that materials with higher impedance, compared to the optimal, results in a transducer with a wider bandwidth at the expense of ripple in the passband. Moreover, alternative material pairs may be used with a negative or positive effect on the characteristics of the transducer. For example, if the pulse length is of most importance, a material pair with a higher impedance compared to Table II could be chosen.

IV. Discussion

Image resolution is the ability to distinguish between adjacent objects. The axial resolution of an ultrasound image is high when the spatial pulse length is short. The length of the pulse, and thus the axial resolution, is limited by the frequency and transducer bandwidth. The frequency is, however, limited by the penetration depth, and a large bandwidth does not, by itself, guarantee a short pulse. Ripple and sharp transitions at the band edges may lead to pulses with relatively high time-sidelobes, which may cause image degradation [2], e.g., in the form of cluttering and a reduction of the ultrasound image contrast. In the results section, we showed that optimizing the transducer in Fig. 2 for a linear phase compared to the broadband equations derived by DeSilets *et al.* resulted in a 14% reduction in the bandwidth; however, a 16 dB reduction in the time-sidelobe level and a 20% reduction in the pulse length was also observed. Compared to a broadband transducer, ultrasound images obtained with a linear phase optimized transducer has therefore the potential of being sharper and associated with less clutter stemming from the time-sidelobes. In certain applications, however, where a broadband transducer is required (e.g. second harmonic imaging, or when modulated excitation pulses are used), the method by DeSilets *et al.* may be preferred. Besides medical imaging transducers, the linear phase method can be used to optimize any transducer where a short pulse and low time-sidelobe level is required, e.g., in non-destructive testing.

Transducer design is often a trade-off between bandwidth

and sensitivity: A backing material may be used to widen the bandwidth and lower the time-sidelobe level on the expense of a reduction in the sensitivity. In the current work, we have shown that the linear phase optimized transducer has a constant time-sidelobe maxima of -33 dB for backing impedances in the range 0 to 15 MRayl. A linear phase optimized transducer should, therefore, be air-backed in-order to maintain the sensitivity at its maximum. Note, however, that the spatial pulse length must be sufficiently short; hence, the bandwidth must be wide enough, to obtain the axial resolution required for the application in mind. In some cases, a backing material may be required to obtain the necessary bandwidth.

Generally, the backing impedance could be included as an optimization parameter; however, if this is performed on the current transducer the optimization algorithm do not obtain the global minimum. The reason for this is that the variations in the cost function, E, with increasing backing impedance are small, and the optimization algorithm converges to a local minimum. If backing is included as an optimization parameter, we advise using a similar method as described in Sec. III-B to verify the results.

In the current paper, the cost function, E, was calculated over a floating -3 dB fitting range; however, other fitting ranges may be used. The benefit of a -3 dB range is that no a priori knowledge about the performance of the transducer is needed. However, transducers with -3 dB bandwidths below, e.g., 10% may be obtained if the variable space permits it. If such transducers are obtained, the bounds on the optimization parameters should be reduced, or a fixed fitting range should be considered [15].

Compared to the analytical design and optimization methods [6]–[8], the linear phase method manages the complexity of realistic and complex transducer structures. The linear phase method yields comparable transfer functions and impulse responses as the existing numerical methods [9]–[11]; however, in contrast to [9] and [10], the linear phase method is based on a mathematical theorem.

In the current paper, the transducer was simulated using a 1D equivalent circuit model proposed by Mason [16]. The Mason model is well established for piezoelectric transducer structures oscillating in thickness mode; however, if other oscillation modes are present, other models should be considered, e.g., finite element method (FEM). 1D simulations are considerably faster compared to 2D- or 3D-FEM simulations, and, for this reason, lend themselves better to be used together with numerical optimization methods due to the extensive use of simulations. 1D simulations can also be used to design arrays and composite transducers if appropriate kerf and ceramic sizes are used [20], [21]. If it is necessary to use 2D- or 3D-FEM simulations to obtain accurate estimates of the transducer's resonating behaviour, we suggest that an initial optimization is performed using 1D simulations. The bounds on the optimization parameters for the 2D- or 3D-FEM optimizations may therefore be made significantly smaller using the results from the 1D optimization, and a reduction in the total optimization time is thus expected.

V. Conclusion

A new numerical design and optimization method for ultrasound transducers has been developed. The method is based on a mathematical theorem and linearizes the phase spectrum of transducer transfer functions. The motivation for a linearized phase spectrum is to obtain short pulses, ideal for imaging applications. Simulations of an air-backed single element 4 MHz imaging transducer with electrodes and bondlines demonstrated an implementation of the linear phase method. The magnitude spectrum resembled that of a Gaussian and, compared to a conventional broadband imaging transducer, the time-sidelobe level was reduced by more than 15 dB. Moreover, a close to constant group delay ripple was obtained.

The linear phase method is developed to be used on complex transducer structures designed for new imaging and therapeutic modalities. For example, the linear phase method can be used to optimize transducers where several active piezoceramic layers are used. However, the linear phase method can also be a valuable tool for conventional imaging transducers. Specifically, it manages the inclusion of construction layers (electrodes, flex-circuits and bondlines) and electrical loading in the design and optimization process, which is not trivial using the existing analytical methods.

Acknowledgment

The authors express their gratitude to Kristoffer Johansen and Marcus Wild for proofreading the manuscript.

References

[1] G. Kossoff. The Effects of Backing and Matching on the Performance of Piezoelectric Ceramic Transducers. *IEEE Transactions on Sonics and Ultrasonics*, 13(1):20–30, March 1966.

[2] T. L. Szabo. *Diagnostic ultrasound imaging: Inside out*. Elsevier Academic Press, 1 edition, 2004.

[3] D. M. Mills and S. W. Smith. Multi-layered PZT/polymer composites to increase signal-to-noise ratio and resolution for medical ultrasound transducers. *IEEE Transactions on Ultrasonics, Ferroelectrics, and Frequency Control*, 46(4):961–971, 1999.

[4] N. R. Owen and F. P. Curra. Multilayer transducer for nonlinear imaging with application to targeting and monitoring of therapeutic ultrasound. In *2010 IEEE International Ultrasonics Symposium*, pages 893–896, October 2010.

[5] T. Azuma, M. Ogihara, J. Kubota, A. Sasaki, S.i. Umemura, and H. Furuhata. Dual-frequency ultrasound imaging and therapeutic bilaminar array using frequency selective isolation layer. *IEEE Transactions on Ultrasonics, Ferroelectrics and Frequency Control*, 57(5):1211–1224, May 2010.

[6] C. S. DeSilets, J. D. Fraser, and G. S. Kino. The design of efficient broad-band piezoelectric transducers. *IEEE Transactions on Sonics and Ultrasonics*, 25(3):115–125, May 1978.

[7] J. H. Goll. The Design of Broad-Band Fluid-Loaded Ultrasonic Transducers. *IEEE Transactions on Sonics and Ultrasonics*, 26(6):385–393, November 1979.

[8] J. Souquet, P. Defranould, and J. Desbois. Design of Low-Loss Wide-Band Ultrasonic Transducers for Noninvasive Medical Application. *IEEE Transactions on Sonics and Ultrasonics*, 26(2):75–80, March 1979.

[9] A. R. Selfridge, R. Baer, B. T. Khuri-Yakub, and G. S. Kino. Computer-Optimized Design of Quarter-Wave Acoustic Matching and Electrical Matching Networks for Acoustic Transducers. In *1981 Ultrasonics Symposium*, pages 644–648, October 1981.

[10] J. M. Thijssen, W. A. Verhoef, and M. J. Cloostermans. Optimization of ultrasonic transducers. *Ultrasonics*, 23(1):41–46, 1985.

[11] T. L. Rhyne. Computer optimization of transducer transfer functions using constraints on bandwidth, ripple, and loss. *IEEE Transactions on Ultrasonics, Ferroelectrics, and Frequency Control*, 43(6):1136–1149, November 1996.

[12] G.R. Lockwood and F.S. Foster. Modeling and optimization of high-frequency ultrasound transducers. *IEEE Transactions on Ultrasonics, Ferroelectrics, and Frequency Control*, 41(2):225–230, March 1994.

[13] R. Desmare, L.P Tran-Huu-Hue, F. Levassort, and M. Lethiecq. Practical Design of Multilayer Piezoelectric Transducers for Harmonic Imaging. In Michael Halliwell and Peter N. T. Wells, editors, *Acoustical Imaging*, pages 117–122. Springer US, Boston, MA, 2002.

[14] S. C. Pohlig. Signal duration and the Fourier transform. *Proceedings of the IEEE*, 68(5):629–630, May 1980.

[15] K. K. Andersen, M. Frijlink, and L. Hoff. Numerical optimization of ultrasound transducers by the linearity of the phase spectrum. In *2017 IEEE International Ultrasonics Symposium (IUS)*, pages 1–4, 2017.

[16] W. P. Mason. *Electromechanical transducers and wave filters*. Princeton, NJ, Van Nostrand, 1948.

[17] T.F. Johansen and B.A.J. Angelsen. Versatile analysis of multilayer piezoelectric transducers using an admittance matrix approach. In *Proceedings of the 28th Scandinavian Symposium on Physical Acoustics*, January 2005.

[18] E. K. Sittig. Effects of bonding and electrode layers on the transmission parameters of piezoelectric transducers used in ultrasonic digital delay lines. *IEEE Transactions on Sonics and Ultrasonics*, 16(1):2–9, 1969.

[19] H. Wang, T. Ritter, W. Cao, and K. K. Shung. High frequency properties of passive materials for ultrasonic transducers. *IEEE Transactions on Ultrasonics, Ferroelectrics, and Frequency Control*, 48(1):78–84, January 2001.

[20] T. A. Ritter, T. R. Shrout, R. Tutwiler, and K. K. Shung. A 30-MHz piezo-composite ultrasound array for medical imaging applications. *IEEE Transactions on Ultrasonics, Ferroelectrics, and Frequency Control*, 49(2):217–230, February 2002.

[21] W. A. Smith and B. A. Auld. Modeling 1-3 composite piezoelectrics: thickness-mode oscillations. *IEEE Transactions on Ultrasonics, Ferroelectrics, and Frequency Control*, 38(1):40–47, January 1991.

B. Paper B

A Harmonic Dual-Frequency Transducer for Acoustic Cluster Therapy

Kenneth K. Andersen [a], Andrew J. Healey [b] Nigel L. Bush [c]

Martijn E. Frijlink [a], and Lars Hoff [a].

[a] Department of Microsystems, University of South-Eastern Norway, Horten, Norway.

[b] Phoenix Solutions AS, PO Box 4741, N-0421 Oslo, Norway.

[c] Joint Department of Physics, Division of Radiotherapy and Imaging, the Institute of Cancer Research, London, UK.

Published in Ultrasound in Medicine and Biology, Vol. 45, No. 9, pp. 2381-2390, 2019.

Ultrasound in Med. & Biol., Vol. 45, No. 9, pp. 2381–2390, 2019

0301-5629/$ - see front matter

https://doi.org/10.1016/j.ultrasmedbio.2019.04.008

● *Original Contribution*

A HARMONIC DUAL-FREQUENCY TRANSDUCER FOR ACOUSTIC CLUSTER THERAPY

KENNETH K. ANDERSEN,* ANDREW HEALEY,† NIGEL L. BUSH,‡ MARTIJN E. FRIJLINK,* and LARS HOFF*

* University of South-Eastern Norway, Horten, Norway; † Phoenix Solutions AS, Oslo, Norway; and ‡ Joint Department of Physics, Division of Radiotherapy and Imaging, The Institute of Cancer Research, London, UK

(*Received* 24 *November* 2018; *revised* 22 *March* 2019; *in final from* 7 *April* 2019)

Abstract—Acoustic Cluster Therapy (ACT) is a two-component formulation of commercially available microbubbles (Sonazoid; GE Healthcare, Oslo, Norway) and microdroplets (perfluorated oil) currently under development for cancer treatment. The microbubbles and microdroplets have opposite surface charges to form microbubble/microdroplet clusters, which are administered to patients together with a drug. When the clusters and drug reach the target tumour, two ultrasound (US) exposure regimes are used: First, high-frequency (>2.0 MHz) US evaporates the oil and forms ACT bubbles that lodge at the microvascular level. Second, low-frequency (0.5 MHz) US induces stable mechanical oscillations of the ACT bubbles, causing localized micro-streaming, radiation and shear forces that increase the uptake of the drugs to the target tumour. This report describes the design and testing of a dual-frequency transducer and a laboratory setup for pre-clinical *in vivo* studies of ACT on murine tumour models. The dual-frequency transducer utilizes the 5th harmonic (2.7 MHz) and fundamental (0.5 MHz) of a single piezoceramic disk for the high-frequency and low-frequency regimes, respectively. Two different aperture radii are used to align the high-frequency and low-frequency beam maxima, and the high-frequency −3 dB beam width diameter is 6 mm, corresponding to the largest tumour sizes we expect to treat. The low-frequency −3 dB beam width extends 6 mm. Although unconventional, the 5th harmonic exhibit a 44% efficiency and can therefore be used for transmission of acoustic energy. Moreover, both *in vitro* and *in vivo* measurements demonstrate that the 5th harmonic can be used to evaporate the microbubble/microdroplet clusters. For the *in vivo* measurements, we used the kidneys of non-tumour–bearing mice as tumour surrogates. Based on this, the transducer is deemed suited for pre-clinical *in vivo* studies of ACT and replaces a cumbersome test setup consisting of two transducers. (E-mail: kan@usn.no)

Key words: **Dual-frequency transducer design, Acoustic Cluster Therapy, Numerical optimization, Linear phase, Harmonic excitation.**

INTRODUCTION

Dose-limiting toxicity hampers the efficacy of a wide range of drugs, particularly in oncology when administered systematically. Often therapeutic regimes must be terminated because of unwanted side effects rather than successful treatment of the condition. Throughout the past decades, the pharmaceutical industry has invested significant resources in trying to overcome this quandary. One approach is to use ultrasound (US) energy in combination with acoustically active particles. Commercially available microbubble US contrast agents have been used, such as Optison, Sonazoid and SonoVue (GE Healthcare, Oslo, Norway), and several other technologies are being pursued, such as acoustic droplet vaporisation ([ADV] Lin and Pitt 2013), polymeric cups (Myers et al. 2016) and various drug-loaded particles (Li et al. 2017), among others.

Acoustic Cluster Therapy (ACT) is in the ADV class. The ACT product is the compound formed by reconstitution of commercially available, negatively charged microbubbles (Sonazoid) with an emulsion of positively charged microdroplets of an inert, perfluorated oil. The active moiety comprises free-flowing, microbubble/microdroplet clusters formed by electrostatic attraction (Sontum et al. 2015).

A therapeutic treatment with ACT requires the administration of the microbubble/microdroplet clusters together with a drug (*e.g.*, chemotherapeutic) and two US exposure regimes: The first US exposure regime utilizes

Address correspondence to: Kenneth K. Andersen, Raveien 223 B, H0209, 3184 Borre, Norway. E-mail: kan@usn.no

low-intensity (mechanical index [MI] ~0.35) pulses with a centre frequency above 2.0 MHz (Healey et al. 2016). On exposure, the microbubble components act as evaporation seeds and transfers energy to the oil droplets, resulting in vaporisation of the oil and the formation of the larger, gaseous ACT bubbles (Fig. 1). The resulting bubble population produced has a mean diameter *in vivo* of 22 μm, with no bubbles larger than 44 μm (Healey et al. 2016). The size range has been engineered so that the ACT bubbles lodge in the microvasculature and remain for 5−10 min, during which the second US exposure regime is employed. The second US exposure is used to increase the therapeutic efficacy of the co-administered drugs. Low-intensity (MI ~0.2) pulses with a centre frequency of 0.5 MHz, closer to the resonance frequency of the gaseous ACT bubbles, are used. The second US exposure induces mechanical oscillations of the ACT bubbles, producing stable oscillation, localised microstreaming, radiation and shear forces that increase the local permeability of the vasculature, increasing transport of the co-administered drug across the capillary barrier and through the extracellular matrix (Sontum et al. 2015; Fig. 1a).

Throughout this report, we will refer to the first US exposure as activation, or high-frequency (HF), and the second exposure as therapy, or low-frequency (LF).

Proof of mechanism (Sontum et al. 2015) and proof of principle (Van Wamel et al. 2016) results have been published, including several successful therapy studies spanning several drug types (Åslund et al. 2017; Kotopoulis et al. 2017; Van Wamel et al. 2016). In the studies, however, two separate transducer systems were used for the HF ACT activation and LF therapy. Careful setup is required to accurately align the HF and LF acoustic fields to insonate the tumour volume adequately. The challenges with a two-transducer setup are accentuated because of the small size of the animals and tumours and the different insonication directions required with two transducers. In addition, it is especially desirable to localise the fields as much as possible to the tumour volume to reduce exposure (and therapy response) of surrounding normal, healthy tissue. Replacement with a single dual-frequency transducer with overlapping HF and LF fields may thus assist and simplify laboratory setup and workflow procedures and help mitigate human errors.

A dual-frequency transducer accommodates two US frequency bands in the same transducer, typically with an HF-to-LF ratio equal to or greater than 2:1. Various dual-frequency transducer designs have been suggested in the literature where both a HF and LF piezoceramic layer are incorporated in the same

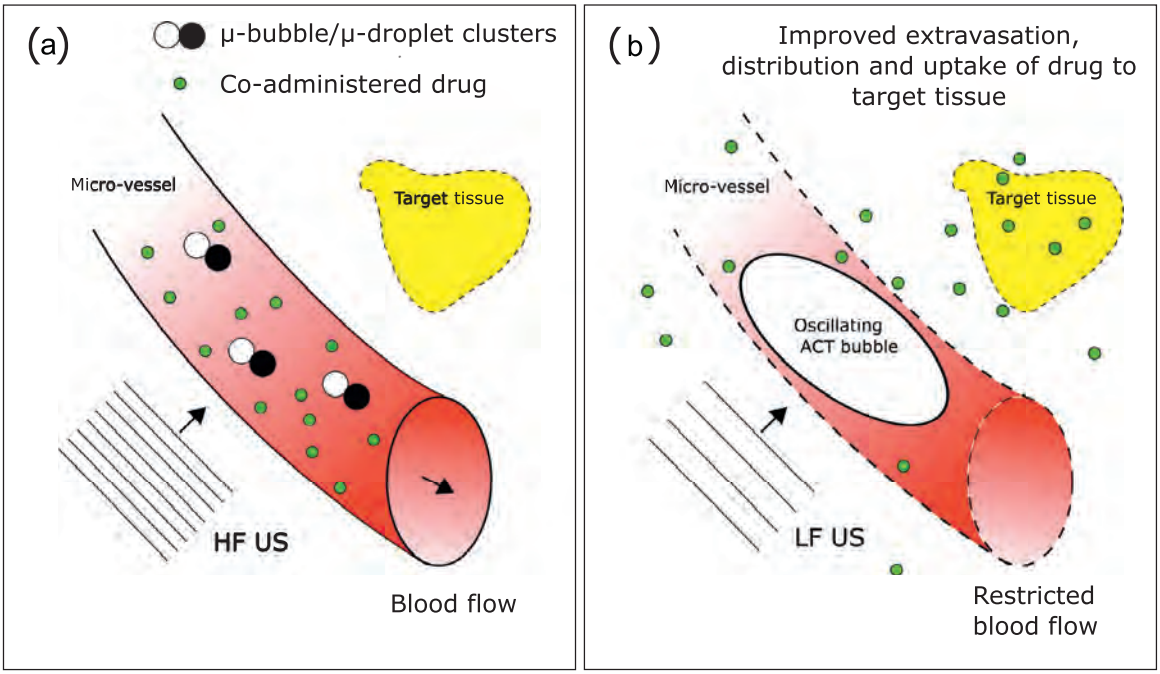

Fig. 1. Working principle of Acoustic Cluster Therapy (ACT): (a) High-frequency (>2.0 MHz) ultrasound insonate a micro-vessel and the microbubble/microdroplet clusters evaporate and forms the larger (~22 μm), gaseous ACT bubble presented in (b). (b) The gaseous ACT bubble lodge in the micro-vessel for about 5 to 10 min, during which low-frequency (0.5 MHz) ultrasound is used to insonate the tumour and obtain stable oscillate of the ACT bubble, thereby inducing biomechanic effects and enhancing the therapeutic efficacy of co-administered drugs. The working principle of ACT is described in detail in Sontum et al. (2015).

transducer. One approach is to place the active LF and HF layer next to one another, perpendicular to the propagation direction (Bouakaz et al. 2001). Another approach is to stack the active layers on top of each other in the propagation direction (Hossack and Auld 1993; Saitoh et al. 1995), alternatively with a passive isolation layer in between the active layers (Azuma et al. 2010; Myhre et al. 2017). However, a dual-frequency transducer may also be realised utilising the intrinsic harmonics of the piezoceramic (Frijlink et al. 2009). The harmonics are seldom utilised in US transducer designs in part because of the reduced sensitivity and the inherent pulse ringing of the harmonics. However, if the pulses are not used for imaging, but for invoking a physical effect (as in this study), pulse ringing is often not critical, and the desired output pressure can be scaled with the electric input voltage. One important benefit of utilising the harmonics in a dual-frequency transducer is a reduced complexity, which may improve the reliability and lifetime of the transducer.

In this report, we investigate whether the harmonics can be taken advantage of in a dual-frequency transducer designed specifically for pre-clinical *in vivo* studies of ACT on murine tumour models. The dual-frequency transducer is created of an air-backed piezoceramic disk with 2 matching layers, where the 5th harmonic (2.7 MHz) is used for activation of the ACT bubbles, and the fundamental frequency (0.5 MHz) is used to enhance the therapeutic efficacy of co-administered drugs. To reduce the ringing of the 5th harmonic pulse, a numerical optimisation method (Andersen et al. 2018, 2019) has been used to optimise the matching layers for transmission of sound at both the fundamental and 5th harmonic. Two different aperture sizes are used to limit the ACT activation to the tumour volume, and to align the HF and LF axial pressure maxima. The dual-frequency transducer is manufactured and incorporated in a laboratory setup for *in vivo* studies of ACT on murine tumour models. Throughout this report, both the dual-frequency transducer and the laboratory setup will be described.

Because it is unconventional to utilize the harmonics, we have used both *in vitro* and *in vivo* measurements to verify that the 5th harmonic can be used to activate the ACT bubbles. For the *in vivo* measurements, the kidneys of non-tumour−bearing mice were used as surrogates to avoid unnecessary suffering to the animals. The measurements are conclusive, and similar ACT activation levels with the dual-frequency transducer compared with clinical scanners have been achieved.

The first part of the Materials and Methods section in this report describes both the harmonic dual-frequency transducer and the pre-clinical *in vivo* laboratory setup, and the third section describes the methods used to experimentally verify the ACT bubble activation. In the Results section of this report, the focus is on the experimental performance of the transducer and its ability to activate the ACT bubbles both *in vitro* and *in vivo*. A publication with more technical details is available in Andersen et al. (2018).

MATERIALS AND METHODS

Dual-frequency transducer

In Figures 2 and 3, a cross-sectional view and a picture of the fundamental and 5th harmonic dual-frequency transducer are presented, respectively. In Table 1, the structural and material parameters are listed. The transducer is created of an air-backed Ferroperm Pz27 (Meggitt Sensing Systems, Kvistgaard, Denmark) piezoceramic disk with 4-mm thickness, 21-mm radius and ∼10-μm screen-printed silver electrodes. The transducer is acoustically matched to the water load by 2 passive matching layers where the thicknesses and impedances have been obtained by a numeric optimisation method described later in this report. A low-density polyurethane is used for mechanical support along the edges of the aluminium housing.

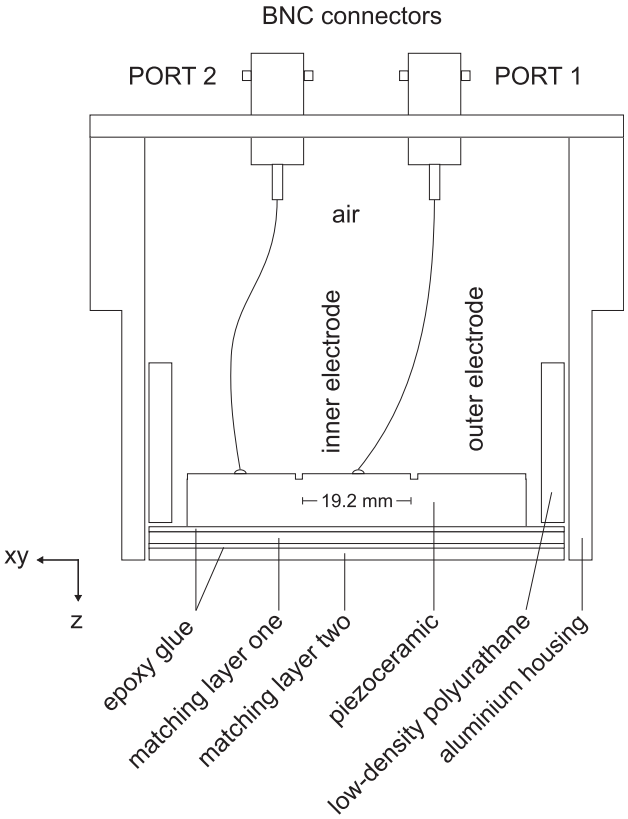

Fig. 2. Cross-sectional view of the dual-frequency transducer constructed of an air-backed single piezoceramic disk with two matching layers. The low-frequency and high-frequency axial beam maxima are aligned utilising two different acoustic apertures realised by separation of the hot (backside) electrode.

Fig. 3. A dual-frequency transducer.

Acoustic apertures. The largest tumour size we expect to treat is approimately 6 mm in linear dimension. It is important that the tumour is fully insonated by both the HF and LF US fields; however, if the HF US field is much larger than 6 mm, ACT activation outside of the tumour may result in an unwanted increase in the uptake of the co-administered drugs to normal, healthy tissue. Note that it is less critical if the LF US field encompasses more than the tumour. Because of this, the 2-sided −3dB HF beamwidth is chosen to be 6 mm, which thus defines the HF aperture size. The LF aperture size is chosen to align the LF and HF axial pressure maxima, allowing both the LF and HF US fields to be used close to their respective pressure maxima. The 2 different aperture sizes are realised by cutting through the hot (backside) electrode of the piezoceramic disk with a 1-mm milling cutting tool. The HF and LF aperture radii are 9.6 mm and 21 mm, respectively, which places the LF and HF axial pressure maxima at a distance of 150 mm and 166 mm from the front of the transducer, respectively. The distance to the murine tumour models is approximately 200 mm, and we use the dual-frequency transducer slightly beyond the last pressure maxima. For the HF, only the inner electrode is used, and the outer electrode is grounded. For the LF, both the inner and outer electrodes are used (*i.e.*, the full aperture is used; Fig. 2).

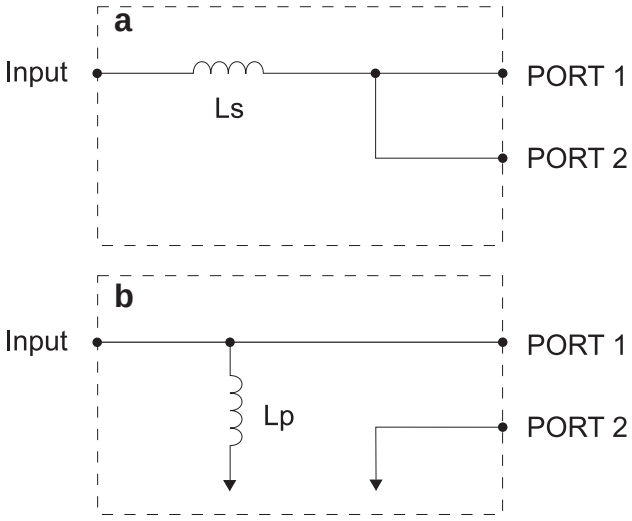

Fig. 4. Simplified schematics of the electric circuits for (a) LF and (b) HF tuning. The circuits are placed inside the switch box (*dashed lines*), and the two electrical configurations are realised with a rotary switch.

Electrical matching. To efficiently transfer the electric energy to acoustic energy, tuning inductors have been used to cancel out the transducers' electrical reactance. For the design choices made, the LF and HF electrical impedances required a 22-μH serial and 2.7-μH parallel inductor, respectively. Simplified schematics of the tuning circuits are presented in Figure 4.

In vivo *laboratory setup.* A schematic of the preclinical *in vivo* laboratory setup is presented in Figure 5. A signal generator is connected to a power amplifier connected to an analogue switch box. The switch box has two separate electric tuning circuits controlled by a rotary switch and two electrical output ports. The two outputs are connected to their respective Bayonet Neill−Concelman (BNC) connectors on the transducer. The transducer is placed in a water-stand-off made of 3-D printed acrylonitrile butadiene styrene (ABS) plastic and a Mylar film is used to close off the opening of the water stand-off. The water stand-off is locked in place in a water bag, and the acoustic energy couples to the murine tumour model through the water path and

Table 1. Structural and material parameters for the dual-frequency transducer

	l [mm]	a [mm]	Z [MRayl]	c [m/s]	Q [−]	$\varepsilon/\varepsilon_0$ [−]	h [GV/m]
Piezoceramic	3.98	21	33.5	4325	100	880	19.7
Matching layer one	1.01*	55	8.0*	2245	27	-	-
Matching layer two	1.05*	55	2.46*	2265	40	-	-
Epoxy glue	0.005	-	2.8	2450	12	-	-

l = layer thickness; a = radius; Z = characteristic acoustic impedance; c = sound speed; Q = quality factor; $\varepsilon/\varepsilon_0$ = relative permittivity; h = piezoelectric coefficient.

* Obtained by numeric optimisation.

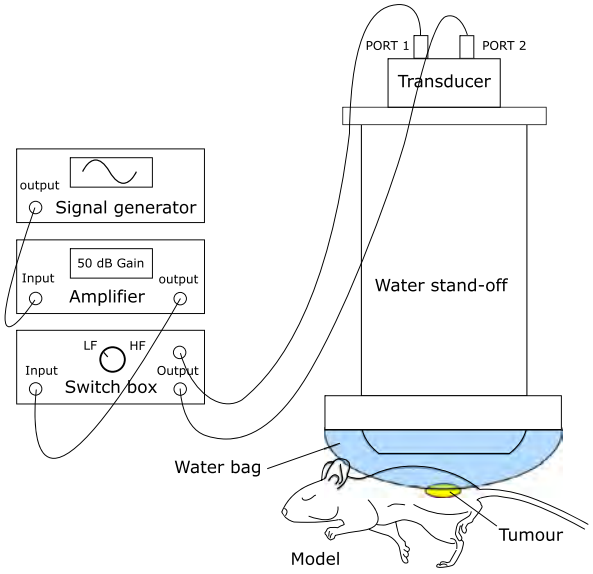

Fig. 5. Schematic of the laboratory setup designed for preclinical *in vivo* studies of ACT on murine tumour models.

coupling gel. The water stand-off is made water-proof, using a plastic primer and a clear lacquer and, to reduce reverberations, the inside of the water stand-off is coated with an acoustic absorber Aptflex F36 (Precicion Acoustics Ltd., Dorchester, UK). In-house made and purchased (Thorlabs Inc., Newton, NJ, USA) mounting accessories are used to hold and guide the water stand-off. The distance from the front of the transducer to the tumour is approximately 200 mm.

Alignment of the US beams with the tumour is achieved in the following manner: Before treatment, a hydrophone is placed below the water bag with the transducer and water-stand off locked in place. The pressure maximum is located with the hydrophone and indicated on the water bag with a cross-hair. The transducer and water stand-off can then be removed, and the murine's tumour can be viewed through the water bag and be aligned with the cross-hair.

Numerical optimisation method. If a conventional broadband analytical method (Desilets et al. 1978) is used to optimise the impedances of the matching layers, the 5th harmonic will exhibit a characteristic similar to a high Q resonator (*i.e.*, a narrow frequency band and correspondingly a long ring-down in the time domain). A numeric method has therefore been used to optimise the matching layers for transmission of sound at both the fundamental and 5th harmonic, with the primary objective of reducing the ringing associated with the 5th harmonic. The method is based on linearising the phase spectrum of a simulated electro-mechanic transfer function, shown by Pohlig (1980) to result in short pulses. In this report, we have linearised both the fundamantal and 5th harmonic passbands simultaneously, using equal weights at both passbands. The optimisation is performed using a gradient-based algorithm implementation in MATLAB's Global Optimization Toolbox (MATLAB, Natick, MA, USA) by searching for combinations of the impedances and thicknesses of the matching layers that linearises both the fundamental and 5th harmonic passbands. Details of the optimisation method can be found in Andersen et al. (2018), and the method is further described in Andersen et al. (2019).

Acoustic measurements

The acoustic measurements were performed using a calibrated Onda (Onda Corporation, Sunnyvale, CA, USA) HGL0200 Golden Lipstick hydrophone connected to an AG-2010 pre-amplifier mounted in an AIMS III measurement system controlled through MATLAB. Note that calibration of the HGL0200 hydrophone is difficult below 1 MHz because of an inherent resonance at approximately 0.6 MHz, and the pressure values obtained in this frequency range are therefore regarded as uncertain.

The transducer efficiency, η, quantifies the rate of energy transfer from electric to acoustic, and can be estimated by Sherman and Butler (2007)

$$10\log_{10}\eta = \mathrm{SL} - \mathrm{DI} - 170.8\ \mathrm{dB} - W_e, \quad (1)$$

where SL is the on-axis source level at 1 m referenced to 1 μPa, DI is the directivity index, 170.8 dB is the source level at 1 m for 1 acoustic watt from an omnidirectional radiator, and W_e is the input electrical power. Determining SL requires far-field conditions, which were not possible to achieve in the current laboratory setup. The measured pressure was therefore extrapolated from the near-field to a far-field equivalent, correcting for diffraction effects (Goldstein et al. 1998).

Experimental verification of ACT activation

The current section describes the materials and methods used to experimentally verify that the 5th harmonic can be used to activate the gaseous ACT bubbles. *In vitro* and *in vivo* measurements have been performed.

Microbubble/microdroplet clusters. The microbubbles employed were the commercially available US contrast agent Sonazoid (GE Healthcare, Oslo, Norway) with a volume-weighted median diameter of 2.6 μm. The microdroplet emulsion consisted of a perfluoromethylcyclopentane stabilised with a distearoylphosphatidylcholine phospholipid membrane containing 3% stearylamine to produce the positive surface charge. The microdroplets have a volume-weighted median diameter

of 2.8 μm. The microbubble/microdroplet compound for injection was prepared by reconstituting a vial of Sonazoid with 2 mL of the microdroplet emulsion. See Sontum et al. (2015) for further details.

In vitro *ACT activation.* An acoustic transmission technique was used to measure the size population of the gaseous ACT bubbles *in vitro*. Details of the measurement method is provided in Healey et al. (2016). The technique quantifies the number of activated ACT bubbles in a size range from 4−80 μm in 2-μm diameter intervals. The measurements were performed in the following manner: A sample cell containing 250 ml Isoton II was placed in a water bath (37.0 ± 0.5˚C). A 250-kHz transducer (Olympus Videoscan, part V1012, Waltham, MA, USA) was used to transmit and receive a broadband pulse through the sample cell, which reflected off a steel plate. The microbubble/microdroplet compound was diluted 1:10 in sterile water for injection and 30 μL was added to the sample cell. Sonication of the sample cell was achieved by moving the dual-frequency transducer in front of the sample cell 5 seconds after injection for 25 seconds. The bubble activation was recorded for 445 seconds in 5-s intervals, and each measurement was an average of 200 transmissions. The peak gas volume fraction in the sample cell was used as the metric to quantify the size population of the gaseous ACT bubbles. Four vials of microbubble/microdroplet compounds were reconstituted and, for each vial, we compared the dual-frequency transducer with a clinical scanner (Zonare with a P10-4 probe; Zonare Medical Systems, Inc., Mountain View, CA, USA). The dual-frequency transducer's settings were: 2.7 MHz, 20 period sine, pulse repetition frequency of 0.5 kHz and an MI of 0.5. The clinical scanner's settings were: 4 MHz with an MI of 1.3 set to 10 cm image depth.

Animal model. The kidneys of non-tumour−bearing female athymic nude mice, ICR: Ncr-Foxn1 (nu), were used as tumour surrogates. All mice were treated per local and national animal welfare guidelines (Workman et al. 2010), were housed in individually ventilated cages and allowed access to food and water *ad libitum*. Before treatments, anaesthesia was induced by subcutaneous injection of fentanyl citrate + fluanisone (Hypnorm, Vetapharma Ltd, Leeds, UK) and midazolam (Hypnovel, Roche Products Ltd, Welwyn Garden City, UK) (0.28:10:4.5 mg/kg). The ACT compound (50-μl bolus) was injected into the lateral tail vein of the mouse. During treatments, the mice were maintained on a mouse handling table (Vevo, Fujifilm Visualsonics Inc., Toronto, ON, Canada). The body temperature was controlled thermostatically and vital signs were carefully monitored. After treatments, the mice were kept in a temperature-controlled recovery chamber until fully recovered.

In vivo *ACT activation.* Because of the size, the activated and gaseous ACT bubbles will reflect more acoustic energy and therefore increase the contrast in an US image, compared with the microbubbles/microdroplets compound. *In vivo* ACT activation can, therefore, be estimated using US imaging by monitoring the change in image contrast over time.

The image acquisition was performed using dual B-mode and contrast imaging with a Toshiba Aplio XG clinical US scanner and a 1204BT linear array probe operating at 8 MHz (Toshiba Corp., Tokyo, Japan). Imaging at 8 MHz has a sufficient resolution to discern details in the small animals, and to allow the monitoring of the change in image contrast over time. The image acquisition MI was 0.01, which is too low to activate the ACT bubbles, and the imaging did therefore not influence the results.

For the *in vivo* ACT activation estimates, we used the kidneys of non-tumour−bearing mice as surrogates. The microbubble/microdroplet compound was injected in the mice, and ACT activation was performed using the dual-frequency transducer placed over the kidney. After injection, the 5th harmonic (2.7 MHz) was used to insonate the kidney for 45 s, using a 20 period sine with an MI of 0.2 and a pulse-repetition frequency of 1 kHz. To monitor the contrast, image acquisition was subsequently performed with the Toshiba scanner from 1.5 min, followed by 10-s video clips every minute until 9-min post-injection.

To compare the activation levels obtained with the dual-frequency transducer, we also used the Toshiba scanner for ACT activation. After injection, the Toshiba scanner was used for activation using a contrast mode MI of 0.32 for 45 s. After 45 s, the MI was lowered to 0.01 and 2 min of continuous video was first acquired, followed by 10-s video clips every minute until 9-min post-injection.

Finally, we performed a control using Sonazoid administration only. For the control, we used the Toshiba scanner for activation with a contrast mode MI of 0.32 for 45 s. Image acquisition was performed after 45 s with an MI of 0.01. First, we acquire 2 min of continuous video, followed by 10-s video clips every minute until 9-min post-injection.

Between each acquisition, the kidney was insonated for 3 min with the highest MI available in contrast mode (1.09) to remove any residual signal. Post-treatment, the image contrast enhancement was quantified in B-mode from the recorded videos from a region of interest drawn manually over the kidney. The results are shown as the image intensity as a function of time.

RESULTS AND DISCUSSION

Transducer characterisation

In Table 2, we compare measured and simulated figures of merit for the dual-frequency transducer. All simulations were conducted in Comsol (Comsol AB, Stockholm, Sweden) except the beamwidths, where Field II (Jensen 1996; Jensen and Svendsen 1992) was employed. In Table 2, we see that the relative LF bandwidth is 5.1 times wider than the relative HF bandwidth; however, the absolute bandwidths are practically identical. The similarity in the absolute bandwidths is a consequence of optimising the transducer for a linear phase simultaneously at the fundamental and 5th harmonic passbands, using equal weights at both passbands. The similarities in the HF and LF absolute bandwidths are also reflected in the simulated impulse responses, which are also practically identical. Compared with a conventional analytic broadband optimisation method (Desilets et al. 1978), simulations show that the linear phase optimised transducer has a 200% wider bandwidth and a 50% shorter impulse response length at the 5th harmonic (Andersen et al. 2018).

Acoustic beam pattern. In Figure 6, measurements of 4 acoustic-beam profiles are presented. The beam profiles are representative for the pre-clinical *in vivo* US fields, and are shown as the

$$\text{Pulse energy} \propto \int_{-\infty}^{\infty} |p(t,x,y,z)|^2 dt, \qquad (2)$$

where p is the time-domain pressure. Note that eqn (2) does not, strictly speaking, quantify the energy in a pulse, but is a convenient way of representing the measurements. The LF and HF electric excitation pulses were a 2-period 0.5 MHz sine (a,b) and a 12-period 2.7 MHz sine (c,d), respectively. The measured and simulated (*in parenthesis*) −3 dB beamwidths at 200 mm are 16 mm (15.8 mm) and 6 mm (6 mm) for the LF and HF, respectively. A critical design criterion was the HF −3 dB beamwidth of 6 mm, which has been achieved.

Table 2. Figures of merit for the fundamental and 5th harmonic dual-frequency transducer

	meas.		sim.	
Quantity	LF	HF	LF	HF
−3 dB rel. BW (%)	41	8.0	46	7.9
−3 dB abs. BW (MHz)	0.21	0.22	0.22	0.22
−20 dB impulse length (μs)	-	-	5.8	5.5
−3 dB beamwidth (mm)	16	6	15.8	6
−3 dB depth of field (rel. max) (mm)	225	175	-	-
Efficiency (%)	73	44	90	43

meas., measured; sim., simulated; rel., relative; BW, bandwidth; abs, absolute

Acoustic pulses. In Figure 7, measurements of the LF and HF pressure pulses are presented. The pulses are measured on-axis at $z = 200$ mm, and the LF and HF electric excitation pulses were a 2-period 0.5 MHz sine (Fig. 7a) and a 12-period 2.7 MHz sine (Fig. 7b), respectively. For both pulses, a generator voltage of 5-V peak amplitude was used and the peak-negative pressure levels are approximately −30 kPa for both the LF and HF pulses. The peak-negative pressure values used for the *in vivo* studies are −0.14 MPa and −0.58 MPa for the LF and the HF pulses, respectively, both of which are achieved using a power amplifier.

The pulse in (Fig. 7a) exhibits a conventional broadband response typically used in US imaging applications recognized by a short rise-time, few pulse cycles (3−4) to reach steady-state conditions, and a low time-sidelobe level (−27 dB). The pulse in (Fig. 7b) exhibit ringing that renders it unsuited for imaging purposes; however, for the current study, the 2.7-MHz pulses are used for ACT activation only. Later in this report, we show that the 5th harmonic shows comparable ACT activation levels compared with clinical scanners.

Efficiency. The measured and simulated (*in parenthesis*) LF and HF efficiencies are 73% (90%) and 44% (43%), respectively. The measured and simulated LF efficiencies deviate by 17%, and the reason for this discrepancy is attributed to the hydrophone calibration, discussed before in this report. The measured and simulated HF efficiencies compare well, and we note that an HF efficiency of 44% demonstrates that the 5th harmonic can be used to transmit acoustic energy. Compared with the LF efficiency, the HF efficiency is lower in value. A lower efficiency means that less of the electrical energy is transformed to “usable” acoustic energy and is dissipated as heat inside the transducer.

Experimental verification of ACT activation

In vitro *ACT activation.* In Figure 8, the peak gas volume fraction in the sample cell after activation with the dual-frequency transducer is compared with the clinical scanner (Zonare with a P10-4 probe). The clinical scanner’s MI level (1.3) was used to obtain maximum evaporation of the oil droplets (Healey et al. 2016), and the dual-frequency transducer’s MI (0.5) was chosen to be closer to what is used for the pre-clinical *in vivo* testing of ACT on tumours in mice (0.35). The results show comparable activation levels for both transducers with small variations between the two transducers and the different vials. On average, the dual-frequency transducer shows a 5% lower activation level compared to the clinical scanner; however, this

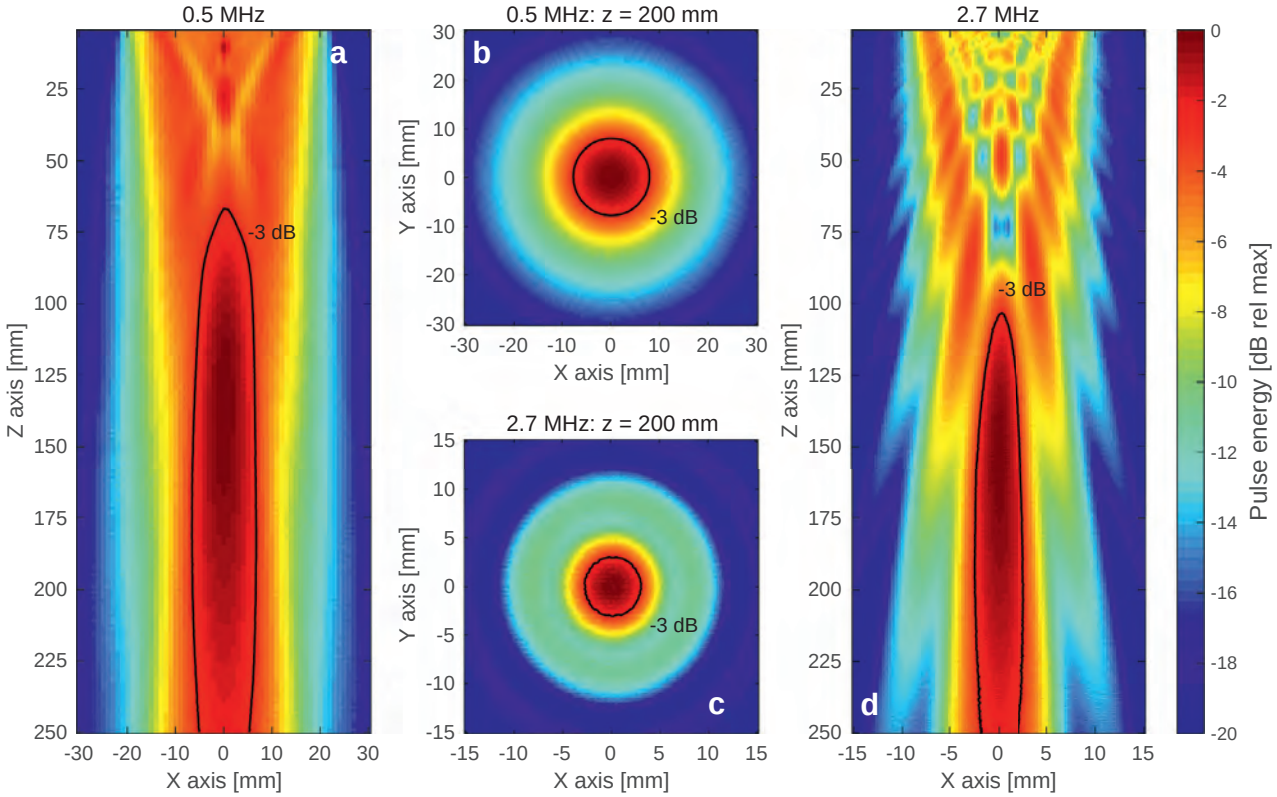

Fig. 6. Measurements of the transducer's acoustic beam patterns.The colorbar (*right*) is applicable to all figures, and the annotated −3 dB black contour line indicate where the pulse energy has dropped −3 dB from the maximum. Note that the X, Y and Z axes are not to scale.

difference is considered to be within the measurement uncertainties.

Although the 2 transducers used different MI levels and frequencies, the measurements support earlier results that ACT activation may be performed above ∼2 MHz, as long as the MI is above ∼0.15 (Healey et al. 2016), and demonstrate that the dual-frequency transducer is capable of *in vitro* ACT activation.

In vivo *ACT activation.* In Figure 9, *in vivo* ACT activation with the dual-frequency transducer is compared with the Toshiba scanner. A control was performed, where the Toshiba scanner was used for activation and only Zonazoid was administered to the mice. The dual-frequency transducer's MI (0.2) was chosen slightly lower than 0.35 to reduce non-linear distortions in the HF pulses, and still delivering enough energy to evaporate the oil microdroplets. The kidneys of a non-tumour−bearing mice were used, and the results are presented as the region-of-interest image intensity as a function of time. After activation with the dual-frequency transducer, imaging commenced at 1.5-min post-injection. Therefore, we do not have any data before 1.5 min. However, at 1.5 min, the dual-frequency transducer show a comparable intensity level to the Toshiba scanner, and both intensity levels show a similar and exponential decay from 1.5 min to 9 min. The image intensity decays because the gas in the ACT bubbles diffuses into the blood stream, which, after 5−10 min transports the bubbles away. Based on this, we infer that the dual-frequency transducer is capable of *in vivo* ACT activation.

For the control, the video sequences indicate a slight movement of the animal at approximately 50-s post-injection. More of the kidney cortex was therefore present in the image, which increased the region-of-interest contrast enhancement and is responsible for the modest rise in image intensity observed after 50 s. The control shows that the contrast enhancement originating from the Sonazoid alone is significantly lower and dies out earlier compared with ACT administration.

CONCLUSIONS

A dual-frequency transducer for ACT has been designed, manufactured and tested. The transducer utilises the fundamental (0.5 MHz) and 5th (2.7 MHz)

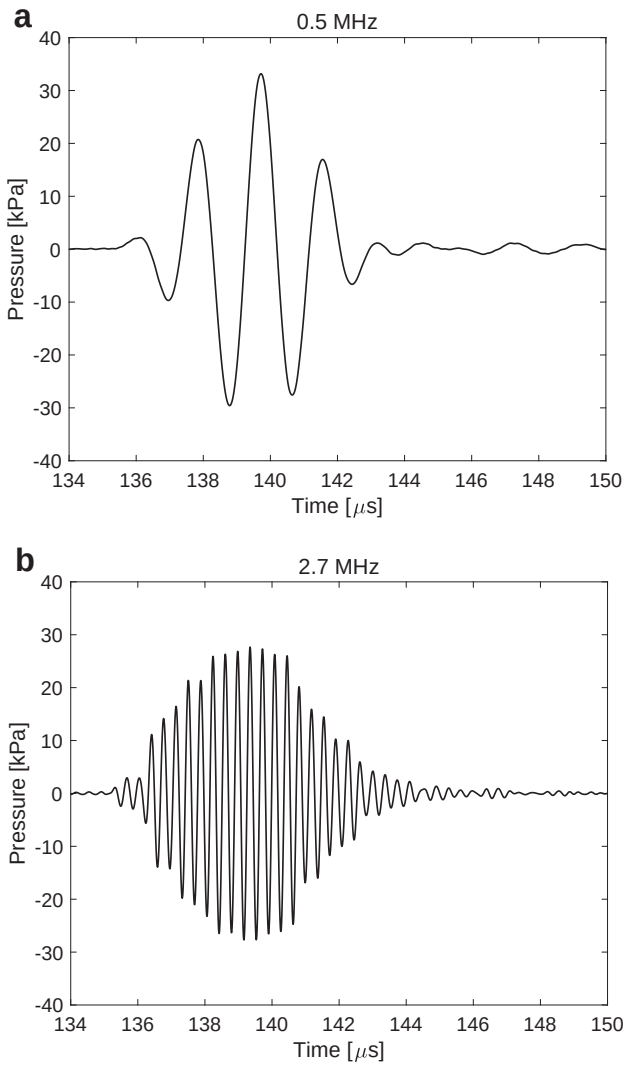

Fig. 7. Measured on-axial pulses at $z = 200$ mm for (a) 0.5 MHz 2-period 5 V peak sine excitation, and (b) 2.7 MHz 12-period 5 V peak sine excitation.

harmonic of a single piezoceramic disk: the 5th harmonic is used to activate the gaseous ACT bubbles, and the fundamental is used to obtain stable oscillations of the ACT bubbles, thereby inducing biomechanic effects and enhancing the therapeutic efficacy of co-administered drugs. *In vitro* and *in vivo* measurements demonstrate that the transducer is suited to be used for preclinical *in vivo* studies of ACT on murine tumour models. The dual-frequency transducer replaces a cumbersome two-transducer setup, and thus assists and simplifies workflow procedures and helps mitigate human errors. The dual-frequency system is currently in use at several research facilities.

Acknowledgments—This work was supported by the Research Council of Norway (grant number 237887).

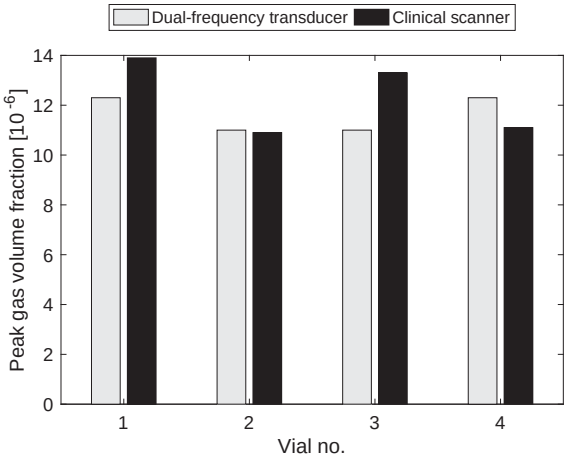

Fig. 8. Peak gas volume fraction in the sample cell after ACT activation with the dual-frequency transducer compared with the clinical scanner.

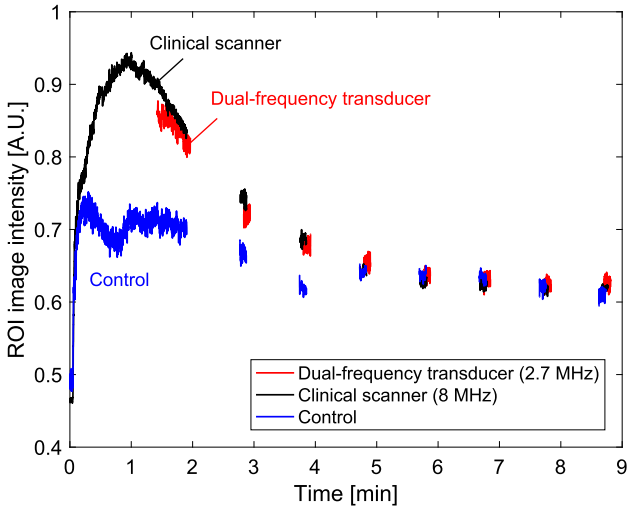

Fig. 9. Region-of-interest image intensity of *in vivo* ACT activation in the kidney of a living murine model, using the dual-frequency transducer (*red*), a clinical scanner (*black*) and a control with Sonazoid administration only (*blue*).

REFERENCES

Andersen KK, Frijlink ME, Hoff L. A numerical optimization method for transducer transfer functions by the linearity of the phase spectrum. IEEE Trans Ultrason Ferroelectr Freq Control 2019;66: 71–78.

Andersen KK, Healey AJ, Bush NL, Frijlink EM, Hoff L. Design, fabrication, and testing of a dual-frequency transducer for acoustic cluster therapy activation. 2018 IEEE International Ultrasonics Symposium. Piscataway, NJ. IEEE; 2018. p. 1–4.

Åslund AK, Snipstad S, Healey A, Kvåle S, Torp SH, Sontum PC, de Lange Davies C, van Wamel A. Efficient enhancement of blood-brain barrier permeability using Acoustic Cluster Therapy (ACT). Theranostics 2017;7:23–30.

Azuma T, Ogihara M, Kubota J, Sasaki A, Umemura Si, Furuhata H. Dual frequency ultrasound imaging and therapeutic bilaminar array using frequency selective isolation layer. IEEE Trans Ultrason Ferroelectr Freq Control 2010;57:1211–1224.

Bouakaz A, Frigstad S, Ten Cate FJ, de Jong N. Super harmonic imaging: A new imaging technique for improved contrast detection. Ultrasound Med Biol 2001;28:59–68.

Desilets CS, Fraser JD, Kino GS. The design of efficient broad-band piezoelectric transducers. IEEE Trans Sonics Ultrason 1978;25: 115–125.

Frijlink ME, Løvstakken L, Torp H. Investigation of transmit and receive performance at the fundamental and third harmonic resonance frequency of a medical ultrasound transducer. Ultrasonics 2009;49:601–604.

Goldstein A, Gandhi DR, O'Brien WD. Diffraction effects in hydrophone measurements. IEEE Trans Ultrason Ferroelectr Freq Control 1998;45:972–979.

Healey AJ, Sontum PC, Kvåle S, Eriksen M, Bendiksen R, Tornes A, Østensen J. Acoustic Cluster Therapy: *In vitro* and *ex vivo* measurement of activated bubble size distribution and temporal dynamics. Ultrasound Med Biol 2016;42:1145–1166.

Hossack JA, Auld BA. Improving the characteristics of a transducer using multiple piezoelectric layers. IEEE Trans Ultrason Ferroelectr Freq Control 1993;40:131–139.

Jensen JA. Field: A Program for Simulating Ultrasound Systems. Paper presented at the 10th Nordic-Baltic Conference on Biomedical Imaging Published in Medical & Biological Engineering & Computing Volume 34, Supplement 1, Part 1, 351–353.

Jensen JA, Svendsen NB. Calculation of pressure fields from arbitrarily shaped, apodized, and excited ultrasound transducers. IEEE Trans Ultrason Ferroelectr Freq Control 1992;39:262–267.

Kotopoulis S, Stigen E, Popa M, Safont MM, Healey A, Kvåle S, Sontum P, Gjertsen BT, Gilja OH, McCormack E. Sonoporation with Acoustic Cluster Therapy (ACT) induces transient tumour volume reduction in a subcutaneous xenograft model of pancreatic ductal adenocarcinoma. J Control Release 2017;245:70–80.

Li B, Li Q, Mo J, Dai H. Drug-loaded polymeric nanoparticles for cancer stem cell targeting. Front Pharmacol 2017;8:51.

Lin CY, Pitt WG. Acoustic droplet vaporization in biology and medicine. Biomed Res Int 2013;2013 404361.

Myers R, Coviello C, Erbs P, Foloppe J, Rowe C, Kwan J, Crake C, Finn S, Jackson E, Balloul JM, Story C, Coussios C, Carlisle R. Polymeric cups for cavitation-mediated delivery of oncolytic vaccinia virus. Mol Ther 2016;24:1627–1633.

Myhre OF, Johansen TF, Johan Angelsen BA. Analysis of acoustic impedance matching in dual-band ultrasound transducers. J Acoust Soc Am 2017;141:1170–1179.

Pohlig SC. Signal duration and the fourier transform. In: Proceedings of the IEEE. Vol. 68, No.5. Piscataway, NJ. IEEE; 1980. p. 629–630.

Saitoh S, Izumi M, Mine Y. A dual frequency ultrasonic probe for medical applications. IEEE Trans Ultrason Ferroelectr Freq Control 1995;42:294–300.

Sherman CH, Butler JL. Transducers and arrays for underwater sound. New York, NY: Springer; 2007.

Sontum P, Kvåle S, Healey AJ, Skurtveit R, Watanabe R, Matsumura M, Østensen J. Acoustic Cluster Therapy (ACT)—A novel concept for ultra sound mediated, targeted drug delivery. Int J Pharm 2015;495:1019–1027.

Van Wamel A, Healey A, Sontum PC, Kvåle S, Bush N, Bamber J, de Lange Davies C. Acoustic Cluster Therapy (ACT)—Pre-clinical proof of principle for local drug delivery and enhanced uptake. J Control Release 2016;224:158–164.

Workman P, Aboagye EO, Balkwill F, Balmain A, Bruder G, Chaplin DJ, Double JA, Everitt J, Farningham DAH, Glennie MJ, Kelland LR, Robinson V, Stratford IJ, Tozer GM, Watson S, Wedge SR, Eccles SA. Guidelines for the welfare and use of animals in cancer research. Br J Cancer 2010;102:1555–1577.

C. Paper C

Design, Fabrication, and Testing of a Dual-Frequency Transducer for Acoustic Cluster Therapy Activation

Kenneth K. Andersen[a], Andrew J. Healey[b] Nigel L. Bush[c]

Martijn E. Frijlink [a], and Lars Hoff [a].

[a] Department of Microsystems, University of South-Eastern Norway, Horten, Norway.

[b] Phoenix Solutions AS, PO Box 4741, N-0421 Oslo, Norway.

[c] Joint Department of Physics, Division of Radiotherapy and Imaging, the Institute of Cancer Research, London, UK.

Design, Fabrication, and Testing of a Dual-Frequency Transducer for Acoustic Cluster Therapy Activation

Kenneth K. Andersen*§, Andrew J. Healey†, Nigel L. Bush‡, Martijn E. Frijlink*, Lars Hoff*
*Department of Microsystems, University of South-Eastern Norway, Horten, Norway
†Phoenix Solutions AS, PO Box 4741, N-0421 Oslo, Norway
‡Joint Department of Physics, Division of Radiotherapy and Imaging, the Institute of Cancer Research, London, UK.
§Email: Kenneth.Andersen@usn.no

***Abstract*—Acoustic Cluster Therapy (ACT) is a two-component formulation of commercially available microbubbles and microdroplets currently under development for cancer treatment. Promising studies of ACT have been performed on murine tumour models; however, ACT requires exposure to high- and low-frequency ultrasound (US) and in the studies, two transducers were therefore used. A two-transducer set-up require careful spatial alignment of the high- and low-frequency US fields and replacement with a single dual-frequency transducer with coaxial US fields is therefore desirable. This paper describes the design and testing of a dual-frequency transducer for ACT. The 1st and 5th harmonics of a single piezoceramic disk are used for the low- and high-frequency regimes, respectively. In vitro sonometry measurements demonstrate that the transducer is suited for preclinical in vivo studies of ACT. The dual-frequency transducer replaces a cumbersome two-transducer set-up and is currently in use for preclinical in vivo studies of ACT.**

I. Introduction

Acoustic Cluster Therapy (ACT) is a two-component formulation of commercially available microbubbles (Sonazoid, GE Healthcare, Oslo, Norway) and microdroplets (perfluorated oil) currently under development for cancer treatment [1]. ACT employs two ultrasound (US) exposure regimes: Firstly, high-frequency (HF > 2.0 MHz) US evaporates the oil and forms ACT bubbles (22 µm mean diameter [2]) which lodge at the microvascular level. Secondly, low-frequency (LF = 0.5 MHz) US induces stable oscillations of the gaseous ACT bubbles, thereby inducing biomechanical effects and enhancing the therapeutic efficacy of co-administered drugs (referred to as therapy). Promising studies of ACT on murine tumour models have been performed; however, two transducers were used in the experiments which require careful spatial alignment of the acoustic fields for consistent results. Replacement with a single dual-frequency transducer with coaxial US fields is therefore desired for future animal testing.

In the current paper, we investigate if the harmonics can be taken advantage of in a dual-frequency transducer for preclinical testing of ACT on murine tumours. A 1st and 5th harmonic dual-frequency transducer comprised of an air-backed piezoceramic disk with two matching layers is designed, manufactured and tested. The 5th harmonic (2.7 MHz) is used for generation of the gaseous ACT bubbles and the 1st harmonic (0.5 MHz) is used for the therapy response. A numerical optimisation method [3] has been used to optimise the matching layers for transmission of sound at both harmonics, with the primary objective of reducing the ringing of the 5th harmonic pulse. Alignment of the coaxial pressure maxima is achieved by using two different aperture radii.

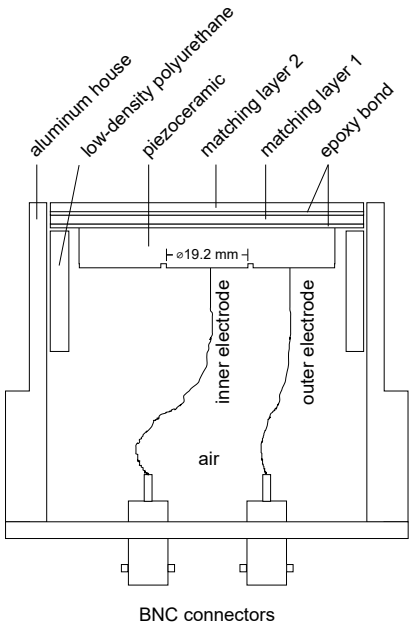

Fig. 1. A schematic of the dual frequency transducer comprised of an air-backed single piezoceramic disk with two matching layers. The 5th harmonic (2.7 MHz) is used to activate the gaseous ACT bubbles, and the 1st harmonic (0.5 MHz) is used to induce biomechanical effects.

II. Transducer Design

In Figure 1 and 2, a schematic and a picture of the dual-frequency transducer is given, respectively. The material parameters are listed in Table I, where l is layer thickness, a is radius, Z is characteristic acoustic impedance, Q is quality factor, ϵ/ϵ_0 is relative permittivity, and h is piezoelectric coefficient. The transducer is comprised of an air-

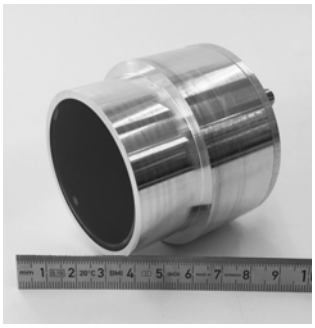

Fig. 2. A picture of the dual-frequency transducer.

TABLE I
STRUCTURAL AND MATERIAL PARAMETERS FOR THE DUAL-FREQUENCY TRANSDUCER.

	l [mm]	a [mm]	Z [MRayl]	c [m/s]	Q [-]	ϵ/ϵ_0 [-]	h [GV/m]
Pz27	3.98	21	33.5	4325	100	880	19.7
ML 1	1.01*	55	8.0*	2245	27	-	-
ML 2	1.05*	55	2.46*	2265	40	-	-
Epoxy	0.005	-	2.8	2450	12	-	-

*Obtained by numerical optimisation.
ML = matching layer.

backed Ferroperm™ Pz27 (Meggitt Sensing Systems, Denmark) piezoceramic disk and two passive matching layers; the thicknesses and impedances have been obtained by a numerical optimisation method described in Sec. II-A. The transducer has two acoustical apertures to allow coaxial alignment of the transmitted beam maxima, realised by separation of the hot (backside) electrode by a milling cutter. The acoustic aperture radii are $9.6\,\mathrm{mm}$ and $21\,\mathrm{mm}$ for the HF and LF, respectively. For the HF, only the inner electrode is used, and the outer electrode is grounded. For the LF, both electrodes are used. The transducer's electrical reactance was tuned out using inductors: The LF required a $22\,\mu\mathrm{H}$ series inductor, and the HF required a $2.7\,\mu\mathrm{H}$ parallel inductor.

A. Numerical optimization method

Conventional broadband analytical optimisation methods, e.g., [4], do not lend themselves easily to complex transducer designs. A numerical method based on linearising the phase spectrum of the transducer's electro-mechanical transfer function has therefore been employed to optimise the matching layers for transmission of sound at both the 1st and 5th harmonics. The linear phase method has been described in [3] and we hereby extend this to include two frequency bands. The optimisation is performed using 1D simulations [5].

Let $H \equiv U/V$ denote the spectral electro-mechanical transfer function, where U is the complex normal particle velocity at the face of the transducer, V is the complex input voltage at the terminals of the transducer, and $H = |H|\exp(i\theta)$, where $|H|$ denotes magnitude and θ is the spectral phase. To quantify the linearity of the spectral phase, we fit a regression line, θ_l, to the spectral phase in the 1st and 5th harmonic passbands and calculate the absolute mean differences between the regression lines and the spectral phase in each passband, i.e.,

$$E^n(F^n, \bar{x}) = \frac{1}{M^n}\sum_{i=1}^{M^n} |\theta(F_i^n, \bar{x}) - \theta_l^n(F_i^n, \bar{x})|, \qquad (1)$$

where the superscript n is used to distinguish between the 1st and 5th harmonic passbands, F^n are the frequency ranges where the regression lines are fitted, and M^n are the total number of discrete frequency points in each frequency range. The total difference between the regression lines and the spectral phase is a linear sum of the differences in each passband

$$E = E^{1\mathrm{st}} + E^{5\mathrm{th}}. \qquad (2)$$

The transducer is optimised by numerically searching for combinations of the impedances and thicknesses of the matching layers that minimise E. For the current study, the optimisation variables are

$$\left\{\frac{Z_m^1}{Z_p}, \frac{Z_m^2}{Z_p}, \frac{l_m^1}{\lambda_m^1}, \frac{l_m^2}{\lambda_m^2}\right\} \subset \bar{x}, \qquad (3)$$

where Z_p denotes the characteristic impedance in the piezoceramic, Z_m, l_m, and λ_m are the characteristic impedances, thicknesses, and wavelengths in matching layer 1 and 2, denoted by the superscript. The optimisation is performed using a gradient-based algorithm implementation in MATLAB's *Global Optimization Toolbox*.

III. EXPERIMENTAL SET-UP

A. Acoustical measurements

Acoustical measurements were performed using a calibrated Onda (Onda Corporation, CA, USA) HGL0200 *Golden Lipstick* hydrophone connected to an AG-2010 pre-amplifier mounted in an AIMS III measurement system controlled through Matlab. Note: The hydrophone used in this study has an inherent resonance peak at 0.6 MHz. Calibration in this range is difficult, and this causes uncertainty in the measured pressure values in the lower frequency range. The on-axis spectral pressure, $P(f, z)$, at the position z of the hydrophone is obtained by dividing the spectrum of the measured voltage with the hydrophone and pre-amplifier calibration data. A measurement of the magnitude of the electro-mechanical transfer function H is obtained from

$$H = \frac{P(f, z)}{V(f)D(f, z)Z_L}, \qquad (4)$$

where $V(f)$ is the spectrum of the measured voltage at the transducer terminals, $D(f, z)$ is diffraction correction [6], and Z_L is the characteristic impedance of water.

B. In vitro sonometry

An acoustic transmission technique – referred to as sonometry – was used to measure the size population of the gaseous ACT bubbles in vitro [2]. The method quantifies the number of ACT bubbles activated by US exposure into a sample cell. A sample cell was placed inside a water bath ($37.0 \pm 0.5\,^{\circ}\mathrm{C}$) and the ACT compound was injected to the sample cell. US exposure of the sample cell was achieved by moving the transducer in front of the sample cell 5 seconds after injection for a duration of 25 seconds. The bubble activation was recorded for 445 seconds in 5 seconds intervals, and each measurement was averaged 200 times. The peak gas volume fraction in the sample cell was used as the metric to quantify the activation of the gaseous ACT bubbles. ACT activation with the dual-frequency transducer was compared to a clinical scanner (Zonare with a P10-4 probe) using four separate ACT vials. The dual-frequency transducer's settings were: 20 period sine with an MI of 0.5; the clinical scanner's settings were: 4 MHz with an MI of 1.3.

IV. Results and discussion

A. Numerical optimisation

In Figure 3, 1D simulations of the magnitude of the electro-mechanical transfer function H for the linear phase optimised transducer is shown for both the 1st and 5th harmonics. The results are compared to a *broadband* transducer optimized at the 1st harmonic using the equations derived by Desilets [4]. All curves are normalised to the maximum for the linear phase optimised transducer. The broadband transducer exhibits a conventional flat and wideband response at the 1st harmonic compared to the 5th harmonic which exhibits a high Q resonating characteristic. In contrast to the broadband transducer, the linear phase optimised transducer exhibits comparable absolute bandwidths at both harmonics. The -3 dB relative bandwidths are 46% (63%) and 7.9% (2.6%) for the 1st and 5th harmonic, respectively (broadband transducer in parenthesis). The most notable difference between the two transducers is seen at the fifth harmonic: The linear phase optimised transducer has a 200% wider bandwidth and a $50\,\%$ shorter impulse response length compared to the broadband transducer.

B. Electro-mechanical transfer function

In Figure 4, measurements on $|H|$ are compared to simulations using a 1D equivalent circuit model [5] and 2D FEM (Comsol AB, Stockholm, Sweden) for the (a) 1st and (b) 5th harmonic passbands. In Figure 4 (a), a fair overall agreement is observed between the three representations of $|H|$. However, below 0.5 MHz the measurement is lower in value compared to both simulations: This discrepancy is ascribed to uncertainties in the hydrophone calibration data (cf. Sec. III). Below 0.4 MHz, both the measurement and 2D simulation exhibit radial resonances. The deviations in the radial resonances we ascribe to material parameters and production artefacts.

In Figure 4 (b), around 2.7 MHz the three representations of $|H|$ exhibit a fair agreement. Below 2.4 MHz an interesting deviation between the 1D simulation, measurement and 2D simulation is observed: the measurement and 2D simulation exhibit even harmonic resonances. An ideal piezoelectric resonator in thickness mode has no coupling between the electric field and the mechanical resonances at the even harmonics. However, the HF electrical configuration utilises only the inner electrode, while the hot outer electrode is grounded, and this structure can allow even harmonic resonances to be excited by the diverging electric field. The even harmonics are observed throughout the examined frequency range if the inner electrode is used, but no even harmonics are seen if the full aperture size is used

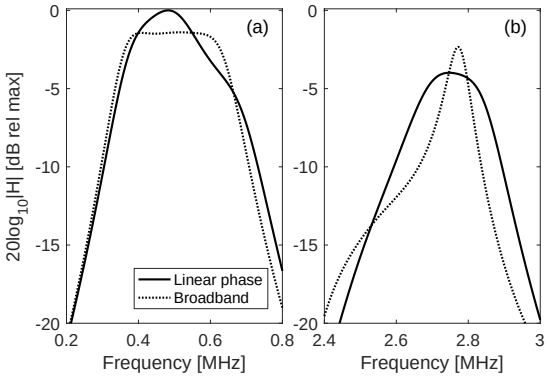

Fig. 3. 1D simulations of the magnitude of the electro-mechanical transfer function H for the linear phase optimised transducer compared to a broadband transducer around the (a) 1st and (b) 5th harmonic passbands.

TABLE II
Peak gas volume fraction [10^{-6}] in a sample cell after ACT activation with the dual-frequency transducer compared to a clinical scanner.

Vial no.	1	2	3	4
Dual-frequency	12.3	11.0	11.0	12.3
Scanner	13.6	10.9	13.3	11.1

C. Acoustic fields

In figure 5, hydrophone measurements of the radial acoustic fields at $z = 200\,\mathrm{mm}$ are shown for the (a) LF (0.5 MHz, 2 period sine excitation) and the (b) HF (2.7 MHz, 12 period sine excitation). An important design criterion was the HF $-3\,\mathrm{dB}$ beam width which, for the targeted ACT application, should match the murine tumour size of $6\,\mathrm{mm}$. The $-3\,\mathrm{dB}$ beam widths are 14.9 mm and 6 mm for the LF and HF, respectively, and we note that we have achieved the required HF beam width.

D. In vitro sonometry

In Table II, the results from the in vitro sonometry measurements on ACT activation are given as the peak gas volume fraction. The results show comparable activation levels for both transducers with small variations between the two transducers and the different vials.

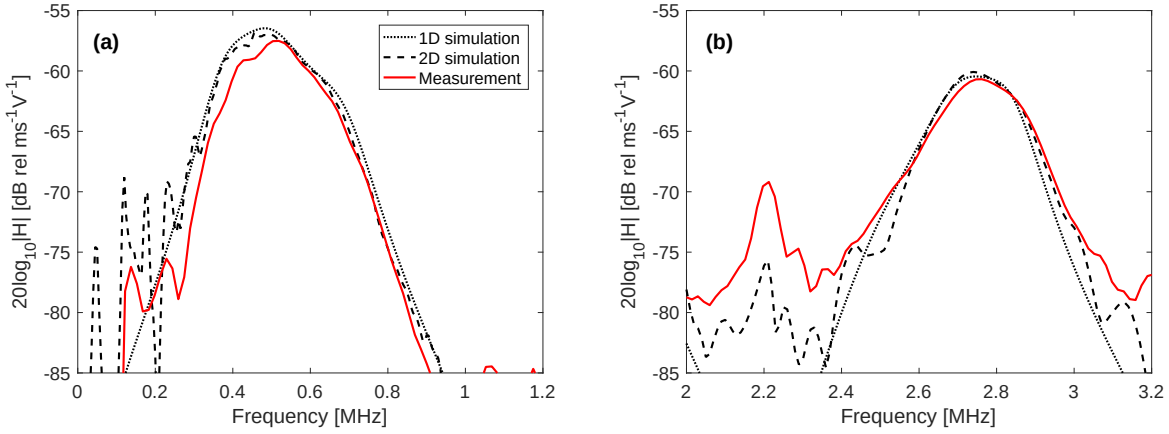

Fig. 4. Measurements (solid red) of $|H|$ compared to 1D simulations (black dotted) and 2D Comsol simulations (black dashed) for the (a) 1st and (b) 5th harmonic passbands.

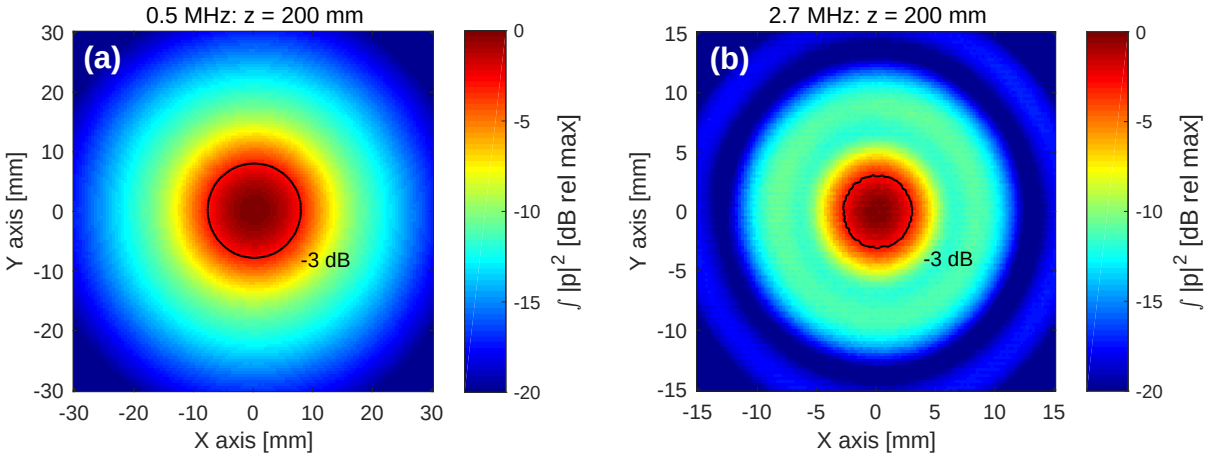

Fig. 5. Measurements of the acoustic beam pattern at 200 mm for the (a) LF and (b) HF excitation. The measurements are shown as the sum of the squared magnitude of the pressure, p.

V. Conclusion

A dual-frequency transducer for Acoustic Cluster Therapy (ACT) has been designed, manufactured, and tested. The transducer utilises the 1st and 5th harmonics of a single-layer piezoceramic disk for both insonication regimes: The 5th harmonic (2.7 MHz) is used for activation of the gaseous ACT bubbles, and the 1st harmonic (0.5 MHz) is used to obtain stable oscillations of the ACT bubbles, thereby inducing biomechanical effects that enhance the efficacy of co-administered drugs. Sonometry measurements demonstrate that the transducer is suited for activation of the ACT bubbles, and the transducer is currently in use for pre-clinical in vivo testing of ACT on murine tumours.

Acknowledgment

This work was supported by the Research Council of Norway (grant number 237887).

References

[1] P. Sontum, S. Kvåle, A. J. Healey, R. Skurtveit, R. Watanabe, M. Matsumura, and J. Østensen, "Acoustic Cluster Therapy (ACT) – A novel concept for ultrasound mediated, targeted drug delivery," *International Journal of Pharmaceutics*, vol. 495, no. 2, pp. 1019–1027, Nov. 2015.

[2] A. J. Healey, P. C. Sontum, S. Kvåle, M. Eriksen, R. Bendiksen, A. Tornes, and J. Østensen, "Acoustic Cluster Therapy: In vitro and ex vivo measurement of activated bubble size distribution and temporal dynamics," *Ultrasound in Medicine & Biology*, vol. 42, no. 5, pp. 1145–1166, May 2016.

[3] K. K. Andersen, M. Frijlink, and L. Hoff, "Numerical optimization of ultrasound transducers by the linearity of the phase spectrum," in *2017 IEEE International Ultrasonics Symposium (IUS)*, 2017, pp. 1–4.

[4] C. S. Desilets, J. D. Fraser, and G. S. Kino, "The design of efficient broad-band piezoelectric transducers," *IEEE Transactions on Sonics and Ultrasonics*, 1978.

[5] W. P. Mason, *Electromechanical transducers and wave filters*. Princeton, NJ, Van Nostrand, 1948.

[6] A. Goldstein, D. R. Gandhi, and W. D. O'Brien, "Diffraction effects in hydrophone measurements," *IEEE Transactions on Ultrasonics, Ferroelectrics, and Frequency Control*, vol. 45, no. 4, pp. 972–979, July 1998.

D. Paper D

A Dual-frequency Coupled Resonator Transducer

Kenneth K. Andersen[a], Martijn E. Frijlink [a], Tonni F. Johansen, [b,c], and Lars Hoff [a].

[a] Department of Microsystems, University of South-Eastern Norway, Horten, Norway.

[b] Department of Circulation and Medical imaging, Norwegian university of science and technology, Trondheim, Norway.

[c] SINTEF Digital, Acoustics, Trondheim, Norway.

Submitted for publication to *IEEE Transactions on Ultrasonics, Ferroelectrics, and Frequency Control*, October 2019.

A Dual-frequency Coupled Resonator Transducer

Kenneth K. Andersen, *Student Member, IEEE,* Martijn E. Frijlink, *Member, IEEE,*
Tonni F. Johansen, *Member, IEEE,* and Lars Hoff, *Member, IEEE*

***Abstract*—New ultrasound mediated drug delivery systems, such as Acoustic Cluster Therapy, or combined imaging and therapy systems, require transducers that can operate beyond the bandwidth limitation ($\sim$100 %) of conventional piezoceramic transducers. In the current paper, a dual-frequency coupled resonator transducer (CRT) comprised of a polymeric coupling layer with a low acoustic impedance (2-5 MRayl) sandwiched between two piezoceramic layers is investigated. Depending on the electrical configuration, the CRT exhibits two usable frequency bands. The resonance frequency of the high-frequency (HF) band can be tailored to be $\sim$3-5 times higher than the resonance frequency of the low-frequency (LF) band by means of the stiffness in the coupling layer. The CRT's LF band was analysed analytically and we obtained closed-form expressions for the LF resonance frequency. A dual-frequency CRT was designed, manufactured, and characterized acoustically and comparisons with theory showed good agreement. The HF band exhibited a centre frequency of 2.5 MHz with a -3 dB bandwidth of 70 %, and is suited to manipulate microbubbles, or for diagnostic imaging applications. The LF band exhibited a centre frequency of 0.5 MHz with a -3 dB bandwidth of 13 %, and is suited to induce biological effects in tissue, therein manipulation of microbubbles.**

***Index Terms*—Dual-frequency transducer design, coupled resonators, therapeutic transducers, combined imaging and therapy systems, drug delivery, Acoustic Cluster Therapy.**

I. Introduction

ACOUSTIC CLUSTER THERAPY (ACT) is a new ultrasound mediated drug delivery system currently under development for cancer treatment [1], [2]. The ACT product is a two-component microparticle formulation consisting of Sonazoid (GE Healthcare, Oslo, Norway) microbubble/oil microdroplet clusters held together by electrostatic attraction. A therapeutic treatment with ACT requires the administration of the microbubble/microdroplet clusters together with a drug and two ultrasound exposure regimes. When the clusters reach a tumour, a high-frequency (HF) sonication regime with a centre frequency above 2 MHz is used to evaporate the oil component, thereby forming gaseous bubbles ($\sim$22 µm) that lodge on the microvascular level. A second low-frequency (LF) sonication regime with a centre frequency of 0.5 MHz, closer to the resonance frequency of the gaseous bubbles, is used to enhances the uptake of the co-administered drug to the tumour.

In the current paper, our focus is on transducer designs suited for treatment of liver metastasis with ACT. The propagation path from the skin to the liver is relatively long and the HF centre frequency should therefore be $\sim$2-3 MHz. The corresponding HF-to-LF ratio is in the range 4:1 to 6:1. A transducer with a bandwidth of at least 125-150% is therefore required; however, conventional piezoceramic transducers have a bandwidth limitation of $\sim$100%. The bandwidth limitation is also a challenge for diagnostic imaging using the third, and higher, harmonics [3]; when designing combined imaging and therapy systems [4]; and for new applications such as SURF [5].

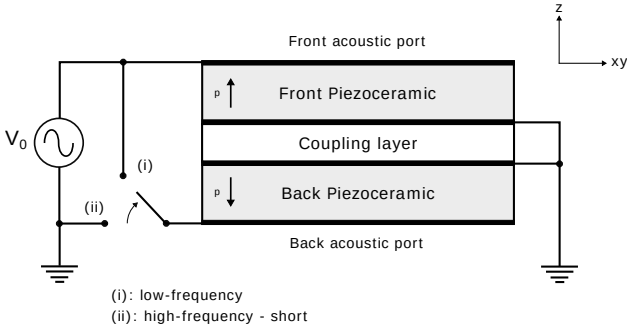

Fig. 1. A cross-sectional view of a dual-frequency coupled resonator transducer (CRT). The low-frequency (LF) and high-frequency (HF) electrical configurations are indicated using a switch, and the piezoelectric polarization directions are indicated with arrows.

To overcome the challenges presented by the bandwidth limitation, several *dual-frequency* transducer designs have been proposed in the literature. One approach is to interleave the LF and HF array elements perpendicular to the propagation direction. Using this approach, Bouakaz et al. [3] realised a transducer where the centre frequency of the HF band was 3.1 times higher than the centre frequency of the LF band. The drawbacks of this approach include grating lobes, an increase in the azimuth aperture size, and production challenges. Another approach is to stack similar active piezoceramic layers (or array elements) on top of each other in the propagation direction [6], [7]; however, this leads to a HF-to-LF ratio of $\sim$2:1. Alternatively, the LF array elements can be significantly thicker than the HF array elements with a soft polymeric layer sandwiched in between the LF and HF array elements. Using this approach, Azuma et al. [8] realised a transducer with a $\lambda/10$ polymeric layer (λ is wavelength; calculated at HF) where the centre frequency of the HF band was 4 times higher than the centre frequency of the LF band. Later, Myhre et al. [5] proposed to have alternating soft-hard-soft $\lambda/4$ layers in between the LF and HF array elements; moreover, they showed that the LF could be viewed as a spring-mass system if the HF-to-LF ratio was $>$7:1.

The current authors have previously designed a dual-frequency transducer for pre-clinical testing of ACT on tu-

This work was supported by the Research Council of Norway (grant number 237887).

K. K. Andersen, M. E. Frijlink and L. Hoff are with the Department of Microsystems, University of South-Eastern Norway, Horten, Norway. T. F. Johansen is with the Dep. Circulation and Medical imaging, Norwegian university of science and technology, Trondheim, Norway and SINTEF Digital, Acoustics, Trondheim, Norway. (e-mail: kan@usn.no).

mours in mice [9]. A HF-to-LF ratio of 5.4:1 was realised by taking advantage of the inherent harmonics in the piezoceramic [9]. A drawback of this approach was a narrow HF band, not suitable for imaging. For ACT, it would be beneficial if the HF band could be used for both imaging and to evaporate the oil component.

In the current paper, we investigate a dual-frequency coupled resonator transducer (CRT) with the potential for being used for pre-clinical and clinical testing of ACT. Compared to our previous approach [9], the CRT's HF band can be designed to exhibit similar characteristics as a conventional imaging transducer. Compared to the existing dual-frequency transducers [3], [5], [8], the CRT's LF band can be realised without the use of the relatively thick piezoceramic layer. Although the CRT has not received significant attention in the literature, some publications do exists. Paco et al. [10] developed a lumped element model of a coupled resonator filter. Powell et al. [11] developed a 1D modelling approach for multi-layered piezoceramic transducer structures, therein investigating a CRT. Wang et al. [12] designed a bifrequency array using two piezoceramic layers with a passive polymeric layer sandwiched in between the active layers; however, the polymeric layer was significantly thinner compared to $\lambda/4$, which resulted in a HF-to-LF ratio of $\sim$2.5 (comparable to [6], [7]).

In Fig. 1, a schematic of the CRT is shown. The CRT is comprised of two piezoceramic layers stacked on top of each other with a soft (2-5 MRayl) polymeric *coupling* layer sandwiched in between the active layers. The polarisation direction of the two active layers (which can be a solid piezoceramic, a piezo-polymer composite, or elements in an array transducer) are reversed. Two electrical configurations are indicated using a switch, which allows for separate HF and LF bands. If the LF electrical configuration is used, then both piezoceramics are excited electrically in parallel and mechanically in series. If the HF electrical configurations is used, the electrodes on the back piezoceramic are grounded and the front piezoceramic resonates as a half-wave resonator.

The coupling layer serves two main purposes:

1) In the LF configuration, the piezoceramics are coupled through the coupling layer which modifies the LF resonance frequency depending on the material properties of the coupling layer (thickness, stiffness) relative to the piezoceramics. If the coupling layer thickness tends to zero, the HF-to-LF ratio tends to 2:1 [6], [7].
2) In the HF configuration, a good choice for the coupling layer thickness is $\lambda/4$ [5]. The $\lambda/4$ layer acts as an impedance transformer and the mechanical impedance presented to the front piezoceramic at the boundary towards the coupling will be lower than the coupling layer impedance itself; hence, most of the acoustic energy reflects of this boundary. However, close to the centre frequency, where the back piezoceramic is $\lambda/2$, the mechanical impedance presented to the front piezoceramic at the boundary towards the coupling will be higher than the coupling layer impedance itself. Because of this, in a narrow frequency range ($\sim$5%) around the centre frequency, the acoustical energy propagates into the coupling layer and the back piezoceramic.

TABLE I
TRANSMISSION LINE PARAMETERS FOR THE PIEZOCERAMICS AND COUPLING LAYER.

Piezoceramic	
$C_0 = \epsilon_{33}^S A/l$	Clamped capacitance
$N = h_{33} C_0$	Electro-mechanical turns ratio
$Z_0 = \rho c A$	Mechanical impedance
$Z_a = iZ_0 \tan(kl/2)$	Distributed mechanical impedance
$Z_b = -iZ_0/\sin(kl)$	Distributed mechanical impedance
$Z_A = Z_a/N^2$	Distributed equivalent electrical impedance
$Z_B = Z_b/N^2$	Distributed electrical impedance
Coupling layer	
$Z_{0c} = \rho_c c_c A$	Mechanical impedance
$Z_{ac} = iZ_{0c} \tan(k_c l_c/2)$	Distributed mechanical impedance
$Z_{bc} = -iZ_{0c}/\sin(k_c l_c)$	Distributed mechanical impedance
$Z_{Ac} = Z_{ac}/N^2$	Distributed electrical impedance
$Z_{Bc} = Z_{bc}/N^2$	Distributed electrical impedance

ϵ_{33}^S, h_{33}, ρ, c are defined in Table V. A is area; l is thickness; $i = \sqrt{-1}$; $k = \omega/c$ is wave number; $\omega = 2\pi f$ is angular frequency; f is frequency

The main objective of the current paper is to obtain physical understanding of the coupling layer's effect on the LF resonance frequency. To achieve this, we first rearrange a distributed 1D equivalent circuit model [13] of the CRT's LF band to a more comprehensive circuit. A lumped equivalent model and a mechanical spring-mass analogy is developed which yields identical closed-form expressions for the LF resonance frequency A prototype dual-frequency CRT was designed, manufactured and tested acoustically. The prototype was realised as a single-element transducer to best demonstrated the dual-frequency performance of the CRT and establish the CRT as a choice for future studies of ACT.

II. THEORY

A. Distributed equivalent circuit model of the CRT's LF band

In Figure 2 (a), the distributed equivalent circuit model [13] representing the CRT's LF band is shown. The model is for a transducer in air, hence, the front and back acoustic ports are modelled as vacuum, and the front and back acoustic ports are therefore effectively short-circuited. The transmission line parameters modelling the piezoceramics and coupling layer are defined in Table I and V. A subscript $_c$ distinguishes the coupling layer parameters from the piezoceramic parameters. In Fig. 2 (b), the acoustic branches are transformed to the electrical side, and all the variables are represented as electrical analogies. The moving branch exhibits symmetry about Z_{Bc}, which we have represented as a parallel branch with doubled impedance. Utilising the symmetry, we can further rearrange the circuit to that of Fig. 2 (c), where the division by two stems from the parallel connection of the front and back moving branches. From the circuit in Fig. 2 (c), we find the electrical input admittance of the CRT's LF band:

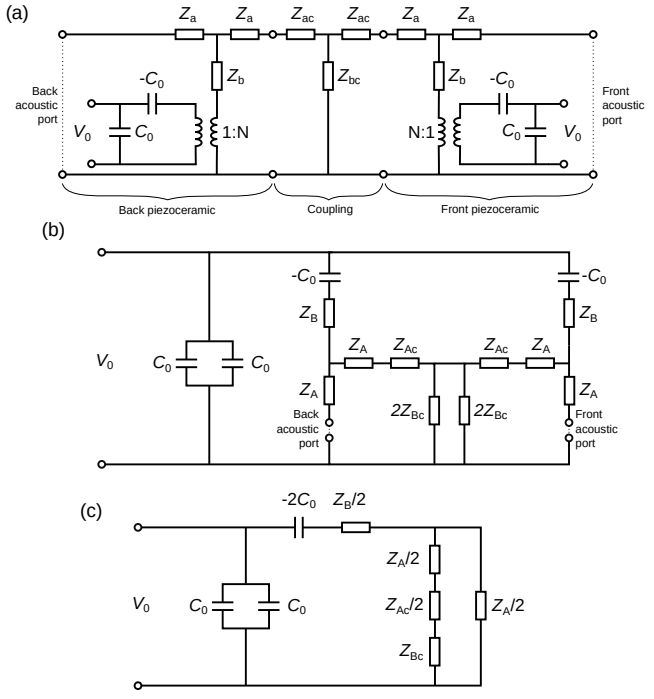

Fig. 2. Distributed equivalent circuit models of the CRT's LF band. (a) Electrical and mechanical variables. (b) All variables are referred to the electrical side, and the transmission line parameter Z_{Bc} is represented as a parallel branch, revealing the symmetry in the circuit. (c) Rearrangement of the circuit in (b).

$$Y = 2\left[i\omega C_0 + \frac{1}{i/\omega C_0 + Z_B + \frac{Z_A(Z_A+Z_{Ac}+2Z_{Bc})}{2Z_A+Z_{Ac}+2Z_{Bc}}}\right]. \quad (1)$$

B. Lumped equivalent circuit model of the CRT's LF band

Transforming the distributed circuit model to a lumped equivalent circuit model allows physical interpretation of the transmission line parameters by representing these as inductors (masses) and capacitors (inverse of stiffnesses). Because the CRT's LF resonance frequency is ∼3-5 times lower than the half-wave resonance of the piezoceramics (cf. Sec. IV-A2), a 1st order Taylor series can be used to estimate the lumped circuit components, shown in Table II. Note that the coupling layer's inductance is small compared to the piezoceramic's inductance, and can safely be neglected. The lumped equivalent circuit model of the CRT's LF band is shown in Fig. 3, where $C_{0B} = C_0C_B/(C_0 - C_B)$ is the parallel equivalent of the piezoelectric stiffening $-1/C_0$ in series with the piezoceramic mechanical stiffness $1/C_B$. From Fig. 3, the input admittance can be approximated as

$$Y \approx 2\left[i\omega C_0 + \frac{1}{1/i\omega C_{0B} + \frac{i\omega L_A(i\omega L_A+2/i\omega C_{Bc})}{2i\omega L_A+2/i\omega C_{Bc}}}\right], \quad (2)$$

and we find a closed form expression for the LF resonance frequency, ω_r, by letting $Y \to \infty$:

$$\omega_r^2 = \frac{1}{L_AC_{0B}C_{Bc}}\left[C_{0B} + C_{Bc} - \sqrt{C_{0B}^2 + C_{Bc}^2}\,\right], \quad (3)$$

TABLE II
LOW-FREQUENCY CIRCUIT COMPONENTS.

Quantity		1st order Taylor approx.	Description
Z_A	$\to$	$L_A = \rho l A/2N^2$	Motional inductance (piezoceramic)
Z_B	$\to$	$C_B = lN^2/\rho c^2 A$	Motional capacitance (piezoceramic)
Z_{Bc}	$\to$	$C_{Bc} = l_cN^2/\rho_c c_c^2 A$	Motional capacitance (coupling)

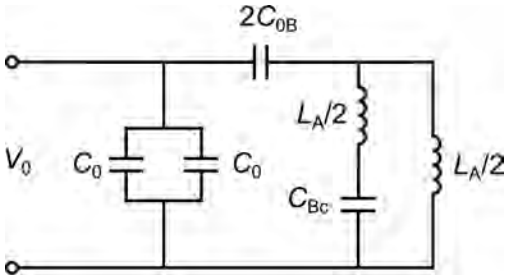

Fig. 3. Lumped circuit model of the CRT's LF band.

which shows the relationship between the different circuit components and the resonance frequency. As expected, the input capacitance, C_0, does not affect the resonance frequency; however, the resonance frequency increases with increasing coupling layer stiffness and, conversely, decreases with decreasing coupling layer stiffness.

C. Spring-mass representation of the CRT's LF resonance frequency

In the current section, a spring-mass analogy of the CRT's LF resonance frequency will be developed. The spring-mass analogy is an alternative to the electrical circuit diagrams, and is useful when interpreting the motion of the masses. In Fig. 4 (a), the mechanical spring-mass representation of the CRT's LF is shown. In Table III, the correspondence between the mechanical and electrical variables are shown. Both piezoceramics are modelled as two half-masses connected with a spring of constant K_{0B} acted on by forces indicate with F. The piezoceramics are connected with a spring, K_{Bc}, which models the stiffness of the coupling layer. As in Sec. II-B, the mass of the coupling layer is left out.

In Fig. 4 (b), the electrical analogy of the mechanical system in (a) is shown. The circuit exhibits symmetry about C_{Bc} which can be taken advantage of by representing it as a parallel branch with half the value (similar to Fig. 2 (b)). In Fig. 4 (c), the mechanical spring-mass system utilizing the symmetry is shown with the coupling layer stiffness $2K_{Bc}$. From (c), the resonance frequency is found by a balance of forces:

$$\omega_r^2 = \frac{1}{m/2}\left[K_{0B} + K_{Bc} - \sqrt{K_{0B}^2 + K_{Bc}^2}\,\right], \quad (4)$$

which, using the analogies in Table III, is identical to Eq.(3) and the considerations made in Sec. II-B applies also here. The arrows in Fig. 4 (c) illustrates vector quantities of the displacement of the masses, discussed further in Sec. V-A.

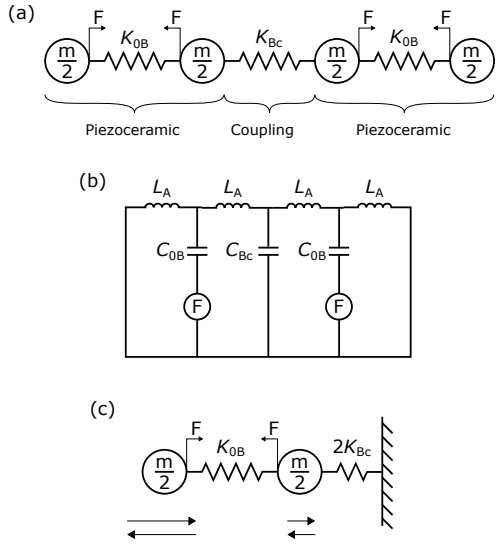

Fig. 4. Spring-mass analogy of the CRT's LF band. (a) The piezoceramics are represented as two half-masses connected with a spring of constant K_{0B}. The coupling layer connects the piezoceramics with a spring of constant K_{Bc}. (b) Electrical analogy of (a). (c) Utilising symmetry, the coupling layer stiffness is $2K_{Bc}$.

TABLE III
MECHANICAL AND ELECTRICAL ANALOGIES.

Mechanical		Electrical
$m/2$	$\leftrightarrow$	L_A
K_{0B}	$\leftrightarrow$	$1/C_{0B}$
K_{Bc}	$\leftrightarrow$	$1/C_{Bc}$

III. METHODS

The current section describes the design, manufacturing, and measurement methods of the prototype dual-frequency CRT. The material properties are given in Table V.

A. Design considerations

To best demonstrate the fundamental dual-frequency properties of the CRT, a single-element transducer with a square aperture of 17x17 mm radiating in water was chosen. For the current study, the ideal HF-to-LF ratio is 4:1 to 6:1, and the LF centre frequency should be $\sim 0.5\,\mathrm{MHz}$.

The active piezoceramics were chosen as 65% PZT Navy Type II 1-3 piezo-polymer random fibre composites (Smart Material GmbH, Dresden, Germany) to enhance the HF bandwidth, suppress lateral modes, and increase the CRT's LF band effective coupling coefficient and mechanical quality factor (cf. Sec. V-B). Although alignment of the ceramic posts is a known challenge in stacked composite arrays [14], 2D FEM simulations (Comsol AB, Stockholm, Sweden) indicate that the CRT's LF does not suffer from post alignment challenges. The remaining structural and material parameters (composite thickness, speed of sound and density in the coupling layer) were obtained using Eq.(3), and EPO-TEK 301-2, a commercially available epoxy glue, was chosen as a suitable material for the $\lambda/4$ coupling layer.

To obtain a broadband HF spectrum suitable for imaging, the CRT's HF band was matched to the water medium with two $\lambda/4$ matching layers. With this choice, the matching layers are much thinner than $\lambda/4$ at the LF, resulting in a narrow LF bandwidth; however, for ACT, this is acceptable since the LF can be used with several pulse cycles. The ideal matching layer impedance values were obtained following DeSilets' guidelines [15] and materials with similar properties were chosen. To maintain the transmit sensitivity of the LF, the backing material was chosen to be air.

As discussed in Sec.V-D, although much thinner than $\lambda/4$, the matching layers presents a mass load to the CRT's LF band. Because of this, Eq.(3) predicts a $5\,\%$ to $10\,\%$ higher resonance frequency compared to a transducer with matching layers. With the material choices made and reducing the LF resonance frequency with 10%, the LF and HF resonance frequencies were expected to be around $0.55\,\mathrm{MHz}$ and $2.5\,\mathrm{MHz}$, respectively.

B. Manufacturing

A wrap-around electrode was applied to both composites using physical vapour deposition (AJA International, Inc, MA, USA). The coupling layer and matching layers were ground down to their respective $\lambda/4$ thicknesses and subsequent layers were glued together with an epoxy adhesive, DP460 (3M, Minnesota, USA). During curing for three hours at $60\,^{\circ}\mathrm{C}$, the layers were pressed together using a bonding jig with an adjustable force. Upon completion, lead wires were soldered to the electrodes and the transducer was housed in a 3D printed plastic house with two BNC connectors for the external electrical connections.

C. Acoustical measurements

The acoustical measurements were performed in an AIMS III measurement system (Onda Corporation, CA, USA) consisting of a water tank with a three-axis stage controlling the position of a calibrated Onda HGL0200 *Golden Lipstick* hydrophone connected to an AG-2010 pre-amplifier. The on-axis spectral pressure value at the face of the hydrophone, $P(f, z)$, was obtained by deconvolving the spectrum of the recorded voltage traces with the hydrophone and preamplifier calibration data. Note that the hydrophone was only calibrated in the range $1\,\mathrm{MHz}$ to $20\,\mathrm{MHz}$, which causes uncertainty in the measured pressure values below $1\,\mathrm{MHz}$.

To quantify the performance of the dual-frequency CRT, we used the electro-mechanical transfer function $H = U/V$, where U is the particle velocity at the face of the transducer, and V is the input voltage at the terminals of the transducer. An estimate of the magnitude of the electro-mechanical transfer function H was obtained by

$$|H(f)| = \Big| \frac{P(f, z)}{V(f) D(f, z) Z_L} \Big|, \tag{5}$$

where $V(f)$ is the spectrum of the measured voltage at the transducer terminals, $D(f, z)$ is diffraction correction obtained by numerical integration of the Rayleigh integral for a square plane piston mounted in an infinite and rigid baffle, and Z_L is the characteristic impedance of water.

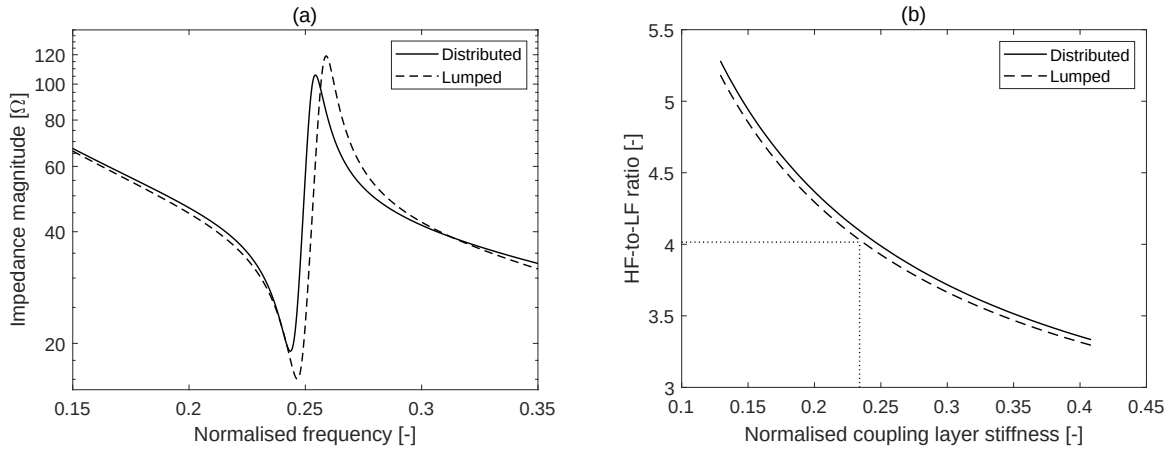

Fig. 5. (a) Electrical impedance $(1/Y)$ of the composite CRT's LF band obtained with Eg.(1) (distributed) and Eg.(2) (lumped). The frequency is normalised to the HF resonance frequency (2.5 MHz). (b) Effect of varying the coupling layer stiffness on the CRT's HF-to-LF ratio. The coupling layer stiffness is normalised to the stiffness in the composites.

IV. Results

In both the results and discussion sections, unless otherwise stated, the dual-frequency CRT will be comprised of two 65% piezo-polymer composite plates with a $\lambda/4$ coupling layer of EPO-TEK 301-2, referred to as a composite CRT. 1D simulations based on the model proposed by Mason [13], further described in [16], and FEM simulations (Comsol AB, Stockholm, Sweden) will be used throughout to evaluate the performance of the CRT. In Figure 6, pictures of the prototype dual-frequency CRT are shown.

Fig. 6. Two pictures of the prototype dual-frequency CRT.

A. Distributed vs. lumped model

1) Electrical impedance: In Figure 5 (a), we compare the composite CRT's LF electrical impedance $(1/Y)$ obtained with Eq.(1) (distributed) and Eq.(2) (lumped). The electrical impedances are therefore of a transducer radiating in vacuum. The frequency is normalised to the HF resonance frequency at 2.5 MHz. Compared to the distributed model, the lumped model exhibits a 1.7% increase in the resonance frequency and some deviations in the magnitude values around the resonance and anti-resonance frequencies; a consequence of neglecting the mass of the coupling layer. For the given material choices, the HF-to-LF ratio is ∼4:1.

2) Coupling layer stiffness: In Figure 5 (b), we show the HF-to-LF ratio as a function of varying the coupling layer stiffness relative to the stiffness in the 65% piezo-polymer composites. The coupling layer stiffness corresponds to a specific acoustic impedance of 1.6 MRayl to 5.1 MRayl. Throughout, the coupling layer thickness is held constant at $\lambda/4$ (calculated at HF). The results are shown for both Eq.(1) (distributed) using the maximum of the admittance, and Eq.(4) (lumped). Notably, by varying the coupling layer stiffness in the specified range, the HF resonance frequency can be tailored to be 3.3-5.2 times higher than the LF resonance frequency. Compared to the distributed model, the lumped model predicts a 2 % to 1.2 % higher resonance frequency. The dotted line indicates that the coupling layer stiffness is identical to EPOTEK 301-2; a HF-to-LF ratio of ∼4:1 is observed, comparable to the results shown in Fig. 5 (a).

B. Experimental results

1) Electro-mechanical transfer function: In Figure 7, the measurements of $|H|$ is compared to 1D simulations for (a) the CRT's LF band and (b) the CRT's HF band. For both measurements, a Panametrics 5800 (Olympus Inc., Waltham, MA) pulser was used to excite the transducer.

The measured and simulated LF magnitude spectra compare well; however, the measured peak magnitude is −50 dB at 0.52 MHz, 1.3 dB lower compared to the simulation which peaks at 0.55 MHz. The measured one-way −3 dB bandwidth is 13%. The measured and simulated HF magnitude spectra compare well throughout the frequency range. The measured one-way −3 dB bandwidth is 70%. At 2.5 MHz, a notch in the magnitude spectra is observed. The notch corresponds to an increase in the coupling layer impedance, hence, the acoustic energy will also propagate backwards and into the coupling layer (cf. Sec. I). If an absorbing backing is used, the notch can be reduced without reducing the overall HF magnitude; however, the overall LF magnitude will be reduced.

Around 0.5 MHz, the LF resonance caused by the front composite alone is observed. Compared to Fig. 7 (a), the LF

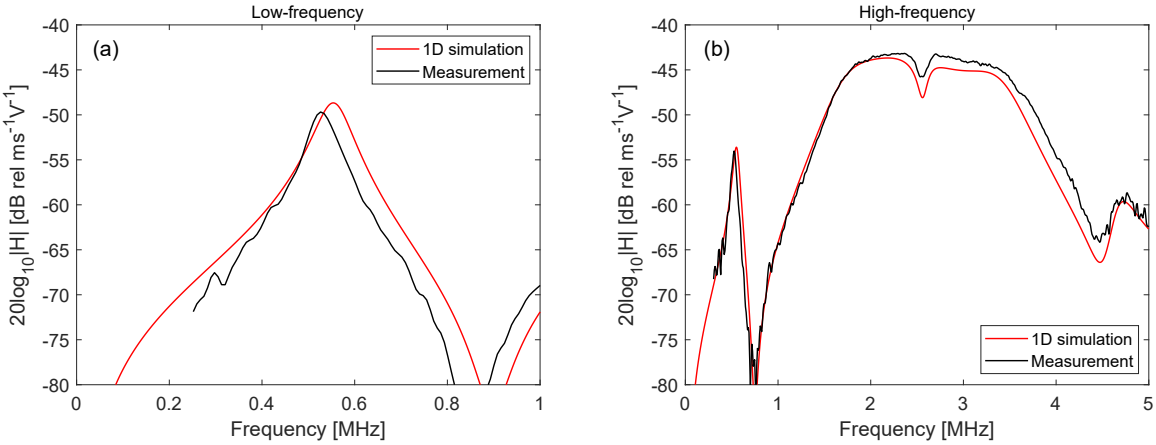

Fig. 7. Measurements and 1D simulations of the magnitude of the electro-mechanical transfer function $|H|$ for the CRT's LF band (a) and HF band (b).

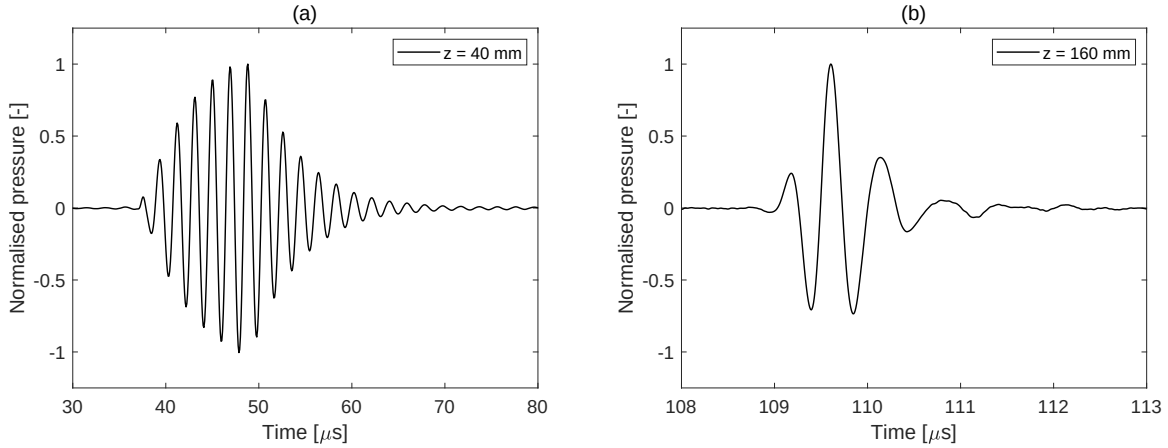

Fig. 8. Measured pressure pulses for (a) the CRT's LF band using a 6 period sine excitation with a centre frequency of 0.5 MHz, and (b) the CRT's HF band using a one period sine excitation with a centre frequency of 2 MHz. For both pulses, the pressure values are normalised to their respective pressure maxima.

resonance in Fig. 7 (b) is 4 dB lower and the -3 dB bandwidth is 8%. A possible application of this resonance is discussed in Sec. V-E. Lastly, we note that if the full HF bandwidth is utilised, the HF is 3.5-7 times higher then the LF.

2) Pressure pulses: In Figure 8 (a), the measured pressure pulse for the CRT's LF band is shown for a 6 period 0.5 MHz sinusoid excitation. The LF pulse uses ∼6 pulse cycles to reach steady-state conditions; a consequence of the narrow bandwidth. However, the LF pulse is designed to induce biological effects in tissue or to manipulate bubbles, which typically require several pulse cycles. In Figure 8 (b), the measured pressure pulse for the CRT's HF band is shown for a one period 2.0 MHz sinusoid excitation. The HF pulse is a typical wideband imaging pulse with some ringing in the tail; however, the ringing is below -20 dB one-way of the maximum, which renders it suited for imaging applications or manipulation of bubbles.

The LF and HF centre frequencies were chosen to yield a HF-to-LF ratio of 4:1, and the measurements were conducted 40 mm and 160 mm from the transducer, respectively; past the last axial pressure maxima.

V. Discussion

A. Particle displacement

In Figure 9, a 1D FEM simulation of the particle displacement in the composite CRT's LF band is shown. The vertical dashed lines indicate the interfaces between the coupling layer (centred) and the composites. The particle displacement is shown for the LF resonance frequency, and both the displacement and position through the CRT are normalised to their respective maxima. Displacement maxima are observed at the back and front of the CRT, and a displacement node is observed in the centre of the coupling layer. Relative to the composites, more than 50% of the displacement occurs in the coupling layer; an expected result considering that the stiffness in the coupling layer is 4.3 times lower compared to the composites.

B. Composite CRT

The prototype dual-frequency CRT was manufactured using 1-3 piezo-polymer composites. The benefits (e.g., increased coupling coefficient and bandwidth, and reduced characteristic impedance) of composites for conventional transducers are

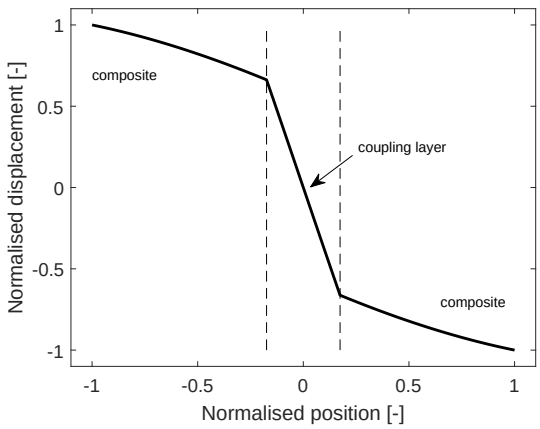

Fig. 9. 1D FEM simulation of the particle displacement through the composite CRT at the LF resonance frequency.

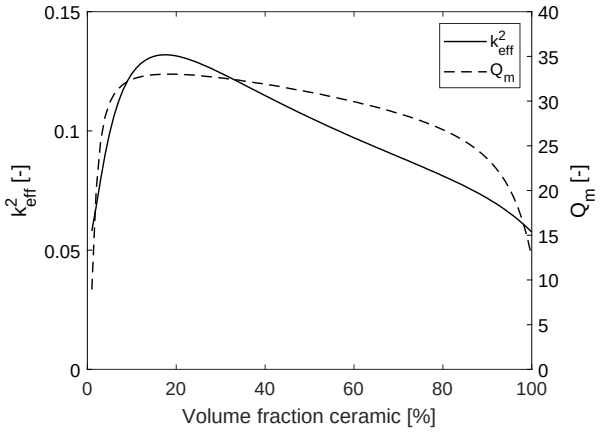

Fig. 10. Effective coupling coefficient, k^2_{eff}, and mechanical quality factor, Q_m, as functions of volume fraction of ceramic for the composite CRT's LF band.

well known and understood [17]; however, the effect of using composites on the CRT's LF band is not previously discussed.

To evaluate the effects of using composites on the CRT's LF band, we will use the effective coupling coefficient

$$k^2_{\text{eff}} = 1 - \left(\frac{f_r}{f_a}\right)^2, \tag{6}$$

and the mechanical quality factor

$$Q_m = \frac{f_r}{f_2 - f_1}, \tag{7}$$

where f_r and f_a are the resonance and anti-resonance frequencies, respectively, and f_1 and f_2 are the $-3\,\text{dB}$ frequency points from the maximum of the admittance power spectrum obtained with Eq.(1) [18, ch.12]. The composites were comprised of a Pz27 piezoceramic with EPO-TEK 301-2 as the kerf filler and $\lambda/4$ coupling layer material. The effective material parameters for the composites were calculated using the model by Smith and Auld [17]. To account for material losses, the variables in the thickness direction were complex [19] and the accuracy of the effective material parameters were verified by comparisons to 3D FEM simulations.

In Figure 10, k^2_{eff} and Q_m are shown as functions of volume fraction of ceramic for the composite CRT's LF band. In Table IV, we compare k^2_{eff} and Q_m for the composite CRT with a conventional composite for 65% and 100% volume fraction of ceramic (100% volume fraction ceramic is, off course, identical to a solid piezoceramic).

For the composite CRT's LF band, using 65% compared to 100% volume fraction increases k^2_{eff} with 50%. Comparing the composite CRT's LF band with the conventional composite, k^2_{eff} is $\sim$70% lower for both volume fractions. A reduction in k^2_{eff} is, off course, unfavourable; however, in Sec. V-C, we show that the electro-acoustical efficiency of the CRT's LF band is comparable to the conventional composite at the resonance frequency, indicating that k^2_{eff} may not be the right figure of merit for the CRT's LF band.

With respect to Q_m, an interesting thing occurs. For the conventional composite, an expected decrease in Q_m is observed for a decrease in the volume fraction of ceramic [20]. However, for the composite CRT's LF band, Q_m increases with a decrease in the volume fraction. The reason for the latter is related to the reduced mechanical impedance as the volume fraction reduces, which results in a higher transmission coefficient at the interfaces between the composites and coupling layer. More mechanical energy is, therefore, transmitted through the coupling layer, enhancing the coupling between the resonators. Lastly we note that doubling the losses in the coupling layer reduces Q_m with 60%, and materials with a low loss are therefore generally preferred.

TABLE IV
EFFECTIVE COUPLING COEFFICIENT AND MECHANICAL QUALITY FACTOR FOR THE COMPOSITE CRT'S LF BAND COMPARED TO A CONVENTIONAL COMPOSITE.

	Composite LF CRT		Conventional Composite	
Volume fraction	65%	100%	65%	100%
k^2_{eff}	0.09	0.06	0.35	0.2
Q_m	30	13	41	68

C. Efficiency of the CRT's LF band

In Section V-B, a significant reduction in k_{eff} for the CRT's LF band compared to a conventional composite was shown. Because of this, it is fair to question the effectiveness of the CRT's LF band to convert electrical energy to mechanical energy. To quantify this, we will use 1D simulations [16] of the electro-acoustical efficiency calculated as the ratio of the output acoustic power to the input electrical power [18, ch.2]. The composite CRT's LF band will be compared to a conventional composite. The conventional composite's thickness was scaled to yield identical resonance frequency as the CRT's LF and was 4.2 times thicker than the CRT's composites. Identical material parameters were used for both the composite CRT and the conventional composite and both transducers radiated in water. Although unmatched transducer are inefficient, the relative comparison is informative.

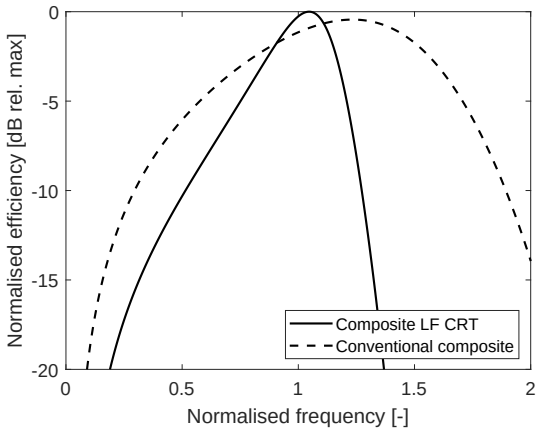

Fig. 11. 1D simulations of the electroacoustic efficiency for the composite CRT's LF band compared to a conventional composite. The efficiencies are normalised to the maximum corresponding to the CRT's LF band.

In Fig. 11, the simulated efficiencies are shown. The frequency is normalised to the respective resonance frequencies and the magnitude is normalised to the maximum of the CRT's LF band. Clearly, the CRT's LF band is more narrow compared to the conventional composite; however, at resonance, the CRT's efficiency is $1\,\mathrm{dB}$ higher compared to the conventional composite. For all practical applications, at resonance, the CRT's LF performs comparable to the conventional composite, and the CRT is therefore suited for applications requiring pulses with a high amplitude and several pulse cycles.

D. Effect of mass loading on the CRT's LF band

In deriving Eqs.(1-4) the matching and backing layers, as well as the radiation medium, were neglected. The prototype dual-frequency CRT was, however, matched to water using two $\lambda/4$ matching layers (calculated at HF). Although the layers were much thinner than a $\lambda/4$ at the LF, they present a mass load to the CRT's LF band. We investigated the mass loading effect on the CRT's LF band using 1D simulations, and the results showed that Eqs.(1-4) predict a 5-10% higher resonance frequency compared to a CRT's LF band where matching and backing layers, as well as radiation medium, were included.

E. An alternative dual-frequency transducer

In Figure 7 (b), in addition to the main resonance centred at $2.5\,\mathrm{MHz}$, we saw that $|H|$ exhibited a resonance at $\sim 0.5\,\mathrm{MHz}$. At the expense of a $4\,\mathrm{dB}$ reduction in $|H|$, it is therefore possible to obtain a LF band without exciting the back composite. The back composite could also be replaced by a metallic layer (e.g., copper) while retaining similar response as observed in Fig. 7 (b) (confirmed by 1D simulations). A dual-frequency transducer, as such, will have a reduced number of electrical connections compared to a CRT with two piezoelectric layers and may therefore be beneficial for microscopic dual-frequency transducers, e.g., positioned on a needle tip, a catheter, or similar designs where restrictions on all the lateral dimensions exists.

VI. Conclusion

A dual-frequency coupled resonator transducer (CRT) comprised of a soft polymeric layer sandwiched in between two active piezoceramic layers have been investigated. Depending on the electrical configuration, the CRT allows for a high-frequency (HF) and a low-frequency (LF) band. The CRT's LF band was investigated from a theoretical perspective. Distributed, lumped, and mass-spring models describing the LF band were developed, from which analytical expressions for the LF resonance frequency were obtained. One analysis showed that the HF-to-LF ratio can be tailored to be in the range 3.3:1 to 5.2:1 by varying the stiffness of the polymeric layer.

Using the analytical expressions, a prototype dual-frequency CRT was designed, manufactured, and tested acoustically. The target application was ACT [1], [2], where a HF-to-LF ratio in the range 4:1 to 6:1 is ideal. The prototype performed comparable to theory, and the HF was 3.5-7 times higher then the LF utilising the full HF bandwidth.

VII. Appendix A

In Table V, the material properties used in the simulations and for the prototype dual-frequency CRT are given.

References

[1] P. Sontum, S. Kvåle, A. J. Healey, R. Skurtveit, R. Watanabe, M. Matsumura, and J. Østensen, "Acoustic Cluster Therapy (ACT) – A novel concept for ultrasound mediated, targeted drug delivery," *International Journal of Pharmaceutics*, vol. 495, no. 2, pp. 1019–1027, Nov. 2015.

TABLE V
Material properties.

Symbol	Unit	Ferroperm™ Pz27 [21]	Smart Materials 65% random fiber PZT Navy Type II	EPO-TEK™ 301-2	Matching layer one	Matching layer two
h_{33}	$10^9\,\mathrm{V/m}$	2.3	2.7	-	-	-
$\epsilon^S_{33}/\epsilon_0$	-	790(1-i0.006)	460(1-i0.013)	-	-	-
c	$\mathrm{m/s}$	4445(1+i0.008)	3915(1+i0.013)	2600(1+i0.015)	2245(1+i0.03)	2265(1+i0.03)
ρ	$\mathrm{kg/m^3}$	7720	5108	1143	3560	1060
$Z = c\rho$	MRayl	34.3	20	3.0	8	2.4

h_{33} is piezoelectric coefficient; ϵ^S_{33} is complex clamped dielectric constant [19]; ϵ_0 permittivity of free space; c is complex speed of sound [19]; ρ is density.

[2] A. J. Healey, P. C. Sontum, S. Kvåle, M. Eriksen, R. Bendiksen, A. Tornes, and J. Østensen, "Acoustic Cluster Therapy: In Vitro and Ex Vivo Measurement of Activated Bubble Size Distribution and Temporal Dynamics," *Ultrasound in Medicine & Biology*, vol. 42, no. 5, pp. 1145–1166, May 2016.

[3] A. Bouakaz, S. Frigstad, F. J. Ten Cate, and N. de Jong, "Super harmonic imaging: a new imaging technique for improved contrast detection," *Ultrasound in medicine & biology*, vol. 28, no. 1, pp. 59–68, 2002.

[4] H. J. Jang, J.-Y. Lee, D.-H. Lee, W.-H. Kim, and J. H. Hwang, "Current and Future Clinical Applications of High-Intensity Focused Ultrasound (HIFU) for Pancreatic Cancer," *Gut and Liver*, vol. 4, no. Suppl 1, pp. S57–S61, Sep. 2010.

[5] O. F. Myhre, T. F. Johansen, and B. A. Johan Angelsen, "Analysis of acoustic impedance matching in dual-band ultrasound transducers," *The Journal of the Acoustical Society of America*, vol. 141, no. 2, pp. 1170–1179, Feb. 2017.

[6] J. A. Hossack and B. A. Auld, "Improving the characteristics of a transducer using multiple piezoelectric layers," *IEEE Transactions on Ultrasonics, Ferroelectrics, and Frequency Control*, vol. 40, no. 2, pp. 131–139, Mar. 1993.

[7] S. Saitoh, M. Izumi, and Y. Mine, "A dual frequency ultrasonic probe for medical applications," *IEEE transactions on ultrasonics, ferroelectrics, and frequency control*, vol. 42, no. 2, pp. 294–300, 1995.

[8] T. Azuma, M. Ogihara, J. Kubota, A. Sasaki, S.-i. Umemura, and H. Furuhata, "Dual-frequency ultrasound imaging and therapeutic bilaminar array using frequency selective isolation layer," *IEEE Transactions on Ultrasonics, Ferroelectrics and Frequency Control*, vol. 57, no. 5, pp. 1211–1224, May 2010.

[9] K. K. Andersen, A. Healey, N. L. Bush, M. E. Frijlink, and L. Hoff, "A Harmonic Dual-Frequency Transducer for Acoustic Cluster Therapy," *Ultrasound in Medicine & Biology*, vol. 45, no. 9, pp. 2381–2390, Sep. 2019.

[10] P. D. Paco, O. Menéndez, and E. Corrales, "Equivalent circuit modeling of coupled resonator filters," *IEEE Transactions on Ultrasonics, Ferroelectrics, and Frequency Control*, vol. 55, no. 9, pp. 2030–2037, Sep. 2008.

[11] D. J. Powell, G. Hayward, and R. Y. Ting, "Unidimensional modeling of multi-layered piezoelectric transducer structures," *IEEE Transactions on Ultrasonics, Ferroelectrics, and Frequency Control*, vol. 45, no. 3, pp. 667–677, May 1998.

[12] Z. Wang, S. Li, T. J. Czernuszewicz, C. M. Gallippi, R. Liu, X. Geng, and X. Jiang, "Design, Fabrication, and Characterization of a Bifrequency Colinear Array," *IEEE Transactions on Ultrasonics, Ferroelectrics, and Frequency Control*, vol. 63, no. 2, pp. 266–274, Feb. 2016.

[13] W. P. Mason, *Electromechanical transducers and wave filters*. Princeton, NJ, Van Nostrand, 1948.

[14] D. M. Mills and S. W. Smith, "Multi-layered PZT/polymer composites to increase signal-to-noise ratio and resolution for medical ultrasound transducers," *IEEE Transactions on Ultrasonics, Ferroelectrics, and Frequency Control*, vol. 46, no. 4, pp. 961–971, Jul. 1999.

[15] C. S. DeSilets, J. D. Fraser, and G. S. Kino, "The design of efficient broad-band piezoelectric transducers," *IEEE Transactions on Sonics and Ultrasonics*, vol. 25, no. 3, pp. 115–125, May 1978.

[16] T. Johansen and B. Angelsen, "Versatile analysis of multilayer piezoelectric transducers using an admittance matrix approach," in *Proceedings of the 28th Scandinavian Symposium on Physical Acoustics*, Jan. 2005.

[17] W. A. Smith, A. Shaulov, and B. A. Auld, "Tailoring the Properties of Composite Piezoelectric Materials for Medical Ultrasonic Transducers," in *IEEE 1985 Ultrasonics Symposium*, Oct. 1985, pp. 642–647.

[18] C. H. Sherman and J. L. Butler, *Transducers and arrays for underwater sound*, 1st ed. Springer-Verlag New York, 2007.

[19] S. Sherrit and K. B. Mukherjee, "Characterization of Piezoelectric Materials for Transducers," 2007. [Online]. Available: arXiv:0711.2657

[20] X. Geng, "Numerical modeling and experimental study of piezocomposite transducers," Ph.D. dissertation, The Pennsylvania State University, 1997.

[21] L. Tran-Huu-Hue, F. Levassort, N. Felix, D. Damjanovic, W. Wolny, and M. Lethiecq, "Comparison of several methods to characterise the high frequency behaviour of piezoelectric ceramics for transducer applications," *Ultrasonics*, vol. 38, no. 1-8, pp. 219–223, Mar. 2000.

Doctoral dissertation no. 66
2020
—

Therapeutic dual-frequency ultrasound transducers

Dissertation for the degree of PhD

—

Kenneth Kirkeng Andersen

—

ISBN: 978-82-7860-427-4 (print)
ISBN: 978-82-7860-428-1 (online)

usn.no